Signaling Regulation of the Epithelial-Mesenchymal Transition in the Hypoxic Pancreas Cancer Microenvironment

---

A Dissertation

Presented to the Faculties of the School of Engineering and Applied Science at

University of Virginia

In partial fulfillment of the requirements for the

Degree of Doctor of Philosophy in Chemical Engineering

by

Brooke Ashley Brown

2023

Doctoral Committee:

Matthew Lazzara, Ph.D., Advisor

Roseanne Ford, Ph.D., Chair

Amy Bouton, Ph.D.

Christopher Highley, Ph.D.

Ben Stanger, M.D., Ph.D.

APPROVAL SHEET

This
Dissertation

is submitted in partial fulfillment of the requirements
for the degree of
Doctor of Philosophy

Author: Brooke Brown

This Dissertation has been read and approved by the examining committee:

Advisor: Matthew Lazzara

Advisor:

Committee Member: Roseanne Ford

Committee Member: Amy Bouton

Committee Member: Christopher Highley

Committee Member: Ben Stanger

Committee Member:

Committee Member:

Accepted for the School of Engineering and Applied Science:

Jennifer L. West, School of Engineering and Applied Science
May 2023

ACKNOWLEDGEMENTS

This thesis was supported by many incredible colleagues, friends, and family. I want to thank my advisor, Matt Lazzara, for his mentorship and scientific guidance. I have been very fortunate to collaborate with many incredible scientists that have helped to challenge my research and push me as a scientist. I am grateful to the members of the Lazzara lab for their scientific discussions and friendship to pursue this work in such a collaborative environment. Thank you to friends, both near and far, for providing joy and balance to my life, especially to Lauren, whom I am so glad I got to share this experience with. I would not be here today without the love and support of my amazing family. I especially want to thank my parents, John and Liz, for always encouraging me to believe in myself, and my siblings, Lauren and Derek, and Michael and Lauren, for always uplifting me. Lastly, I am so incredibly grateful to my amazing husband, Alex for his endless encouragement and love – his support was truly invaluable to this work.

ABSTRACT

The tumor microenvironment contributes to the progression of pancreatic ductal adenocarcinoma (PDAC), an almost uniformly lethal disease. Here, we demonstrate how tumor hypoxia resulting from characteristic PDAC hypovascularity drives epithelial-mesenchymal transition (EMT), a cellular program that occurs early in metastasis and promotes chemoresistance. The work described in this thesis establishes hypoxia as a *bona fide* driver of EMT in pancreas cancer and uncovers the molecular mechanisms through which hypoxia promotes a heterogeneous, but highly durable, EMT in transformed PDAC ductal cells. Multiple mouse models, publicly available human patient data, single-cell and bulk omics, cell-based assays, and data science models are employed to gain a comprehensive and systematic understanding of the signal transduction and epigenetic regulatory processes governing hypoxia-mediated EMT. We find that neoplastic PDAC cells preferentially undergo EMT in hypoxic tumor regions and that hypoxia drives a cell-autonomous EMT in PDAC cells that is substantially more persistent than EMT in response to growth factors. We further identify an oxygen-dependent histone methylation-MAPK signaling positive feedback process that is responsible for driving EMT in response to hypoxia. The signaling process initiated by low oxygen tension that leads to durable phenotype switching can be pharmacologically targeted to inhibit, and even reverse, hypoxia-mediated EMT. Further, through single-cell RNA-sequencing, we uncover the transcriptional basis for the heterogeneity of hypoxia- and growth factor-mediated EMT. We identify context-dependent transcripts that preferentially control EMT by actively suppressing or promoting the mesenchymal state in hypoxic culture, but not in response to growth factors. Collectively, these findings identify several potential vulnerabilities in hypoxia-mediated signaling for EMT in PDAC and nominate specific targeted inhibitors for incorporation into combination therapies designed to augment chemoresponse by antagonizing EMT.

TABLE OF CONTENTS

LIST OF TABLES

LIST OF FIGURES

CHAPTER 1: INTRODUCTION

1.1 PANCREAS CANCER SURVIVAL RATES AND SUBTYPES

Pancreatic ductal adenocarcinoma (PDAC) has one of the lowest survival rates of all cancers, with a five-year survival of only 11% (2022, American Cancer Society). This can be attributed to the fact that patients are often not diagnosed until advanced metastatic disease (1). More than 50% of PDAC patients have detectable metastasis at diagnosis, but autopsies suggest that an even larger percentage of patients have metastatic disease (2,3). Due to nonspecific symptoms, patients usually present with advanced disease, which allows less than 10% of patients to be eligible for surgical resection (4,5). Even with complete resection, relapse occurs 80% of the time, suggesting that undetectable metastases are also present at diagnosis for most surgical patients (6). The current standard of care of chemotherapies, commonly gemcitabine or FOLFIRINOX, potentially in combination with other agents, only results in a median survival of 23 months (4,7). Immunotherapies and molecularly-targeted therapies have not provided the same success in PDAC as they have seen in other carcinomas (8). Therefore, there is a clear and urgent need to develop improved therapies for PDAC.

In an effort to understand inter-tumoral heterogeneity in disease progression and treatment response, patient bulk tumor transcriptomics have been utilized to determine subtypes within PDAC, with the three major classification systems being those attributed to Moffit, Collisson, and Bailey (9-11). Moffitt et al. classifies tumors into classical and basal-like subtypes, with the basal subtype having the worse prognosis and enrichment of mesenchymal characteristics (9). The Collisson method defines three subtypes of classical, quasimesenchymal, and exocrine-like, where quasimesenchymal tumors have the shortest median survival among the subtypes (10). Lastly, the Bailey classification defines four subtypes: squamous, pancreatic progenitor, immunogenic, and aberrantly differentiated endocrine exocrine, based on histopathological characteristics, with the squamous population having the worst prognosis and

an increase in mesenchymal characteristics (11). Therefore, each of these methods for classifying PDAC tumors identifies an especially aggressive subtype that is associated with decreased survival and mesenchymal characteristics. However, these subtyping methods were defined from bulk tumor transcriptomics, which does not account for heterogeneity within the tumor.

1.2 EPITHELIAL-MESENCHYMAL TRANSITION

Epithelial-mesenchymal transition (EMT) is a normal developmental and wound healing process by which cells lose their polarity and cell-cell adhesions to become more motile and invasive. EMT is associated with the earliest stages in metastasis and promotes chemoresistance in a variety of carcinomas, including PDAC (12-14). The epithelial phenotype is associated with expression of E-cadherin, certain cytokeratins, and zonula occludens-1 (ZO-1), which are lost as cells transition to a mesenchymal state **(Figure 1.1)** (15). The mesenchymal phenotype can involve expression of vimentin, fibronectin, and N-cadherin, and can alter the cytoskeleton to allow for migration (16). EMT is predominantly regulated by key transcription factors (TFs), including Slug, Snail, Twist, and Zeb1 (17). Although these are all known to drive EMT, they serve non-redundant functions (18). The downstream targets of the EMT-TFs are different, as they contain different DNA recognition patterns (18). For example, in breast cancer, ZEB1, but not Slug, promotes transcription of the receptor tyrosine kinase *AXL* (18).

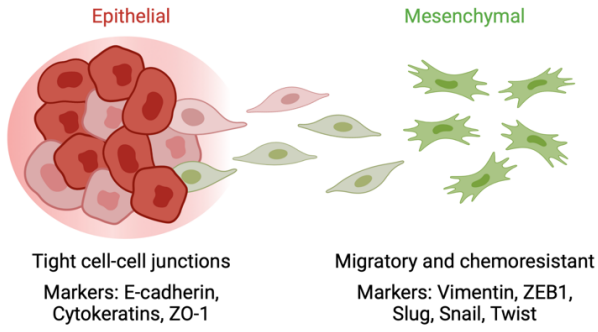

Figure 1.1 Schematic of EMT
EMT is associated with a loss of junctional proteins, including E-cadherin, and a gain of mesenchymal-associated proteins, including vimentin. Figure created with BioRender.com.

EMT is associated with poor tumor differentiation, which is a hallmark of a higher-grade carcinoma (19,20). Circulating tumor cells (CTCs) are detected in the majority of PDAC patients, and the presence of mesenchymal-CTCs is positively correlated with higher PDAC stage, metastasis, and decreased reoccurrence-free survival (21,22). Lineage tracing in an autochthonous PDAC mouse model (KPC, which generates pancreas-specific mutation in *Kras* and a deletion of one allele of *p53*) shows that a subset of CTCs maintain a mesenchymal phenotype, which ultimately seed the liver (13). KPC epithelial cells labeled with a $Rosa^{YFP}$ allele creates a KPCY mouse model that allows for tracing of cells of epithelial origin (13). This model allowed for the conclusion that EMT occurs in premalignant lesions and becomes invasive before histological evidence of PDAC (13). Further, mesenchymal PDAC cells are more resistant than epithelial cells to chemotherapy, and silencing Zeb1 can restore drug sensitivity (23). Therefore, EMT has a clinical relevance in aggressive disease and the ability to reduce EMT could improve the therapeutic window of chemotherapies in PDAC.

1.3 MULTIVARIATE SIGNALING AND EPIGENETIC REGULATION OF EMT

EMT can be driven by a variety of exogeneous stimuli that activate a multitude of signal transduction pathways, which ultimately control gene expression **(Figure 1.2)**. Signaling can be initiated from many soluble factors, such as cytokines and growth factors (e.g., TGFβ, EGF, TNFα, IL-6) which can originate from the tumor microenvironment (24,25). TGFβ is perhaps the most potent and commonly described initiator of EMT, with it routinely being used as an *in vitro* EMT-driver (26-28). Other extracellular cues include Wnt signaling through β-catenin, Notch receptor nuclear localization, Hedgehog signaling, and matrix interactions (25). These external stimuli can activate intracellular signaling pathways including MAPK and PI3K/AKT, which will ultimately impact EMT-regulating transcription factors (i.e., Snail, Slug, Twist, Zeb1) to downregulate epithelial genes, such as E-cadherin (25).

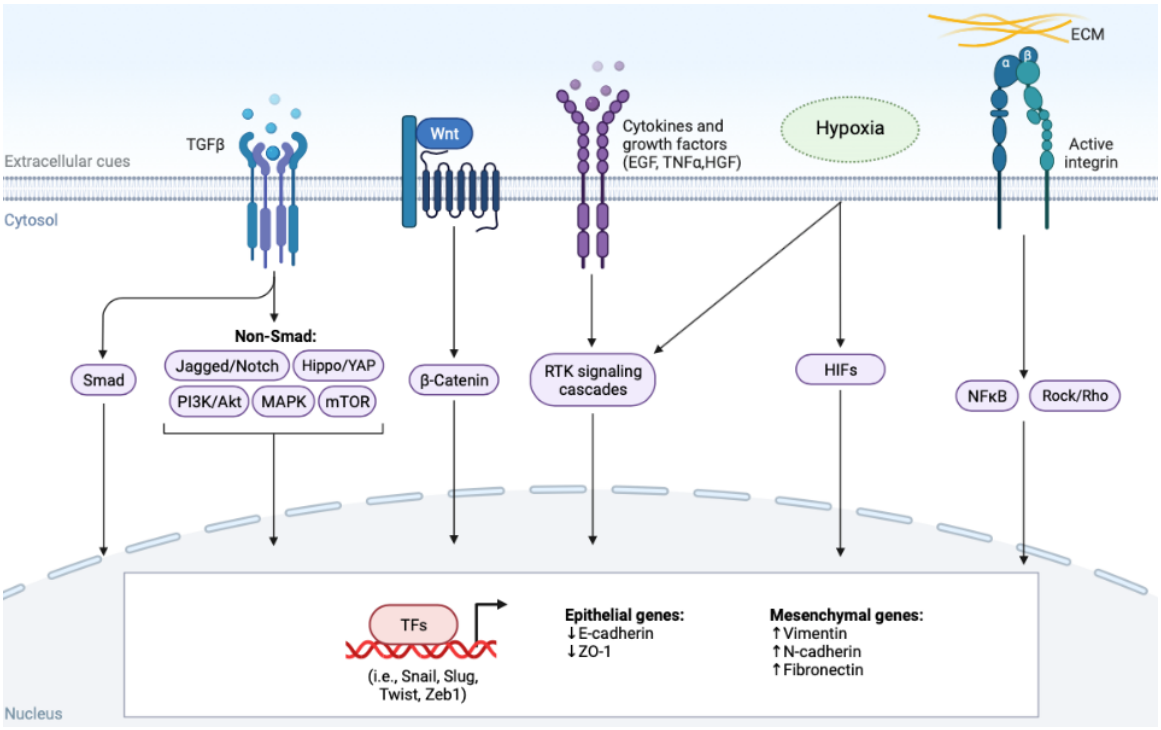

Figure 1.2 EMT is induced through signal transduction pathways
Extracellular cues activate intracellular signal transduction to promote expression of EMT transcription factors. This is a summary of key pathways but not an exhaustive list of all signaling pathways involved in EMT or the crosstalk between pathways. Figure created with BioRender.com.

Single-cell RNA sequencing (scRNA-seq) of lung, prostate, breast and ovarian cancer cells treated with TGFβ, EGF, and TNFα over a time course revealed the context dependence of cell signaling in EMT, based on minimal overlap of differentially expressed genes between treatments within a cell line and between cell lines for a particular treatment (29). In the same study, a panel of kinase inhibitors was used to demonstrate inhibition of multiple targets, including TGFβR1, EGFR, MEK, and RIPK1, had varying effects on preventing EMT in response to the three different ligands (29). Further, in TGFβ-treated breast cancer cells, scRNA-seq revealed that cells progress through EMT at different paces (30), and mechanistic modeling of single-cell mass spectrometry revealed network rewiring of both ERK and AKT pathways (31). Previous work from our lab identified a more complete EMT when cells were treated with EGF in addition to

TGFβ by engaging SHP2 (32). Therefore, drivers of EMT are activating numerous signaling pathways to create a network of multivariate signaling regulation of EMT.

Epigenetic changes can also regulate EMT. Epigenetic alterations are stable through multiple cell divisions, and DNA methylation patterns can serve as a form of cell memory (33). In PDAC, dysregulation of the histone methyltransferase Nsd2 and the demethylase Kdm2a allow for increased dimethylation of histone 3 lysine 36 (H3K36me2) to act upstream of *Snai1* and *Zeb1* (34). Additional histone modifications (e.g., methylation, acetylation), such as H2K27me3, H3K4me2, and H3K4Ac, have also been reported to regulate EMT-associated genes (35,36). However, there is a lack of understanding in the literature of the interplay between signal transduction pathways and epigenetic modifications and the resulting ability to drive EMT.

1.4 COMPLEX TUMOR MICROENVIRONMENT OF PANCREAS CANCER

PDAC tumors have a rich desmoplastic stroma, accounting for up to 90% of the tumor volume (37) and comprised of tumor-associated immune cells and cancer-associated fibroblasts (CAFs) that reside in an extracellular matrix (ECM) of secreted proteins **(Figure 1.3)** (38). This dense PDAC stroma, along with hypovascularity, gives rise to tumor subdomains of low oxygen tension (39-42). Recently, there has been a greater appreciation for the role the complex tumor microenvironment can play in tumorigenesis and EMT **(Figure 1.4)**.

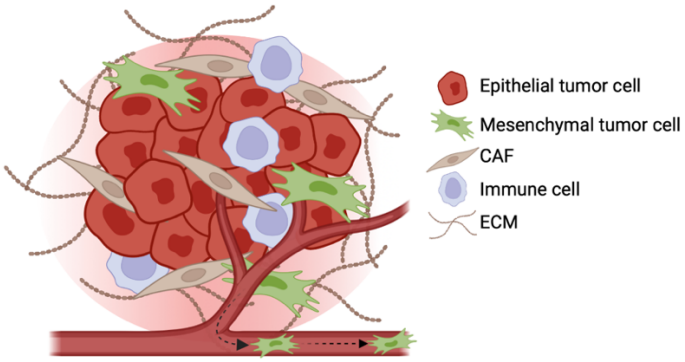

Figure 1.3 The tumor microenvironment promotes EMT in neoplastic cells
The complex tumor microenvironment is comprised of cancer-associated fibroblasts (CAFs), tumor-associated immune cells (e.g., macrophages and neutrophils), extracellular matrix [(ECM), e.g., collagens,

fibronectin, laminins] that impact epithelial and mesenchymal tumor cells. The arrows indicate disseminating mesenchymal cells. Figure created with BioRender.com.

Immune cells, such as tumor-associated macrophages (TAMs) and tumor-associated neutrophils (TANs), impact neighboring tumor cells through secretion of proteins. TAMs can be classified as M1 (anti-tumor, pro-inflammatory) or M2 (pro-tumor, anti-inflammatory), where M1-type secrete inflammatory cytokines (e.g., IL-1, TNFα) and M2-type secrete immunosuppressive cytokines (e.g., TGFβ, IL-10) (43). For example, TAMs produce hepatocyte growth factor (HGF) and proteolytic matrix metalloproteinases (MMPs) (38). Secretion of these extracellular proteins can promote EMT in tumor cells.

CAFs are activated resident pancreatic stellate cells and have been classified into two main subtypes: myofibroblastic CAFs (myCAFs) and inflammatory CAFs (iCAFs). There is recognition of other CAF subtypes including antigen-presenting CAFs and mesenchymal stem cell CAFs (38). The myCAF subtype is associated with expression of α-smooth muscle actin and matrix components (44). The iCAF subtype can be induced via IL-1α and is characterized by secretion of inflammatory cytokines (e.g., IL-6, CXCL12), which can promote EMT via JAK/STAT in tumor cells (38,45). CAFs are able to promote EMT directly through secreted factors and by contributing to the ECM by laying down collagens, fibronectin, and laminin (46-48).

Additionally, the stiffness of the ECM can contribute to tumor cell fate. The PDAC ECM is comprised primarily of collagens, with type I and III being the most abundant (48). Integrins are able to interact with collagen, fibronectin, and laminins to initiate intracellular signaling, such as Src-family kinase and JNK signaling (48). The binding of ECM proteins with dimerized integrins allows for formation of focal adhesions (48), with focal adhesion formation proportionate to external mechanical force (49). Therefore, a stiff ECM will constantly engage these adhesion pathways to promote signaling that drives EMT.

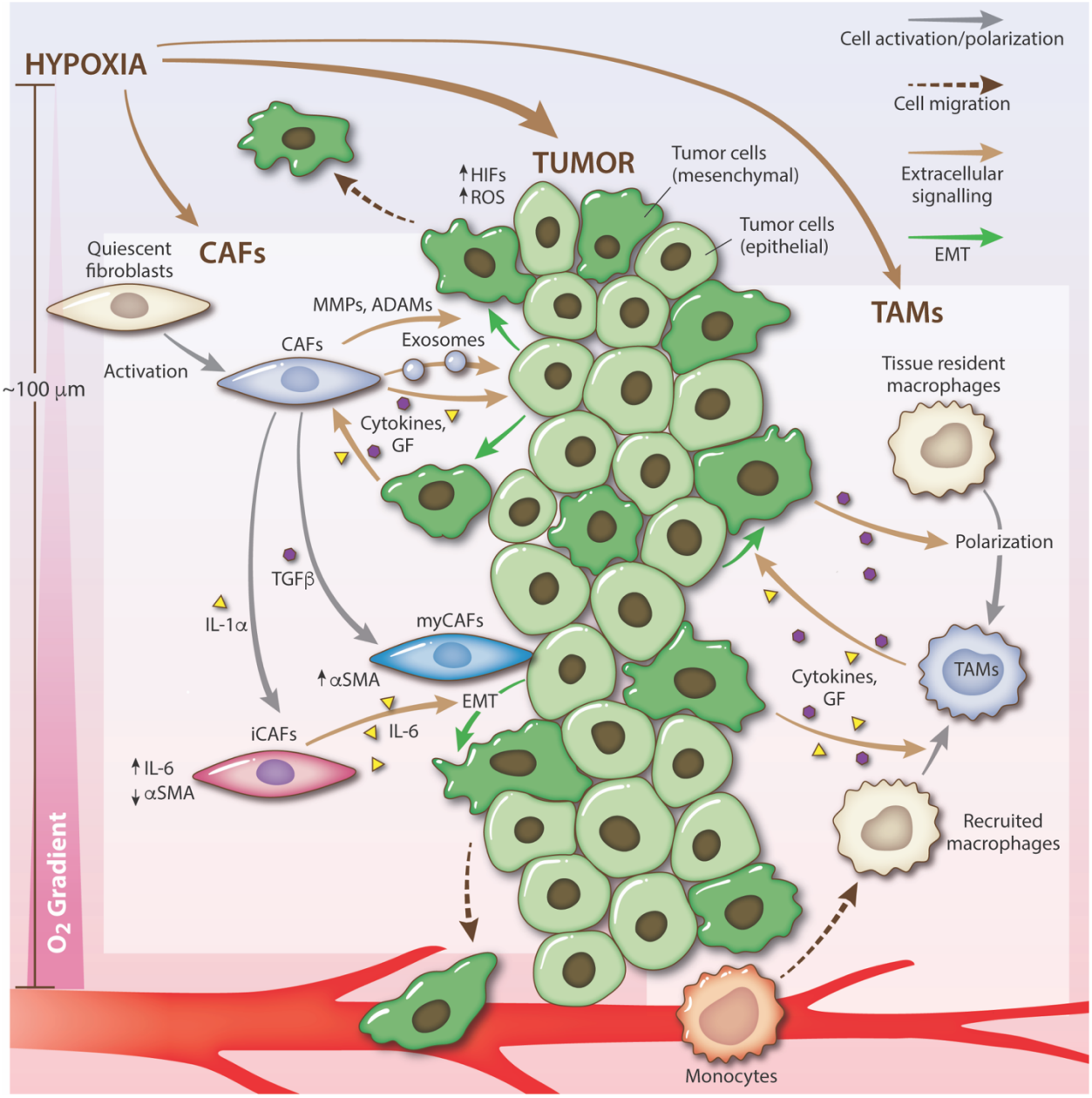

Figure 1.4 The tumor microenvironment promotes EMT through a variety of stimuli

Non-transformed tumor cells such as cancer associated fibroblasts (CAFs) and tumor-associated macrophages (TAMs) and hypoxic regions created by the diffusional limitations of oxygen (50,51) can participate in driving EMT in the cancer cell compartment. In the context of the tumor, fibroblasts are activated to become CAFs, which secrete cytokines and growth factors, release exosomes, and metalloproteinases that can all drive the neighboring tumor cells to undergo EMT. In some tumor settings, such as pancreas cancers, CAFs exist in subpopulations, including inflammatory CAFs (iCAFs) that secrete growth factors and cytokines which may drive EMT and myofibroblast-like CAFs (myCAFs). Tissue-resident macrophages, as well as recruited macrophages, are polarized to release cytokines and growth factors that cause cancer cells to undergo EMT. HIFs = hypoxia-induced factors; ROS = reactive oxygen species; MMPs = matrix metalloproteinase; ADAMs = disintegrin metalloproteases; TGFβ = transforming growth factor beta; IL-1α = interleukin 1 alpha; IL-6 = interleukin 6; αSMA = alpha smooth muscle actin; EGF = epidermal growth factor; TNFα =tumor neurosis factor alpha. This figure is part of the submitted paper,

Brown BA, Barbeau MC, Hart WS, Kowalewski K, Lazzara MJ, Regulation of epithelial-mesenchymal transition within the tumor microenvironment.

1.5 ROLE OF HYPOXIA IN PANCREAS CANCER

Hypoxia is defined as a state of reduced oxygen availability or decreased oxygen partial pressure (O_2 tensions, pO_2 values). Cells that are farther than approximately 70 μm from a blood vessel experience *diffusion-limited hypoxia* due to decreased oxygen supply, creating chronic hypoxia **(Figure 1.5A,B)** (51,52). Tumors can also have perfusion-limited O_2 delivery to create *ischemic hypoxia*, which is an acute, transient hypoxia due to abnormal structure and function of microvessels (52). Additionally, patients can experience *anemic hypoxia* which decreases the ability of oxygen transport capacity in the blood, ultimately lowering the oxygen supplied to the tumor (52,53). Almost half of cancer patients experience anemia, which can be caused by the tumor itself, or from treatments of myelosuppressive chemotherapy or radiation (54-56). Therefore, many carcinomas, including PDAC, have lower oxygen availability than the surrounding normal tissue (39,57,58). The pancreas has a median oxygen level of 6.8%, whereas, pancreas tumors have a median oxygen level of 0.4%, a close to 20-fold decrease in the abundance of oxygen (39). Evidence of hypoxia can be found as early as the pancreatic intraepithelial neoplasia (PanIN) stage in PDAC (59).

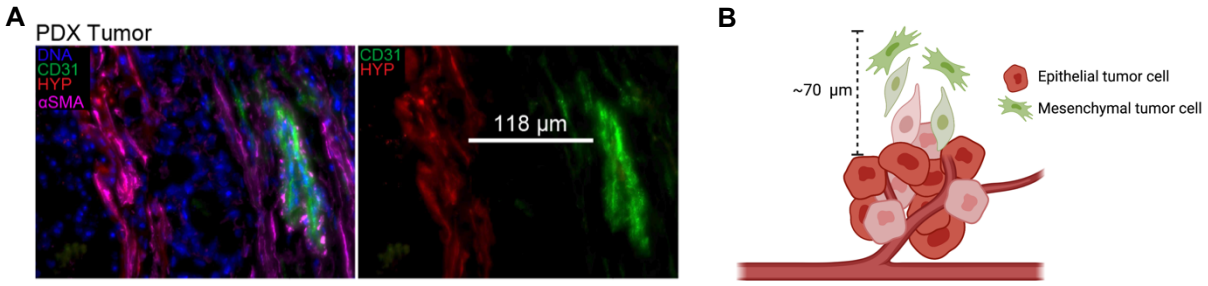

Figure 1.5 Hypoxia in PDAC
(A) Immunohistochemistry of a pancreas tumor section from a patient-derived xenograft (PDX 395) stained for CD31, α-smooth muscle actin (αSMA), and hypoxia (HYP). **(B)** Schematic of diffusion-limited hypoxia promoting EMT. Figure created with BioRender.com.

Considerable reductions in oxygen availability can impact transcriptional programs, which in part is regulated by hypoxia-inducible factors (HIFs). Decreased oxygen results in suppression of the hydroxylation and ubiquitination of the α subunits of the three HIF isoforms (HIF-1α, HIF-2α, and HIF-3α) to allow for HIF protein stabilization, which directly links oxygen abundance to transcriptional regulation (60). A hypoxic environment also promotes mitochondrial reactive oxygen species (ROS), such as superoxide and hydrogen peroxide, by a transfer of electrons from a free radical state to molecular oxygen in the electron transport chain (61,62). ROS can activate signaling by oxidizing target molecules, such as phosphatases and transcription factors (61,62). Further, some histone demethylases containing the Jumanji-C domain, can directly sense oxygen, which impairs their activity to allow for increased histone methylation and resulting changes in gene expression (63,64). To date, at least two histone demethylases, KDM5A and KDM6A, have been identified to exhibit substantially variable activities over (patho)physiological ranges in oxygen tension (63,64).

These transcriptomic changes allow for phenotypic changes in low oxygen. Hypoxia causes rapid tumor growth, spontaneous metastasis, and resistance to chemotherapies in PDAC (65,66). Analysis of transcriptomic data from The Cancer Genome Atlas (TCGA) reveals that *HIF1A* was positively correlated with EMT signatures in nine cancer types, including PDAC (65). Further, head and neck squamous cell carcinoma tumors show co-expression of HIF-1α with Twist and Snail (67), and PDAC tumors show co-expression of carbonic anhydrase, a protein up-regulated by hypoxia, with vimentin and Twist2 (68). Conversely, excess oxygen *in vivo* causes mesenchymal-epithelial transition (MET), measured by an increase in epithelial genes and a decrease in mesenchymal genes (69).

Some of the proposed mechanisms of hypoxia-mediated EMT include HIF-1α-dependence through, for example, HIF-1α- binding directly to the hypoxia response element on the *TWIST* promoter and HIF-1α promoting expression of lysyl oxidase to stabilize Snail (67,70).

ROS can also drive EMT, both indirectly and directly. Attenuation of ROS by the antioxidants N-acetylcysteine (NAC) and ebselen suppresses expression of Snail, Slug, and Twist in hypoxic cancer cells. The antioxidant NAC also abrogates the activation of HIF-1α and NF-κB during hypoxia, which both play an active role in hypoxia-driven EMT (62). Additionally, ROS play a critical role in signaling by receptors such as the epidermal growth factor receptor by targeting protein tyrosine phosphates to promote tumor progression and drug resistance (61).

Although some studies have identified a potential connection between hypoxia and EMT and identified some relevant signaling pathways, there has yet to be a systematic study of hypoxia-driven EMT signaling or a study that broadly profiles transcriptional programs involved in hypoxic response and EMT simultaneously. While there is significant *in vitro* evidence of hypoxia-driven EMT, the *in vivo* relevance of hypoxia for EMT in PDAC still needs to be studied further. Additionally, it will be worth understanding the capacity for hypoxia to drive EMT compared to other agonists (e.g., growth factors). Further, the most critical signaling effector pathways that are common to multiple agonists of EMT, which would provide the most readily accessible targets of inhibition, are unknown. In this work, we plan to find targetable pathways to prevent hypoxia-driven EMT.

When discussing hypoxic cell culture to compare to *in vivo* measurements, it is important to note that traditional cell culture is conducted in a humidified 37°C incubator with 5% CO_2, and thus operates at an oxygen percentage closer to 18.6% O_2, rather than that of dry air of 20.9% O_2 (71). Additionally, although the incubator is operating at that bulk oxygen level, the cells under a layer of medium may experience a lower oxygen level due to diffusional limitations and oxygen consumption from cells (71,72). With these caveats, oxygen-dependent studies can still be conducted by allowing for all other parameters to be the same and creating a substantial enough difference in bulk oxygen so that any differences can be attributed to the differential oxygen levels (71).

1.6 PLASTICITY AND HETEROGENEITY IN EMT

EMT is a highly dynamic process that results in phenotypic plasticity and heterogeneity of EMT states within a population (17). Thus, cells do not exist only as binary states of epithelial (E) or mesenchymal (M), but rather cells exist on a spectrum in which hybrid/intermediate phases exist with cells co-expressing E and M markers (73). Some have defined a partial EMT as a program that involves internalization of E-cadherin, whereas a complete EMT requires transcriptional repression of epithelial genes (19). Partial EMT could be even more detrimental than a complete EMT for metastasis, as cells still harbor epithelial characteristics allowing for a collective migration and the ability to seed a metastatic site, but both partial and complete EMT promote chemoresistance (74).

EMT heterogeneity can arise from extrinsic factors including a nonuniform tumor microenvironment. As previously described, the stromal compartment can promote EMT; therefore, the distribution of cell types within the tumor can dictate the neighboring tumor cell phenotype. In pancreas cancer, myCAFs were found to be adjacent to neoplastic cells more so than the cytokine-secreting iCAFs (45). This intra-tumoral spatial heterogeneity in the tumor microenvironment can create gradients in diffusible ligands and oxygen. Hypoxic subdomains arise from diffusional limitations. Thus, cells proximal to blood vessels do not experience hypoxia and the resulting consequences.

Heterogeneity in gene expression and signal transduction across cells can yield baseline differences in E and M states within a population and can also make a cell more susceptible to undergoing EMT. HGF stimulation of *in silico* cells produced differential responses that were determined to be dependent on the network of MEK/ERK and PI3K/AKT within the cells (75). In a lung cancer cell line, patterns of basal signaling heterogeneity across clones correlated with drug sensitivity (76), and in colon cancer cells, baseline differences in signaling activity among

cells correlated with the baseline EMT state (77). Therefore, identification of genetic differences in susceptibility to undergo EMT could provide insight into targetable mechanisms.

1.7 THESIS SUMMARY

Given the dismal survival rate of PDAC, there is an urgent need to provide improved therapeutic options to patients. Due to the chemoresistance of PDAC and the role of EMT in chemoresistance, methods to target EMT may allow for improved therapeutic response and ultimately improved patient survival. While tumor hypoxia has been associated with especially poor PDAC patient outcomes, the mechanisms through which hypoxia impacts tumor progression are incompletely understood. An association between hypoxia and EMT has been proposed, but a definitive mechanistic connection has not been established, and the frequency with which hypoxia is associated with EMT in PDAC is unknown. This thesis addresses the relationship between EMT and hypoxia in PDAC and analyzes the ability of the hypoxic tumor microenvironment of PDAC to promote EMT through multivariate signaling.

In Chapter 2, we performed a comprehensive study of the relationship between hypoxia and EMT in PDAC and identified an integrated kinase signaling and epigenetic mechanism that leads from low oxygen tension to EMT. The study utilizes four PDAC mouse models, transcriptomic and proteomic human patient data, and neoplastic PDAC cells derived from human and mouse tumors. Murine mouse models include orthotopic patient-derived xenografts, the autochthonous lineage-traced KPCY model (*LSL-Kras*^{G12D}; *p53*^{R172H}; *Pdx1-Cre*; *Rosa26*$^{LSL\text{-}YFP}$), subcutaneous tumors formed by KPCY-derived cell lines, and orthotopically implanted human PDAC cells engineered with a hypoxia fate mapping system. Human and murine PDAC cells were used to conduct biochemical and phenotypic measurements in normoxic and hypoxic culture conditions to definitely show hypoxia promotes a *bona fide* EMT. Hypoxia-mediated EMT is found to be substantially more durable than growth factor-mediated EMT, and the mesenchymal state

is more heritable when driven by hypoxia. Neoplastic cells that undergo EMT in response to hypoxia can retain mesenchymal characteristics for weeks, and once-hypoxic cells in tumors retain mesenchymal characteristics outside the local hypoxic environment. We determined that the activity of the histone demethylase KDM2A is highly oxygen-dependent and propose it as playing a critical initiating role in hypoxia-mediated EMT. Furthermore, data science models based on human tumor transcriptomics and proteomics were used to probe for relationships between hypoxia and EMT, to nominate hypoxia-activated signaling pathways, and to confirm the relevance of transcript or protein alterations identified in cell culture studies. We identified ERK and JNK pathways as druggable targets whose simultaneous antagonism prevents, and even reverses, the effects of a microenvironment-initiated phenotypic transition that occurs early in tumor dissemination and promotes chemoresistance.

In Chapter 3, we sought to compare the EMT drivers of hypoxia and growth factors and studied heterogeneity in EMT through data-driven modeling of scRNA-seq. Analysis of the significantly differentiated genes allowed us to identify promoters of both mesenchymal and epithelial states. We exposed pancreatic cancer cells to hypoxia or the growth factor combination of TGFβ+HGF, and then subjected cells to scRNA-seq comparing to a control condition. Through unbiased clustering, we found that cells generally organized into their experimental treatment condition with genes associated with hypoxia, proliferation, and EMT being the most dominant distinguishing features among the clusters. To address the role of EMT directly, we clustered the full data set of all conditions on an EMT-associated gene set to generate two groups of cells identified as epithelial (E) or mesenchymal (M). By performing gene set variation analysis on signaling pathways, it was determined that the Hippo pathway was the most differentially enriched between the E and M clusters, with substantial upregulation in the epithelial cells. To elucidate the differential regulation of EMT across the different drivers, we clustered on the EMT-associated genes within each original treatment condition. We determined that *FAT1* was enriched in the E

clusters across all three experimental treatments. We validated this finding *in vitro* by knocking down FAT1 and measuring the resulting increase in vimentin, at the transcript and protein level, and decrease in *CDH1*. Given the reported role of FAT1 in assembling the Hippo pathway, we tested the effects of FAT1 knockdown and identified a resulting increase in nuclear YAP accumulation. Further, we identified a context-dependent role of AXL in hypoxic mesenchymal cells. Specifically, AXL inhibition only prevented EMT in hypoxia and not in the presence of growth factors. Interestingly, at the protein level, nuclear AXL was enriched in vimentin-positive hypoxic cells, as well as in nuclear YAP-positive cells. To connect this back to Chapter 2, we demonstrated that MEK and JNK inhibition rescued *FAT1* expression in hypoxic cells. We were able to validate the role of *FAT1* and *AXL* in patient tumor scRNA-seq data. Thus, this chapter utilizes computational data analysis methods to generate testable hypotheses for understanding heterogenous EMT.

In Chapter 4, we provide perspective on the clinical implications of these findings and recommend future work to accompany these studies. EMT is being explored in the clinical setting by informing treatment plans based on the phenotypic state of the tumor and as a target to improve therapeutic response. Classification of patient tumors as basal or classical could provide insight into responsiveness to chemotherapy and inform the selection of patient populations for clinical trials. One of the biggest challenges facing pancreatic cancer treatment is the impact of tumor heterogeneity. As we explored in Chapter 2, even within a cell line there is significant genetic heterogeneity that leads to phenotypic heterogeneity. We identified a potential therapeutic target of AXL in the specific context of hypoxic mesenchymal cells. Additionally, the interesting finding of differential nuclear AXL expression is an area that requires more exploration of its mechanistic role in promoting EMT. Lastly, the work presented in this thesis could eventually be translated to new investigational combination therapies aimed at antagonizing EMT with molecularly targeted drugs in combination with chemotherapy. Indeed, Chapter 2 identifies a

synergistic effect of MEK and JNK inhibition on suppressing hypoxia-mediated EMT, and the work in Chapter 3 identifies a potentially druggable AXL/YAP signaling axis as critical for explaining the heterogeneous EMT driven by hypoxia. In order to succeed in leveraging these findings in combination therapy approaches, additional work needs to be conducted to identify strategic dosing regimens to allow for optimal response while minimizing adverse effects of additive drugs.

CHAPTER 2: A HISTONE METHYLATION-MAPK SIGNALING AXIS DRIVES DURABLE EPITHELIAL-MESENCHYMAL TRANSITION IN HYPOXIC PANCREAS CANCER[1]

2.1 ABSTRACT

Here, we show that hypoxia drives especially long-lasting epithelial-mesenchymal transition (EMT) in pancreatic ductal adenocarcinoma (PDAC) primarily through a positive-feedback histone methylation-MAPK signaling axis. We find that neoplastic PDAC cells preferentially undergo EMT in hypoxic tumor regions in multiple model systems and that hypoxia drives a cell-autonomous EMT in PDAC cells which, unlike EMT in response to growth factors, can last for weeks. We further demonstrate that hypoxia reduces histone demethylase KDM2A activity, suppresses PP2 family phosphatase expression, and activates MAPKs to post-translationally stabilize histone methyltransferase NSD2, leading to an H3K36me2-dependent EMT in which hypoxia-inducible factors play only a supporting role. This mechanism can be antagonized *in vivo* by combinations of MAPK inhibitors that may be effective in multi-drug therapies designed to target EMT.

[1] A version of Chapter 2 is under revision at *Cancer Research*, Brown BA, Myers PJ, Adair SJ, Pitarresi JR, Sah-Teli SK, Campbell LA, Hart WS, Barbeau M, Leong K, Seyler N, Jones M, Kane W, Lee KE, Stelow E, Simon MC, Koivunen P, Bauer TW, Stanger BZ, and Lazzara MJ, A histone methylation-MAPK signaling axis drives durable epithelial-mesenchymal transition in hypoxic pancreas cancer.

2.2 INTRODUCTION

The pancreatic ductal adenocarcinoma (PDAC) microenvironment exerts complex regulation over tumor progression and response to therapy. One of the most well described features of the dense PDAC stroma is its characteristic hypovascularity, which gives rise to tumor subdomains with low oxygen concentration (39-42). Hypoxic regions are found in most or all human PDAC, with oxygen tensions as low as 0.4% (ratio of corresponding equilibrium gas-phase oxygen partial pressure to atmospheric pressure) within tumors compared to 6.8% in adjacent normal tissue (39,42). Evidence of hypoxia can be found as early as the pancreatic intraepithelial neoplasia (PanIN) stage in PDAC, and low numbers of mature blood vessels or pronounced hypoxia transcriptomic signatures portend shorter patient survival times (40,59,78). Hypovascularity and hypoxia have been proposed to reduce patient survival by limiting tumor perfusion with systemic therapies and decreasing anti-cancer immune cell infiltration (40). In patient-derived xenografts (PDX), hypoxia correlates with increased PDAC tumor growth and spontaneous metastasis (65). Hypoxia has also been proposed as a driver of epithelial-mesenchymal transition (EMT) (79-84), a cell developmental process that occurs aberrantly in PDAC as early as the late PanIN stage and has been linked to chemoresistance and poor tumor differentiation (13,19,85).

Each of the common methods for classifying PDAC tumors has identified an especially aggressive subtype that is enriched for mesenchymal characteristics and associated with decreased survival (9-11). There are many known drivers of EMT, but cytokines and growth factors including transforming growth factor β (TGFβ) and hepatocyte growth factor (HGF) are perhaps the best known (15). It was recently discovered that complete TGFβ-mediated EMT in PDAC cells involves dimethylation of H3K36 mediated by loss of histone demethylase KDM2A and upregulated expression of histone methyltransferase NSD2 (34). Hypoxia can also promote epigenetic rewiring through histone methylation (86), but the possibility that such regulation

impacts EMT has not been fully explored. Interestingly, at least two histone demethylases, KDM5A and KDM6A, exhibit substantially variable activities over (patho)physiological ranges in oxygen tension (63,64), raising the intriguing possibility that EMT could be controlled via an entirely intracellular mechanism independent of cytokines. One recent study identified a mechanism involving KDM5A and the NADPH oxidase NOX4 that promoted H3K4 trimethylation to regulate *Snail* expression in PDAC (81), but the signaling mechanisms involved were not investigated.

The potential mechanistic connections between hypoxia and EMT notwithstanding, direct evidence for hypoxia as a driver of EMT in PDAC is limited. Some studies have highlighted the role HIFs could play in PDAC EMT through HIF-1α-induced *Twist* expression (80), HIF-1α/YAP1 interactions (79,83), or HIF-2α crosstalk with Wnt/β-catenin (84). Further, transcriptomic analyses have identified a correlation between hypoxia-inducible factor-1α (*HIF1A*) expression and EMT in PDAC (85). However, given that *HIF1A* is only one target affected by hypoxia and that it is primarily post-translationally regulated, individual transcript measurements provide limited insight. Moreover, the connection between hypoxia and specific signaling pathways that may promote EMT is largely unexplored. More specifically, whether a potential hypoxia-driven EMT might occur via the same pathways that are important for growth factor-mediated EMT is unclear. MAPKs have been proposed as some of the most critical regulators of growth factor-driven EMT (15,32), but the potential relevance of MAPKs in hypoxic PDAC cells and tumors for driving EMT has not been thoroughly investigated, either experimentally or through the analysis of publicly-available patient data.

Here, we demonstrate that hypoxia promotes a *bona fide* EMT in PDAC via an integrated mechanism involving histone methylation and MAPK signaling that can be pharmacologically inhibited. Through the analysis of multiple types of human patient data, we demonstrate that the relationship between hypoxia and EMT in PDAC is so typical that statistically significant

relationships between EMT and hypoxic gene signatures can be identified. Through use of multiple mouse models and cell culture studies, we find that hypoxia-mediated EMT occurs in both a cell-autonomous fashion and in the tumor microenvironment, and that hypoxia drives a more durable EMT than growth factors. The identification of MAPK signaling as indispensable for hypoxia-mediated EMT nominates specific targeted inhibitors for combination therapy approaches that could promote chemoresponse by antagonizing EMT.

2.3 METHODS

2.3.1.Data Analytic and Computational Modeling Methods

Acquisition of publicly available datasets

CPTAC PDAC Discovery Study data (78) were generated by the Clinical Proteomic Tumor Analysis Consortium (NCI/NIH). Clinical information and tumor histology data were obtained from the same publication, and the processed proteomics data were downloaded from the LinkedOmics data portal. CPTAC data are also available through the Proteomic Data Commons. Links to publicly available data and software used are in **Supp Table 2.S1**. To maximize the number of proteins retained for consensus clustering of the pcEMT signature, imputation was performed on the CPTAC global proteomics gene-level data for all proteins with non-missing values in at least 50% of samples using the DreamAI algorithm (87), which was designed specifically for proteomics data. DreamAI was used with default settings.

TCGA PAAD RNA-seq gene expression data (data set ID: TCGA.PAAD.sampleMap/HiSeqV2; version: 2017-10-13) were downloaded from the UCSC Xena Browser as $\log_2$(RSEM+1) normalized counts and were converted first to transcripts per million (TPM) and finally to $\log_2$(TPM+1) for all analyses unless otherwise noted. Curated TCGA PAAD phenotype and survival data were also downloaded from UCSC Xena. Only PDAC tumors were retained for analysis, as determined based on provided histology annotations (150 tumors). Annotated and pre-processed PDAC scRNA-seq data from (88) were kindly provided by Dr. David Tuveson (Cold Spring Harbor Laboratory). The code used to analyze the publicly available omics data can be accessed here: https://github.com/lazzaralab/Brown-et-al_PDAC-hypoxia-EMT. R version 4.1.2 was used for all analyses.

Gene sets and signatures

The pan-cancer EMT signature (89) was used as the primary feature set for clustering based on EMT markers. The HIF target signature (90) was used as the primary feature set for clustering based on hypoxia markers. Gene sets from the Molecular Signatures Database (MsigDB) including Hallmark Hypoxia (91) were accessed within R using the *msigdbr* package, and gene sets from the Kyoto Encyclopedia of Genes and Genomes (KEGG) (92,93) were accessed within R using the *clusterProfiler* package.

Immune deconvolution of TCGA RNA-seq data

Cell-type-specific immune deconvolution of bulk TCGA PAAD data was performed using the *immunedeconv* R package (94) and EPIC algorithm (95). EPIC was selected because of its reported superior performance over other algorithms for most cell types (94) and because it estimates absolute fractions of cell types, including cancer-associated fibroblasts and neoplastic cells.

Clustering of tumor-derived bulk and single-cell omics data sets

Non-negative matrix factorization (NMF) clustering of bulk tumor data from TCGA (RNA-seq) and CPTAC (mass spectrometry) was performed with expression data for all available genes or proteins, respectively, from the pcEMT signature using the *NMF* R package (96) and the standard NMF algorithm based on the Kullback-Leibler divergence (97). For CPTAC data, the imputed version of the data was used to retain as many proteins as possible for clustering since NMF requires non-negative, non-missing data. The optimal NMF factorization rank k (i.e., number of clusters) was selected using an approach similar to that described previously (78). First, a range of clusters from $k = 2$ to 10 was tested by: (i) performing 100 iterations of NMF with random initializations of the NMF matrices W (basis component matrix) and H (mixture coefficient matrix); (ii) calculating the product of the cophenetic correlation coefficient, the dispersion coefficient of

the consensus matrix (98), and the average silhouette width (99) of the consensus matrix for each *k*; and (iii) selecting the optimal *k* with the maximum product of the cophenetic, dispersion, and average silhouette coefficients. Then, using the optimal *k*, the final NMF clustering was obtained by repeating the analysis with 500 iterations of random initializations of matrices *W* and *H*. The coefficient matrix *H* was used to assign samples (tumors) to clusters by identifying the cluster (row of *H*) for which each sample (column of *H*) had its maximum mixture coefficient.

Clustering of the ductal cell scRNA-seq data (88) was performed by first projecting cells onto a 2D UMAP space using gene expression data for only the mesenchymal genes from the pcEMT signature. The UMAP projection was calculated using a nearest neighbors setting of 30 and a minimum distance of 0.01 using the *umap* R package. Consensus clustering (100) was then performed on the resulting UMAP projection to assign cells to individual clusters. Consensus clustering was performed in R with *ConsensusClusterPlus* (101) using Euclidean distance as the distance metric, Ward's linkage for subsampling and as the linkage method for the consensus matrix, and partitioning around medoids (PAM) as the clustering algorithm.

Gene set enrichment analysis and pathway overdispersion analysis

Gene set variation analysis (GSVA) (102) was used to calculate sample-wise gene set enrichment scores using the CPTAC PDAC global proteome data and TCGA PAAD RNA-seq data from the and using the *GSVA* R package. For GSVA on CPTAC data, the original global proteome data were used without imputing missing values since GSVA does not require non-missing data. For GSVA on TCGA PAAD data, log-transformed transcripts per million ($\log_2$(TPM+1)) expression values were used. Pathway and gene set overdispersion analysis (Pagoda2) (103-105) was used to calculate sample-wise gene set enrichment scores for the ductal cell scRNA-seq data from (88) using the *Pagoda2* R package.

Partial correlations with pan-cancer EMT enrichment

Partial rank correlation coefficients and associated confidence intervals were computed with *ggstatsplot* in R. In all analyses, partial correlations were computed with respect to GSVA scores for the mesenchymal portion of the pcEMT signature, as calculated using the CPTAC global proteomics data or TCGA PAAD RNA-seq data as indicated in each analysis.

Phospho-kinase overrepresentation analysis

First, using the gene-level phosphorylation data (i.e., summarized over all phosphosites, as provided by the CPTAC), we filtered the data set for only kinases (358 kinases retained) and calculated Spearman rank correlation coefficients between the kinase phosphorylation levels and the Hallmark Hypoxia GSVA scores calculated from the CPTAC global proteomics expression data. KEGG pathway overrepresentation analysis was then performed on the list of positively and significantly ($p < 0.05$) correlated phospho-kinases using the *clusterProfiler* R package (106). Only the list of available kinases in the CPTAC phosphoproteomics data set was used as the set of reference genes for testing overrepresentation. *p* values from the hypergeometric test were adjusted for multiple comparisons by controlling the false discovery rate (107). Spearman correlations and *p* values were calculated using the *Hmisc* R package.

Linear modeling of human ductal cell scRNA-seq data

Least absolute shrinkage and selection operator (LASSO) regression was performed using the *glmnet* R package (108). The LASSO regularization parameter λ was determined via cross-validation using the “cv.glmnet” function with default settings and by taking the largest value of λ such that the cross-validated mean-squared error (MSE) was within one standard error of the minimum MSE. An ordinary least squares linear regression model was then trained using the LASSO-selected KEGG signaling pathways and subjected to further variable selection by

minimizing the Akaike information criterion [AIC; (109)] using the “step” R function. Finally, model statistics, including statistics for the regression coefficients of the final LASSO+AIC-selected KEGG pathways, were calculated using the base R “summary” function and were plotted using *ggstatsplot*.

Statistical analyses and visualizations of publicly available data

The *ggstatsplot* R package (110) was used to perform the Mann-Whitney U test and the Kruskal-Wallis test. Log-rank test *p* value and survival curves were generated in R using the *survival* (111) and *survminer* packages, respectively. The *ggplot2* (112), *tidyHeatmap* (113) , *ComplexHeatmap* (114) and *cowplot* R packages were used throughout this work to generate figures and plots. UpSet plots (115) were created in R using the *ggupset* package.

2.3.2.Experimental Methods

Cell culture

HPAF-II cells (Carl June, University of Pennsylvania) were authenticated by the Genetic Resources Core Facility at the John Hopkins University School of Medicine by performing short tandem repeat profiling via GenePrint 10 (Promega) and comparing to the ATCC database. HPAF-II cells and cell lines derived from human PDXs (116,117) were maintained in RPMI with 10% fetal bovine serum (FBS), 1 mM L-glutamine, 100 units/mL penicillin, and 100 µg/mL streptomycin. MiaPaca2 cells (Paolo Provenzano, University of Minnesota) were maintained in DMEM with 10% FBS, 1 mM L-glutamine, 100 units/mL penicillin, and 100 µg/mL streptomycin. Murine KPCY cells were derived from *Kras*$^{LSL\text{-}G12D}$*, p53*$^{LSL\text{-}R172H}$*, Pdx1-Cre, Rosa26*$^{LSL\text{-}YFP}$ mice (2838c3, 6499c4, 6556c6, and 7160c2; all clonal) or *Kras*$^{LSL\text{-}G12D}$, *p53*$^{loxP/+}$, *Pdx1-Cre*, *Rosa26*$^{LSL\text{-}YFP}$ mice (PD798 and PD7591) and were maintained in DMEM + GlutaMAX supplemented with 10% FBS, 1 mM L-glutamine, 100 units/mL penicillin, 100 µg/mL streptomycin, and 8.66 µg/mL

gentamicin. Cell lines were tested for mycoplasma using the MycoAlert PLUS Detection Kit (Lonza). Cells were maintained in a Thermo Scientific Forma Steri-Cycle i160 incubator at 5% CO_2 and 37ºC for normal culture. For culture at 1% or 7% O_2, cells were maintained in a Tri-Gas version of the same incubator, which displaces O_2 using N_2. While O_2 tensions < 1% have been reported in PDAC tumors, 1% is the lower limit of the incubator. For hypoxia experiments, cells were moved to the tri-gas incubator 16 hr after plating and culturing under normal 21% O_2 conditions. For chronic hypoxia experiments, medium was changed after 72 hr or every 48 hr when growth factors or inhibitors were used. Cells were treated with inhibitors immediately prior to hypoxic culture.

Growth factors and inhibitors

Recombinant human HGF and TGFβ (Peprotech) were used at 50 ng/mL and 10 ng/mL, respectively. For treatment, complete medium containing growth factors was replenished every 48 hr. The SFK inhibitor PP2 (Sigma-Aldrich) was used at 10 μM, PP2A inhibitor LB-100 (Selleck Chem) was used at 5 μM, PP2Cδ inhibitor sanguinarine chloride (MedChemExpress) was used at 1.5 μM, MEK inhibitor CI-1040 (LC Laboratories) was used at 1 μM, JNK inhibitor SP600125 (LC Laboratories) was used at 10 μM, and p38 inhibitor SB203580 (LC Laboratories) was used at 10 μM. Stocks of all inhibitors were prepared in DMSO.

Patient-derived xenograft tumors

PDAC tumor sample MAD12-395 was generated from a human tumor surgical pathology specimen coordinated through the UVA Biorepository and Tissue Research Facility, as previously described (116,117). Tumors were passaged in mice, then sewn orthotopically into 6-7-week-old female athymic nude mice (Envigo, Indianapolis, IN). For studies probing for hypoxic cells, mice were injected with pimonidazole (IP, 60 mg/kg; Hypoxyprobe, #HP7-100) 90 min prior to tumor

harvest. For paraffin embedded sections, tumors were fixed in 10% zinc buffered formalin for 24 hr, transferred to 70% ethanol, then paraffin embedded. 4-5 μm sections were cut. Paraffin embedded tumors were used throughout these studies, except for sections stained for CD31 for which frozen tumors and sections were prepared. For frozen sections, tumors were fixed in 4% paraformaldehyde for 1-3 hr, then moved to 30% sucrose overnight, and finally embedded in OCT. For analysis, 4-5 μm sections were cut on charged slides. PDX animal studies and procedures were approved by the UVA Institutional Animal Care and Use Committee. The UVA Research Histology Core performed the embedding, sectioning, and Hematoxylin/eosin (H&E) staining.

Use of kinase inhibitors in PDX models

PDX 395 tumors were allowed to grow for 6 weeks until palpable. Mice were treated with selumetinib (2.5 mg/kg, orally, twice daily; Selleck Chem), SP600125 (12 mg/kg, IP, twice daily; LC Laboratories), selumetinib+SP600125, or vehicle control. For oral dosing, vehicle was 0.5% hydroxypropylmethylcellulose + 0.1% Tween 80 in water. For IP dosing, vehicle was 5% DMSO + 15% Tween 20 in water. Hypoxyprobe administration and tumor processing was conducted as previously described.

Genetically engineered mouse models

Kras$^{LSL\text{-}G12D}$*, p53*$^{LSL\text{-}R172H}$*, Pdx1-Cre, Rosa26*$^{LSL\text{-}YFP}$ (KPCY) mice were described previously (13). Both female and male mice were used. Mice were palpated and examined for evidence of morbidity twice per week. 90 min prior to harvesting, intraperitoneal injection of tumor-bearing mice with pimonidazole at 60 mg/kg body weight was performed. Tissue was fixed in zinc formalin and paraffin embedded prior to staining. Animals were maintained and experiments were

conducted in compliance with the NIH guidelines for animal research and approved by the University of Pennsylvania Institutional Animal Care and Use Committee.

Subcutaneous tumors

Female C57BL/6J (stock no. 000664) or NOD.SCID (stock no. 001303) mice for subcutaneous tumor cell injection experiments were obtained from The Jackson Laboratory. C57BL/6J (7160c2) or mixed genetic background (PD7591) KPCY cell lines were previously described (19,118,119). Briefly, 2×10^5 cells were injected subcutaneously into mice and allowed to grow for 2-6 weeks, where 6 weeks was used unless otherwise noted. 90 min prior to harvesting, intraperitoneal injection of tumor-bearing mice with pimonidazole at 60 mg/kg body weight was performed. Tissue was fixed in zinc formalin and paraffin embedded prior to staining. Animals were maintained and experiments were conducted in compliance with the NIH guidelines for animal research and approved by the University of Pennsylvania Institutional Animal Care and Use Committee.

HPAF-II hypoxia fate-mapping orthotopic tumors

1×10^6 HPAF-II cells engineered with the hypoxia fate-mapping reporter system were injected orthotopically into 8-week-old male athymic nude mice (Envigo, Indianapolis, IN). Mice were sacrificed 5 weeks later with pimonidazole injected (IP, 60 mg/kg) 90 min prior to tumor harvest. For paraffin-embedded sections, tumors were fixed in 10% zinc buffered formalin for 24 hr, transferred to 70% ethanol, and then paraffin embedded. 4-5 μm sections were cut. Animal studies and procedures were approved by the University of Virginia Institutional Animal Care and Use Committee. The UVA Research Histology Core performed the embedding, sectioning, and H&E staining.

Cell dissociation from HPAF-II orthotopic tumors

Following sacrifice, pieces of four tumors were kept on ice to be dissociated (120). For 50 mg of tumor, 2 mL of protease solution [5mM $CaCl_2$, 10mg/mL *Bacillus Licheniformis* protease, and 125 U/mL DNAseI in Dulbecco's phosphate-buffered saline (DPBS)] was used. Over ice, tumors were minced in solution and then mechanically dissociated for 8 min using a 1 mL pipet. Samples were transferred to Miltenyi C-tubes and run on the gentleMACS tumor_01 program 3 times. Afterwards, cells were mechanically dissociated for 2 min using a 1 mL pipet. Cells were suspended in 10% FBS and EDTA in DPBS, centrifuged at 1200 g for 5 min at 4°C, and supernatant was discarded. Cells were sorted using a Becton Dickinson Influx Cell Sorter at the UVA Flow Cytometry Core Facility, with parental HPAF-II cells and engineered HPAF-II hypoxia fate-mapping cells as controls for setting gates. ToPro3 was used to determine viability. For each tumor, cells were sorted into DsRed+, GFP+, and DsRed+GFP+ populations and plated in complete RPMI following sorting.

Pathologic assessment of human PDAC tumor samples

Tumor pieces were placed in tumor blocks, fixed in zinc buffered formalin for 24 hr and embedded in paraffin. H&E staining was performed on human tumors. A board-certified pathologist specializing in pancreatic and liver pathology (EBS) reviewed all slides to assess differentiation as "moderate" or "poor."

Antibodies

Antibodies against E-cadherin (clone ECCD2, Invitrogen, 13-1900) and c-Jun (Cell Signal Technology (CST), #9165) were used for immunofluorescence and western blotting. For immunofluorescence, antibodies against HIF-1α (CST, #79233), vimentin (Santa Cruz Biotechnology, sc-373717), H3K36me2 (CST, #2901), and NSD2 (Santa Cruz Biotechnology, sc-

365627) were used. For western blotting, antibodies against HIF-1α (Novus Biologics, NB100-134), HIF-2α (Novus Biologics, NB100-122), vimentin (Santa Cruz Biotechnology, sc-373717), pc-Jun S73 (CST, #3270), pERK T202/Y204 (CST, #4370), ERK1/2 (CST, #4695), p-p38 T180/Y182, and GAPDH (Santa Cruz Biotechnology, sc-32233) were used. Alexa488-conjugated vimentin antibody (Santa Cruz Biotechnology, sc-373717) was used for flow cytometry and fluorescent immunohistochemistry for PDX and HPAF-II tumors. For KPCY tumors, antibody against vimentin (CST, #5741) was used. E-cadherin (clone ECCD2, Takara, M108), c-Jun (CST, #9165), pERK T202/Y204 (CST, #4370), CD-31 (BioLegend, 102501), α-smooth muscle actin (R&D Systems, MAB1420), GFP (Abcam, ab6673), RFP (Rockland, 600-401-379), and Hypoxyprobe™Red549 (Hypoxyprobe, HP7-100Kit) was used for immunohistochemistry. Hoechst 33342 (Invitrogen, H1399) was used for nuclear stain.

Immunohistochemistry

Slides were antigen-retrieved with high pH by the UVA Biorepository and Tissue Research Facility. Slides were then permeabilized with 0.1% Triton-X in PBS for 20 min and blocked with Intercept Blocking Buffer (IBB) (LiCor, 927-60001) for 1 hr. Primary antibody was diluted in IBB and incubated overnight at 4°C. Slides were washed with PBS and then incubated with secondary antibody diluted in IBB for 2 hr at room temperature. After washing, slides were mounted with ProLong Gold Antifade Mountant (Invitrogen). For immunohistochemistry staining of E-cadherin, a slightly different protocol was used. Slides were blocked with 5% donkey serum in 0.3% Triton-X in PBS for 1 hr, then incubated at 4°C overnight with primary antibodies. Slides were then washed twice with 0.1% Tween-20 in PBS for 5 min each, incubated with secondary antibodies for 1 hr at room temperature, and then washed again with 0.1% Tween-20 in PBS for 5 min in the dark. Slides were mounted with ProLong Gold Antifade Mountant (Invitrogen).

Western blotting

Cells were lysed using a standard cell extraction buffer with protease and phosphatase inhibitors (Sigma-Aldrich, P8340, P5726, P0044). Crude lysates were centrifuged at 14,000 rpm for 10 min at 4°C, and supernatants were removed as clarified lysates. Total protein concentration was determined with a micro-bicinchoninic acid (BCA) assay (Pierce). Equal protein amounts where combined with 10× NuPAGE reducing agent, 4X LDS sample buffer and MilliQ water to reach equal sample volumes. Samples were then heated at 100°C for 10 min and loaded onto a 1.5 mm NuPAGE gradient (4-12%) gel (Invitrogen, NP0336BOX). After electrophoresis, the gel was transferred to a 0.2 µm nitrocellulose membrane using the TransBlot Turbo Transfer System (BioRad). Membranes were blocked with diluted IBB for 1 hr on an orbital shaker. Primary antibodies diluted at 1:1000 in IBB were incubated on the membrane overnight at 4°C. GAPDH was used as a loading control. Membranes were washed with shaking three times for 5 min with 0.1% Tween-20 in PBS. Secondary antibodies were diluted 1:10,000 in IBB and incubated on the membrane with shaking for 2 hr at room temperature. Membranes were washed with 0.1% Tween-20 in PBS as before then imaged on LiCor Odyssey. Membranes were stripped with 0.2 M NaOH as needed, with confirmation by re-imaging. Image Studio software was used to quantify band intensities.

Coverslip immunofluorescence

Cells were grown on 18-mm glass coverslips. At the conclusion of the experiment, cells were fixed with 4% paraformaldehyde in PBS for 20 min and then permeabilized with 0.25% Triton-X 100 in PBS for 5 min. Coverslips were incubated with primary antibodies in a humidified chamber overnight at 4°C. Following five washes with 0.1% Tween 20 in PBS, coverslips were incubated for 1 hr at 37°C in a humidified chamber with Alexa Fluor secondary antibodies and

Hoechst nuclear stain. All antibodies were diluted in IBB. After all staining and washing steps, coverslips were mounted on glass slides with ProLong Gold Antifade Mountant.

Fluorescence microscopy and automated image analysis

Cells on coverslips were imaged using a Zeiss Axiovert Observer.Z1 fluorescence microscope, using a 10×, 20×, or 40× objective and ZEN image processing software to produce .czi files. All image comparisons were done using identical exposure times and image settings. For immunofluorescence microscopy, four frames for each biological replicate were taken at random on the coverslip. For each replicate, at least 1000 cells were quantified. For immunohistochemistry, at least eight frames per tumor section were taken, with more taken for larger sections. For image analysis, CellProfiler v3.1.9 (Broad Institute) was used to quantify signal intensity and localization (121-123). Individual cells were identified based on a nuclear stain, which served as the primary object in the analysis pipeline. For junctional E-cadherin, cells were first identified by nuclei and then the mean edge intensities were measured. For percent-positive measurements (e.g., vimentin), the threshold was set based on a negative control consisting of a sample stained with a secondary antibody only. The same threshold was applied to all images, and a percentage was calculated based on the number of cells with signal above background compared to the total cell number. For intensity measurements, the mean intensity per positive object was quantified.

Five-channel confocal microscopy

Image acquisition was performed on a Zeiss LSM 880 confocal microscope using four laser lines: 405 nm, 488 nm, 561 nm, 633 nm. Fluorophores were deconvoluted by first taking lambda stacks of singly-stained and unstained tissue sections and then by using spectral unmixing. The gallium arsenide phosphide (GaAsP) spectral array detector was tuned to 8.9 nm

to obtain 32-channel images ranging from 411 to 696 nm from which emission spectra for each of the fluorochromes were obtained. The spectral fingerprints from each of the fluorophores and from tissue autofluorescence were then used in the “online fingerprinting” mode of the ZEN Black imaging software. Images were taken using a Plan-Apochromat 20×/0.8 M27 objective.

Cell scatter measurements

GFP-expressing HPAF-II cells were engineered via second-generation lentiviral transfection with LX293T cells (Takara) using pLX302-EGFP plasmid (Kevin Janes, University of Virginia), with pCMV-VSVG and pCMV-delta8.2 as packaging plasmids. Cells were sparsely seeded in a 24-well plate, allowed to adhere for 48 hr, then t = 0 images were taken and then samples were either maintained in 21% O_2 or moved to 1% O_2 for 96 hr. Individual cell clusters (up to 20 cells by the end point) were imaged over time for six individual wells per condition. Using ImageJ, the GFP signal was used to create a binary mask of the cluster to determine the area and perimeter of each cluster to quantify the shape factor as a measure of circularity, shape factor = 4π(area/perimenter^2), where a circle = 1.

Quantitative reverse transcription PCR (qRT-PCR)

RNA was extracted using the RNeasy Kit (Qiagen, #74104) and reverse transcribed using High-Capacity cDNA Reverse Transcription Kit (Applied Biosciences, #4368814). qRT-PCR was performed using PowerUp SYBR Green (Applied Biosciences, #A25741) per manufacturer protocol using a QuantStudio3 system (Applied Biosystems). TaqMan™ Array Human Endogenous Control (Applied Biosciences, 4396840) with 32 potential housekeeping genes was run in triplicate with RNA from HPAF-II cells cultured in 21% or 1% O_2 for 120 hr. This identified *CASC3* as a gene that did not change significantly in response to hypoxia. Measurements were

analyzed with the ddCt method (124). Data are displayed as a normalized fold changes, using *CASC3* as a housekeeping gene. Primer sequences are provided in **Supp Table 2.S2**.

Flow cytometry for vimentin expression

Cells were dissociated with 0.25% Trypsin EDTA, then fixed with 4% paraformaldehyde and permeabilized with 0.25% Triton-X. Washed cells were then incubated with conjugated antibody for 30 min in the dark, and cells were resuspended in 0.1% FBS in PBS. A BD/Cytek FACS Calibur for cytometry, and FCS Express 7 was used for data analysis. Forward and side scatter were used to identify intact single cells, and data shown in main figures represent only single-cell events. 20,000 cells were counted per biological replicate, and gates were based on unstained controls. Flow cytometry was performed at the UVA Flow Cytometry Core Facility.

siRNA-mediated knockdowns

siRNAs against HIF-1α (sc-35561), EPAS-1/HIF-2α (sc-35316), c-Jun (sc-29223), and NSD2 (sc-61233), as well as a control siRNA (sc-37007), were purchased from Santa Cruz Biotechnology. siRNA against ERK 1/2 (#6560) was purchased from Cell Signal Technology. Lipofectamine RNAiMAX (Thermo Fisher) was used per manufacturer recommendations. Cells were transfected 24 hr after plating and subjected to any treatment or hypoxic culture 24 hr after transfection.

Generation of shRNA-mediated knockout cell lines

pLKO.1 plasmids encoding two non-overlapping shRNAs targeting *HIF1A* (TRCN0000003810 and TRCN0000010819) or *EPAS1* (HIF-2α) (TRCN0000003805 and TRCN0000003806), or a scrambled control, were purchased from Sigma-Aldrich. *HIF1A* and *EPAS1* plasmids carried puromycin and neomycin resistance, respectively. Second-generation

lentiviral transfection was performed in LX293T cells (Takara) with pCMV-VSVG and pCMV-delta8.2 packaging plasmids. HPAF-II cells were transduced with filtered viral supernatant with *HIF1A*-targeting plasmids, puromycin selected, then transduced with viral supernatant with *EPAS1*-targeting plasmids with 8 µg/mL polybrene.

Hypoxia fate-map cell line engineering

HPAF-II cells were engineered with a previously described fate mapping system that enables cells to switch irreversibly from constitutive dsRed to GFP expression in response to hypoxia (125). LX293T cells were transfected with the CMV-loxp-DsRed-loxp-eGFP or 4xHRE-MinTK-CRE-ODD plasmid and the psPAX2 and pMD2.G packaging plasmids. CMV-loxp-DsRed-loxp-eGFP and 4xHRE-MinTK-CRE-ODD were created by Dr. Daniele Gilkes (Addgene plasmid #141148 and #141147; http://n2t.net/addgene:141148 and http://n2t.net/addgene:141147; RRID:Addgene_141148 and RRID:Addgene_141147). psPAX2 and pMD2.G were provided by Dr. Didier Trono (Addgene plasmid #12260 and #12259; http://n2t.net/addgene:12260 and http://n2t.net/addgene:12259; RRID:Addgene_12260 and RRID:Addgene_12259). Polyjet (SignaGen, SL100688) was used to increase transfection efficiency. HPAF-II cells were first transduced with filtered viral supernatant from LX293T cells transfected with CMV-loxp-DsRed-loxp-eGFP and 8 µg/mL polybrene. After selection in zeocin (Gibco, R25001), cells were transduced with filtered viral supernatant from LX293T cells transfected with 4xHRE-MinTK-CRE-ODD in the presence of polybrene. HPAF-II cells were then cultured in 5% O_2 and single-cell sorted into 96-well plates using a Becton Dickinson Influx Cell Sorter by the UVA Flow Cytometry Core Facility, with parental HPAF-II cells used as a control for setting gates. Sorting removed GFP+ cells and retained DsRed+ cells. To increase cell viability, single-cell clones were grown in medium condition by parental HPAF-II cells and supplemented with an additional 10% fresh FBS. Once confluent, single-cell clones were split into three plates, with one maintained at 21% O_2,

one at 3% O_2, and one at 1% O_2. Plates were imaged using a Cytation5 (BioTek) with a 10× objective to screen for clones that exhibited increased GFP expression in 1% O_2 only. The selected clone was further confirmed in a larger well format for its ability to decrease DsRed expression in 1% O_2 and that the vimentin expression gained in hypoxic and growth factor culture was comparable to parental HPAF-II cells.

Plasmid cloning for recombinant expression of KDM2A

The *KDM2A* gene fused to an N-terminal FLAG tag was extracted from pcDNA-FLAG-KDM2A (Jing-Yi Chen, I-Shou University) by restriction digest with SalI-HF and XbaI and extraction of the appropriate molecular weight band using a QIAquick gel extraction kit (Qiagen). *FLAG-KDM2A* was inserted into pFastBac1 (Mark Yeager, University of Virginia) digested similarly using standard bacterial cloning techniques. The final version of the cloned plasmid was verified by Sanger sequencing (Eurofins).

Baculovirus generation, protein production, and purification

KDM2A bacmids were generated using DH10Bac competent *E.coli* cells with the standard Bac-to-Bac protocol (Invitrogen). Baculoviruses were generated by transducing the bacmid DNA into Sf9 insect cells using the flashBACTM System (Oxford Expression Technologies). Recombinant proteins were produced by infecting Sf21 insect cells with the baculoviruses for 72 hr at 27°C. The cells were homogenized in a pH 7.8 buffer containing 10 mM Tris, 150 mM NaCl, 100 mM glycine, 0.1% (v/v) Triton X-100, and a protease inhibitor cocktail tablet without EDTA. The cell lysates were centrifuged at 21,000 g for 30 min, and the soluble fractions containing the FLAG-tagged KDM2A protein were affinity purified using the anti-FLAG M2 affinity gel (Sigma). Gel beads were washed with TBS buffer (50 mM Tris, 150 mM NaCl, pH 7.4, protease inhibitor cocktail tablet without EDTA), and the proteins were eluted with TBS buffer also containing 150

μg/mL FLAG-peptide. Eluted fractions were analyzed by SDS-PAGE with Coomassie blue and western blotting using anti-FLAG M2 antibody (Sigma). Protein concentration was measured by Nanodrop, and protein was aliquoted and stored at -70°C until further use.

KDM2A kinetic assays

The kinetic assays were performed as previously described with slight modifications (126). In order to define the optimum conditions for KDM2A-catalyzed reactions, we determined the optimum reaction time and pH. In brief, the 50 μL reactions consisted of 50 mM Tris-HCl, pH 8.8, 2 mg/mL BSA (Roche), 60 μg/mL catalase (Sigma), 0.1 mM DTT, 2 mM sodium ascorbate, 10% v/v DMSO and 0.4 μM of affinity-purified KDM2A enzyme. To determine the K_M values for the histone peptide substrate H3K36me2 ((NH2-)ATKAARKSAPATGGV-(K-Me2)-KPHRYRP-GG(K-Biotin) (-CONH2)) (Innovagen), 2-oxo [1-^{14}C] glutarate (2-OG) (Perkin-Elmer), Fe^{2+}, and O_2, the enzymatic reactions were carried out by varying the concentration of the component in question while keeping the concentration of others saturating and constant. The kinetic experiment to calculate K_M for O_2 was carried out at six different oxygen concentrations in an InVivo400 hypoxia workstation (Ruskinn). The enzymatic reactions were carried out at 37°C for 30 min, and the reactions were stopped by adding 100 μL of 1 M KH_2PO_4, pH 5. The amount of ^{14}C-labeled CO_2 generated during reaction was counted using Tri-carb 2900TR scintillation device (Perkin-Elmer). The K_M values were calculated from Michaelis-Menten saturation curves and Lineweaver-Burk plots using Graphpad Prism. The turnover rate of the enzyme (k_{cat}) was calculated using V_{max} values obtained from Michaelis-Menten curves.

Statistical analyses for experimental studies

Prism 9 for macOS was used for all experimental statistical analyses. Most details are provided in figure captions. For identifying the relationship between E-cadherin and vimentin

expression, a non-linear least squares regression with no weighting was performed with sum-of-squares F test comparison to a line with slope of 0 to determine significance. For cell scatter curves, a logistic least squares regression with no weighting was performed with sum-of-squares F test comparison between 21% and 1% O_2 curves to determine significance. For two-way ANOVA, the post hoc test was Tukey's multiple comparisons when considering all conditions and Sidak's multiple comparisons when considering only specific conditions within a larger dataset. For single-cell measurements of protein intensity, a mixed-effects model was used where the number of biological replicates was used as the *n* value and individual cells were treated as repeated measurements within the replicates. This allowed for consideration of all cellular measurements in the analysis, as opposed to just a mean value per replicate, while maintaining the assumption of independence of the biological replicates. For all comparisons, significance was reported based on the *p* value: * $p < 0.05$, ** $p < 0.01$, *** $p < 0.001$, **** $p < 0.0001$.

2.3.3.Supplemental Methods

RNA extraction and RNA-sequencing of patient-derived xenografts

Human pancreatic cancer samples were obtained in accordance with a University of Virginia IRB for Health Sciences Research under the direction of Dr. Todd Bauer. Primary PDX tumors were grown, as previously described (116). Upon harvest, tumors were stored in Qiagen AllProtect at -80°C. Samples were processed using Qiagen Tissuelyser LT along with Qiagen AllPrep DNA/RNA extraction kit. Samples were quantified and quality control was performed before libraries were prepared using polyA capture and cDNA reverse transcription. Libraries were sequenced on Illumina platform PE150 at a read depth of 40 million reads (Novogene Corp., Chula Vista, CA).

Patient-derived xenograft tissue microarray

A tissue microarray was created by the UVA Biorepository & Tissue Research Facility using paraffin-embedded PDX tumors, PDX-derived cell lines, HPAF-II cells, MiaPaca2 cells, and normal pancreas. Antigen retrieval was performed by the UVA Biorepository & Tissue Research Facility, and the slide was stained per the immunohistochemistry protocol described elsewhere in *Methods*. The microarray was imaged using Cytation5 (BioTek) with a 10× objective.

Phospho-kinase and receptor tyrosine kinase arrays

The Proteome Profiler Human Phospho-Kinase Array, which covers 37 phosphorylated kinases and 2 total proteins, was purchased from R&D Systems (ARY003C). Lysates were prepared per manufacturer protocol. The array was developed on film at multiple exposures (30 sec, 1 min, 3 min, 5 min, 7.5 min, 10 min) and imaged using a GS-800 Densitometer (Bio-Rad). The Human Receptor Tyrosine Kinase Phosphorylation Array, which covers 71 targets, was purchased from RayBiotech (AAH-PRTK-G1). Lysates were prepared per manufacturer protocol. After incubation with cell lysates, the array was shipped to RayBiotech for scanning and data extraction.

2.4 RESULTS

EMT is correlated with hypoxia in human PDAC tumors

We first investigated a potential relationship between EMT and hypoxia in human PDAC by analyzing mass spectrometry data from the National Cancer Institute Clinical Proteomic Tumor Analysis Consortium (CPTAC) PDAC Discovery Study (78). When tumors were clustered based on a patient-derived pan-cancer EMT (pcEMT) signature (89) containing 77 genes associated with epithelial and mesenchymal cell states, two groups were identified: mesenchymal-high (M-high) and mesenchymal-low (M-low) **(Figure 2.1A)**. The pcEMT gene signature was used for most analyses because, unlike PDAC subtype signatures (9-11), it includes many of the genes typically measured in EMT studies **(Supp Figure 2.S1A,B)** and is predictive of disease-free survival **(Figure 2.1B)**. Gene set variation analysis [GSVA; (102)] enrichment scores based on the Hallmark Hypoxia set of 200 hypoxia-related genes (91) were higher for M-high tumors than for M-low **(Figure 2.1C)**, suggesting that EMT may occur preferentially in hypoxic tumors. Importantly, only the *COL5A1* gene is shared between the Hallmark Hypoxia and pcEMT signatures **(Supp Figure 2.S1C)**, minimizing concerns about common gene features leading to correlations. The high stromal content of PDAC tumors (42) raises another potential concern with analyses based on bulk tumor measurements, but a relationship between pcEMT mesenchymal protein enrichment and hypoxia was preserved even when controlling for stromal or other tissue content **(Figure 2.1D)**. Repeating the analysis using a 44-gene HIF target gene signature (90), which has no gene overlap with the pcEMT signature, also demonstrated that EMT preferentially occurs in hypoxic tumors **(Supp Figure 2.S2A,B)**.

It is worth noting that the CPTAC PDAC study found hypoxia to be predictive of poor patient survival (78), and we found that the mesenchymal component of the pcEMT signature is highly enriched in the tumors identified as most hypoxic in that publication **(Supp Figure 2.S2C)**, indicating that the positive relationship between hypoxia and EMT in the CPTAC data is robust to

whether tumors are first clustered based on EMT or hypoxia. Despite very little overlap between the pcEMT and PDAC subtype signatures, M-high tumors largely aligned with the Collisson quasi-mesenchymal, Moffitt basal-like, and Bailey squamous subtypes **(Figure 2.1A, Supp Figure 2.S2D)**, which are associated with more aggressive disease. Tumors classified as quasi-mesenchymal (Collisson), basal-like (Moffitt), or squamous (Bailey) were also significantly enriched in both Hallmark Hypoxia and HIF signatures **(Supp Figure 2.S1D, Supp Figure S2E,F)**.

To extend the analysis to transcriptomics, we used RNA-sequencing data from The Cancer Genome Atlas (TCGA) Pancreatic Adenocarcinoma (PAAD) study. Findings similar to those reached in Figure 1 were obtained **(Supp Figure 2.S3A-G)**. Enrichment for hypoxia-related transcripts was predictive of disease-specific survival **(Supp Figure 2.S3H)**, consistent with conclusions reached in the CPTAC PDAC study for proteomics (78).

To confirm the relationship between EMT and hypoxia in ductal cells specifically, we analyzed previously reported single-cell RNA-sequencing (scRNA-seq) data from six human PDAC tumors (88). Ductal cells were projected in a two-dimensional UMAP space (127) using the mesenchymal pcEMT signature genes as features, and consensus clustering (100,101) was performed based on the UMAP features **(Figure 2.1E)**. While the two groups that emerged had markedly different mesenchymal gene expression, they had similar epithelial gene expression **(Figure 2.1F)**, which may result from the focus of this analysis on ductal cells. Sample-wise gene set enrichment scores calculated using pathway and gene set overdispersion analysis (Pagoda2 scores) revealed that that the Hallmark Hypoxia **(Figure 2.1G)** and HIF target **(Supp Figure 2.S4A)** signatures were significantly enriched in ductal cells expressing mesenchymal markers. Ductal cells from a *Kras*$^{+/LSL\text{-}G12D}$*, Trp53*$^{+/LSL\text{-}R172H}$*, Pdx1-Cre* mouse model (88) exhibited the same relationships **(Supp Figure 2.S4B-E)**. Collectively, these analyses suggest that hypoxia and EMT are correlated in PDAC tumors.

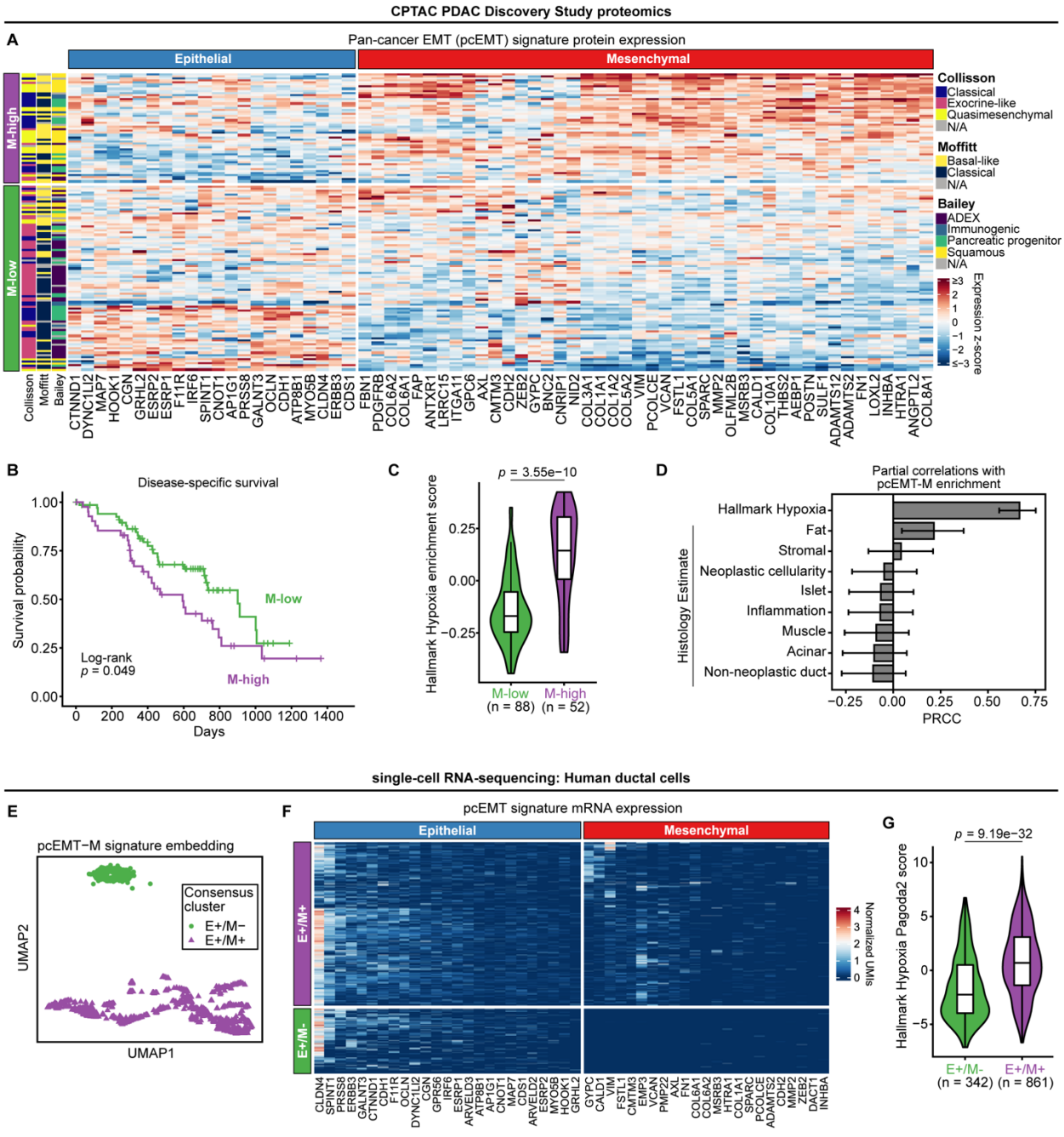

Figure 2.1 EMT and hypoxia marker enrichment are correlated in human PDAC tumors and ductal cells

(A) CPTAC PDAC tumor samples were clustered using non-negative matrix factorization (NMF) of protein expression data for the pan-cancer EMT (pcEMT) signature. Heatmap entries indicate z-scored expression values. The vertical side bar at left (green, purple) indicates the assigned NMF cluster for each tumor. The next three vertical side bars indicate tumor classifications based on the Collisson, Moffit, and Bailey PDAC signatures as reported previously (78). The horizontal side bar (red, blue) indicates the phenotype associated with each protein, as described in publication defining the pcEMT signature (89). (B) Kaplan-Meier analysis was used to determine differences in CPTAC PDAC patient survival when stratifying based

on pcEMT classifications, with a log-rank test performed for statistical analysis. (C) Protein enrichment of the Hallmark Hypoxia signature was calculated using GSVA and compared between M-high and M-low CPTAC PDAC tumors. The Mann-Whitney U test was used to measure significance. (D) Partial rank correlation coefficients (PRCCs) of the indicated variables were calculated with respect to protein enrichment scores for the mesenchymal portion of the pcEMT signature (pcEMT-M). Hallmark Hypoxia enrichment scores were from calculations described in (C). All available histology estimates of specific tissue content were used as provided with the CPTAC data. Error bars denote 95% confidence intervals for the indicated PRCCs. (E) Consensus clustering of scRNA-seq data from human PDAC ductal cells (88) was performed on a 2D UMAP embedding based on the pcEMT-M signature to separate cells into two groups. As explained by results in panel (F), these groups were characterized as epithelial+/mesenchymal- (E+/M-) and epithelial+/mesenchymal+ (E+/M+). (F) Gene expression (normalized UMIs) of the full pcEMT signature in ductal cells is shown with a heatmap, annotated with the cell clusters identified in (E). (G) mRNA enrichment of the Hallmark Hypoxia signature (Pagoda2 scores) was computed and compared between E+/M+ and E+/M- human ductal cells. The Mann-Whitney U test was used to determine statistical significance. (P.J.M.)

To confirm the relationship between EMT and hypoxia in ductal cells specifically, we analyzed previously reported single-cell RNA-sequencing (scRNA-seq) data from six human PDAC tumors (88). Ductal cells were projected in a two-dimensional UMAP space (127) using the mesenchymal pcEMT signature genes as features, and consensus clustering (100,101) was performed based on the UMAP features **(Figure 2.1E)**. While the two groups that emerged had markedly different mesenchymal gene expression, they had similar epithelial gene expression **(Figure 2.1F)**, which may result from the focus of this analysis on ductal cells. Sample-wise gene set enrichment scores calculated using pathway and gene set overdispersion analysis (Pagoda2 scores) revealed that that the Hallmark Hypoxia **(Figure 2.1G)** and HIF target **(Supp Figure 2.S4A)** signatures were significantly enriched in ductal cells expressing mesenchymal markers. Ductal cells from a *Kras*$^{+/LSL\text{-}G12D}$*, Trp53*$^{+/LSL\text{-}R172H}$*, Pdx1-Cre* mouse model (88) exhibited the same relationships **(Supp Figure 2.S4B-E)**. Collectively, these analyses suggest that hypoxia and EMT are correlated in PDAC tumors.

Hypoxia promotes and is correlated with EMT in multiple PDAC model systems

To explore the potential ability of PDAC cells to undergo a cell-autonomous EMT in response to hypoxia, HPAF-II human PDAC cells, which exhibit baseline epithelial characteristics,

were cultured for 120 hr in 21%, 7%, or 1% O_2. These oxygen concentrations were chosen to align with conventional cell culture conditions (21%), median oxygen tension of 6.8% in normal pancreas, and median oxygen tension of 0.4% in pancreas tumors (39,57). E-cadherin loss was robust by 120 hr of hypoxic culture, but hypoxia-inducible factor (HIF)-1α expression peaked at times < 24 hr **(Supp Figure 2.S5A,B)**. At 1% O_2, some HPAF-II cells underwent a clear EMT based on reduced E-cadherin and increased vimentin expression compared to the other O_2 concentrations **(Figure 2.2A)**. Because meaningful differences in EMT markers were not observed between 21% and 7% O_2, all subsequent experiments were performed to compare 21% and 1% O_2. For 1% O_2, a statistically significant inverse relationship between E-cadherin and vimentin expression among cells was determined by linear regression **(Figure 2.2A)**. Because vimentin exhibits a more obvious switch-like expression change in micrographs than does E-cadherin, vimentin was used as the primary mode of assessing EMT throughout this study.

To ensure that changes in E-cadherin and vimentin protein expression observed in hypoxia were accompanied by other changes characteristic of EMT, cellular morphology and EMT-related transcripts were also measured. In a 1% O_2 environment, clusters of GFP-expressing HPAF-II cells exhibited a loss of circularity **(Figure 2.2B)**, consistent with what has been observed for other cell types in response to EMT-inducing growth factors (32). Additionally, in HPAF-II cells cultured in 1% O_2, there was increased expression of the hypoxia transcriptional markers *PGK1* and *SLC2A1* (128), increased expression of the mesenchymal transcripts *VIM*, *SNAI1*, and *TWIST1*, and decreased expression of the epithelial transcript *CDH1* **(Figure 2.2C)**. While there was a decrease in *HIF1A* expression consistent with prior reports (129), HIF-1α protein expression was stabilized by low oxygen **(Supp Figure 2.S5A)**. Together, these results confirm that a *bona fide* EMT occurred in response to hypoxia.

To test for hypoxia-driven EMT in other settings, we first screened cell lines derived from patient-derived xenograft (PDX) tumors. An analysis of RNA-sequencing and tumor grading by a

board-certified pathologist demonstrated that mesenchymal genes were enriched in cells derived from poorly differentiated tumors **(Supp Figure 2.S5C,D)**. Based on screening for baseline epithelial traits using a tissue microarray **(Supp Figure 2.S5E-G)**, we proceeded with six PDX-derived cell lines that readily grew in cell culture and had little or no murine fibroblasts present. Three of these (PDX 366, PDX 395, and PDX 449) exhibited an increase in cell scatter or loss of epithelial morphology in response to 1% O_2 **(Supp Figure 2.S5H)**. PDX 395 cells were selected for further study because they exhibited measurable loss of junctional E-cadherin and increase in vimentin positivity in hypoxic culture.

We also screened for hypoxia-mediated EMT in cells derived from the KPCY (*Kras*$^{LSL\text{-}G12D}$*, p53*$^{loxP/+\ or\ LSL\text{-}R172H}$*, Pdx1-Cre, Rosa26*$^{LSL\text{-}YFP}$) mouse model of PDAC. Six cell lines were screened based on their baseline epithelial phenotype. In pilot screening studies, every cell line exhibited increased vimentin positivity in 1% O_2 **(Supp Figure 2.S6A)**. 7160c2 was among the cell lines that also had an obvious morphology change in 1% O_2, and it was used for further studies. These results suggest that hypoxia-mediated EMT occurs in a variety of PDAC cell settings but that not all cell contexts are primed for this phenomenon.

To investigate a correlation between hypoxia and EMT *in vivo*, we first confirmed the presence of hypoxic tumor regions in a mouse model of PDAC using pimonidazole (Hypoxyprobe), a reagent that binds to peptide thiols at low oxygen concentrations. The growth time needed to detect Hypoxyprobe (HYP)-positive cells in implantable tumor models was based on a pilot study that showed abundant staining by six weeks **(Supp Figure 2.S6B)**. Compared to normal mouse pancreas, a PDX tumor exhibited low CD31 and elevated Hypoxyprobe staining, indicating relatively poor vascularization **(Figure 2.2D)**. Higher magnification images revealed that CD31-positive structures consistent with capillary beds were non-overlapping with HYP-positive cells **(Figure 2.2E)**.

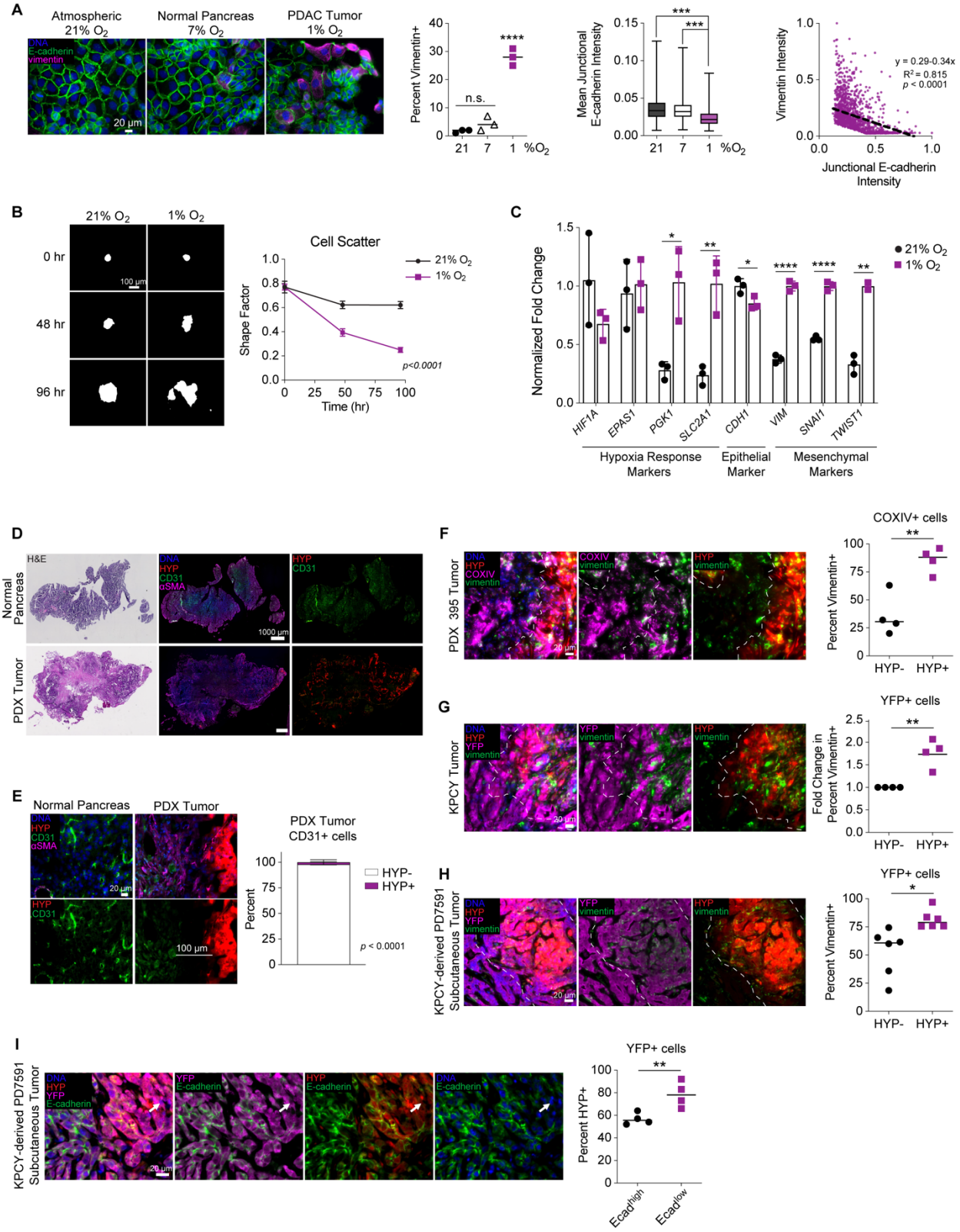

Figure 2.2 Hypoxia drives a *bona fide* EMT in PDAC cells and correlates with EMT in diverse mouse models of PDAC

(A) HPAF-II cells were cultured under atmospheric (21% O_2), normal pancreas (7% O_2), and PDAC tumor (1% O_2) conditions for 120 hr. Immunofluorescence microscopy was performed for the indicated proteins, $n = 3$. For percent vimentin+, a one-way ANOVA with Tukey's multiple comparison test comparing all conditions was performed. For mean E-cadherin intensity, a mixed-effects analysis with Tukey's multiple comparison test was performed. To compare E-cadherin and vimentin intensity per cell, normalized signal from HPAF-II cells cultured in 1% O_2 was plotted and fit to a nonlinear regression, as described in *Methods*. (B) GFP-expressing HPAF-II cells were cultured in 21% or 1% O_2 for 96 hr. Fluorescence microscopy for GFP was performed and the shape factor was calculated per cluster. Data are represented as mean ± s.e.m. $p < 0.0001$ for nonlinear regression comparing slopes, as described in *Methods*. (C) RNA was extracted from HPAF-II cells cultured for 120 hr in 21% and 1% O_2, and qRT-PCR was performed for hypoxia response markers (*HIF1A, EPAS1, PGK1,* and *SLC2A1*) and EMT markers (*CDH1, VIM, SNAI1,* and *TWIST1*). *CASC3* was used as a control gene for normalization. $n = 3$, with t test per transcript. (D) H&E and fluorescent immunohistochemistry for Hypoxyprobe (HYP) and CD31 was performed for murine normal pancreas and PDX tumors. Representative image shown for $n = 3$. (E) Sections of normal mouse pancreas or PDX 395 tumors were stained for HYP and CD31. Image analysis was performed for PDX 395 tumors and quantified for the percent CD31+ cells that were HYP- or HYP+. $n = 3$, with t test. (F) PDX 395 tumors were sectioned and stained to quantify COXIV+/vimentin+ cells that were HYP- or HYP+. $n = 4$, with t test. White dotted line separates regions enriched for HYP+ or HYP- cells. (G) Sections of KPCY tumors were stained with the indicated antibodies, and image analysis was performed to quantify YFP+/vimentin+ cells that were HYP- or HYP+. Data are represented as fold change due to variability across spontaneous genetic mouse model. $n = 4$, with t test. (H) Subcutaneous tumors generated from KPCY-derived PD7591 cells were sectioned and stained with the indicated antibodies. Image analysis was performed to quantify YFP+/vimentin+ cells that were HYP- or HYP+. $n = 6$, with t test. (I) Sections of PD7591 subcutaneous tumors were stained for with the indicated antibodies, and image analysis was performed to quantify YFP+/HYP+ cells that were $Ecad^{high}$ or $Ecad^{low}$. $n = 4$, with t test. * $p < 0.05$, ** $p < 0.01$, *** $p < 0.001$, **** $p < 0.0001$

To assess the relationship between hypoxia and EMT, we utilized three mouse models: orthotopic PDX tumors, KPCY autochthonous tumors, and subcutaneous tumors formed from KPCY-derived cell lines. Antibodies against human COXIV or YFP were used to identify human cells in PDX tumors or epithelial-derived cells in KPCY and subcutaneous tumors, respectively **(Figure 2.2F-I, Supp Figure 2.S6C-H)**. Based on prior work showing that PDX 395 tumors are devoid of human fibroblasts (130), COXIV+ cells were identified as human ductal tumor cells. In PDX tumors, COXIV+/HYP+ cells were primarily vimentin+ **(Figure 2.2F)**. Similarly, in KPCY and subcutaneous tumors, more YFP+/HYP+ cells were vimentin+ than were YFP+/HYP- **(Figure 2.2G,H, Supp Figure 2.S6G)**. Further, in KPCY subcutaneous tumors, YFP+/HYP+ cells were preferentially low in E-cadherin expression **(Figure 2.2I, Supp Figure 2.S6H)**.

Hypoxia-driven EMT can be as complete as growth factor-driven EMT and is more durable

Growth factors are perhaps the most well-studied drivers of EMT. To compare that mode of EMT induction against hypoxia, we combined TGFβ and HGF because both potently promote EMT. In HPAF-II cells, flow cytometry revealed that growth factors drove more than twice as many cells to become mesenchymal than did hypoxia, based on vimentin staining **(Figure 2.3A)**. E-cadherin expression was reduced by both growth factors and hypoxia **(Supp Figure 2.S7A)**. By immunofluorescence microscopy, the trend of more potent EMT induction by growth factors was again observed in HPAF-II cells, but hypoxia and growth factors led to comparable EMT effects in PDX- and KPCY-derived cells **(Figure 2.3B)**. Thus, in some cell settings, hypoxia may drive EMT as homogeneously among cells as growth factors do.

To explore the time scale of mesenchymal phenotype persistence for different methods of EMT induction, HPAF-II cells that had been treated with growth factors or cultured in 1% O_2 were replated in complete medium (without added growth factors) and cultured in 21% O_2. Interestingly, the rate of loss of vimentin+ cells was smaller for cells that had been cultured in hypoxia than those that had been treated with growth factors **(Figure 2.3C)**. Similar trends were observed in KPCY- and PDX-derived cell lines **(Supp Figure 2.S7B,C)**. In KPCY and PDX cells, however, replating after removal of the EMT-inducing condition caused a temporary spike in vimentin positivity. Despite this artifact, it is apparent that hypoxia resulted in more persistent vimentin expression. In PDX-derived 395 cells, there was a more modest decrease in vimentin positivity than in HPAF-II and KPCY 7160c2 cells, which could potentially be attributed to differential baseline vimentin expression.

The preferential maintenance of vimentin expression among cells that experienced low oxygen suggests that hypoxia-induced EMT may be more heritable than EMT driven by growth factors. That is, because the time scale for HPAF-II cell division [~36-42 hr, based on our observations and prior work (131)] is small compared to the time scale over which the fraction of

mesenchymal cells can be maintained (at least 120 hr), the data in Figure 2.3C suggest that vimentin-positive cells must give rise to other vimentin-positive cells for the hypoxic, but not the growth factor-treated, condition. To test this, we quantified nuclei with a morphology indicative of mitosis 120 hr after relief of EMT-inducing conditions. More vimentin-positive cells that appeared to be actively dividing were found among those previously treated with hypoxia than those treated with growth factors **(Figure 2.3D)**. The overall trend in preferential vimentin persistence after hypoxia was also observed five weeks after treatment-withdrawal **(Supp Figure 2.S7D)**.

To explore the implications of durable hypoxia-mediated EMT in tumors, HPAF-II cells were engineered with a HIF-regulated fate-mapping system that stably converts from DsRed to GFP expression after sufficient hypoxia exposure (125). Validation of the clonally selected transductant used in these studies is described in **Supp Figure 2.S7E**,**F**. As in other PDAC models, orthotopic tumors formed from the HPAF-II clone exhibited more vimentin+/HYP+ tumor cells than vimentin+/HYP- cells **(Supp Figure 2.S7G)**. Furthermore, there were equivalent numbers of GFP+/vimentin+ cells that were HYP+ and HYP- **(Figure 2.3E)**. One possible explanation for this observation is that cells can maintain a hypoxia-driven mesenchymal state in a tumor even outside a region of low oxygen tension. Five-color confocal imaging revealed a lack of difference in vimentin positivity for DsRed+ and GFP+ cells **(Supp Figure 2.S7G)**, suggesting that microenvironmental factors other than hypoxia, such as growth factors, may also be substantial drivers of EMT in PDAC tumors. To test the mesenchymal durability of GFP+ cells, pieces of explanted orthotopic tumors were dissociated and flow-sorted into DsRed+, GFP+, and DsRed+/GFP+ populations, which were cultured in 21% O_2. Note that double-positive cells arise due to slow DsRed turnover and that there were too few collected cells that were only GFP+ to analyze. 12 days after tumor dissociation, more DsRed+/GFP+ cells were vimentin+ than were DsRed+ cells **(Figure 2.3F)**. Combined with the results of Figure 2.3C, this suggests that hypoxia-mediated EMT contributed substantially to vimentin expression in DsRed+/GFP+ cells.

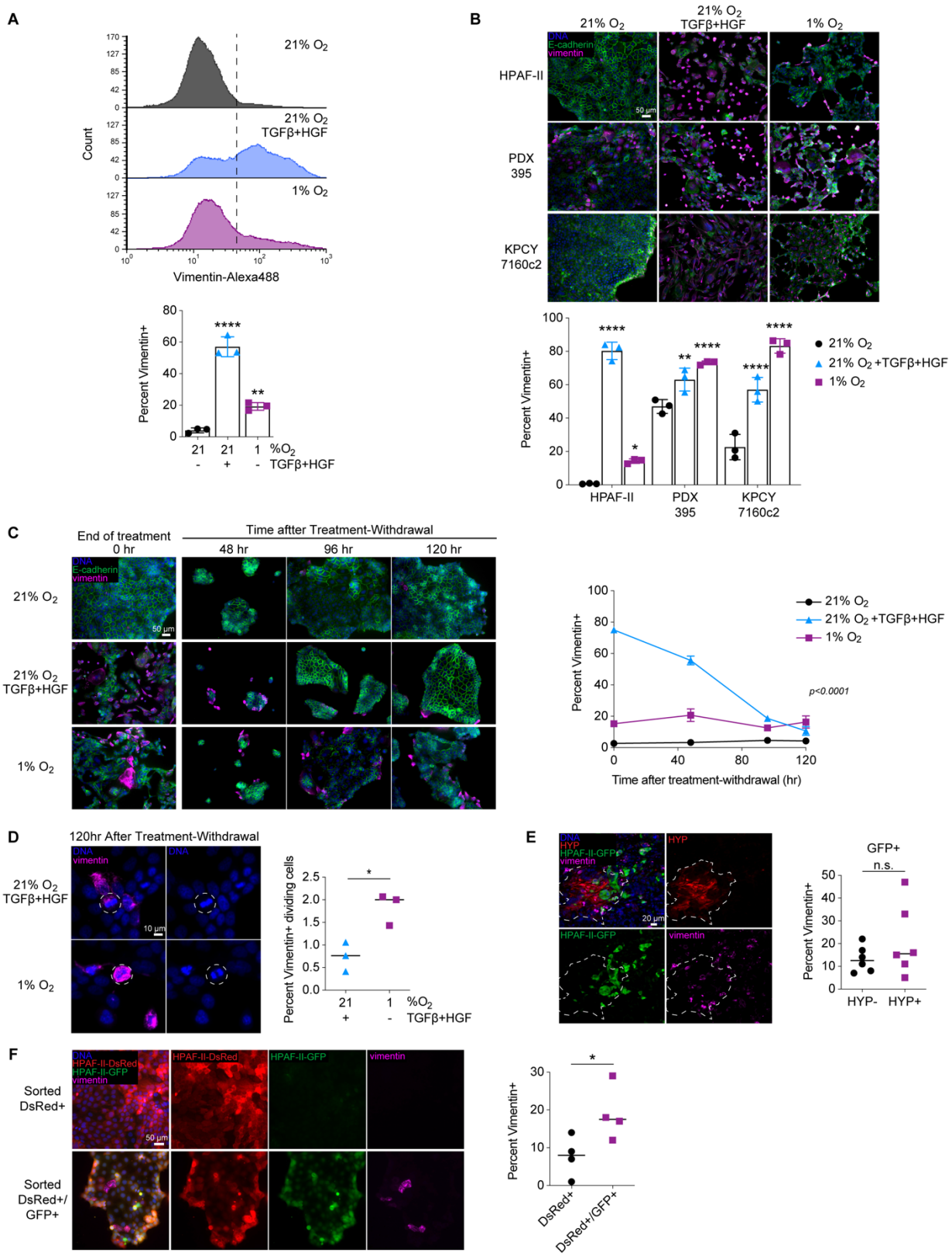

Figure 2.3 EMT in response to hypoxia can occur heterogeneously and is more durable than EMT in response to growth factors

(A) HPAF-II cells were cultured in 21% O_2 with or without 10 ng/mL TGFβ and 50 ng/mL HGF or cultured in 1% O_2 for 120 hr. Cells were then fixed and stained for vimentin, and flow cytometry was performed. Representative data are shown for a single biological replicate, with a summary of data for $n = 3$ in the bar plot. One-way ANOVA with Tukey's multiple comparisons test with comparison to 21% O_2. **(B)** PDAC cells from three different backgrounds were cultured as in (A). Immunofluorescence microscopy was performed for the indicated proteins. $n = 3$, with two-way ANOVA and Tukey's multiple comparisons test, comparisons shown within each cell line to the control 21% O_2 condition. **(C)** HPAF-II cells were first cultured as described in (A). At the end of treatment, cells were re-plated on coverslips and cultured in 21% O_2 without growth factors for up to 120 hr. At the indicated times after re-plating, cells were fixed and immunofluorescence microscopy was performed for the indicated proteins, $n = 3$. Data are represented as mean ± s.e.m. $p < 0.0001$ for nonlinear regression comparing slopes. **(D)** 120 hr after treatment withdrawal from either 10 ng/mL TGFβ + 50 ng/mL HGF or culture in 1% O_2, HPAF-II cells were stained for DNA and vimentin to quantify actively dividing, vimentin+ cells (examples shown encircled by dotted lines). $n = 3$, with t test. **(E)** Orthotopic tumors generated from HPAF-II hypoxia fate-mapping cells (GFP = hypoxic response) were sectioned and stained with the indicated antibodies. Image analysis was performed to quantify the fraction of GFP+ cells that were vimentin+ and Hypoxyprobe-negative (HYP-) or positive (HYP+). $n = 6$, with t test. **(F)** Pieces of explanted tumors described in (E) were disaggregated and flow-sorted based on DsRed and GFP fluorescence. The indicated populations of cells were cultured in 21% O_2 for 12 days after dissociation, and then fixed and stained with the indicated antibodies. $n = 4$, with t test. * $p < 0.05$, ** $p < 0.01$, **** $p < 0.0001$

MAPK and SFK signaling promote hypoxia-mediated EMT and are activated by impaired phosphatase expression

To identify signaling mechanisms that promote EMT in hypoxia, we first analyzed publicly available human PDAC patient data. From the CPTAC PDAC Discovery Study proteomics data (78), we extracted the reported overall phosphorylation scores for all human kinases and calculated Spearman rank correlation coefficients with Hallmark Hypoxia enrichment scores. We then pared the list of kinases to retain only those whose phosphorylation was positively and significantly ($p < 0.05$) correlated with Hallmark Hypoxia protein enrichment for use in an overrepresentation analysis (hypergeometric test) with the Kyoto Encyclopedia of Genes and Genomes (KEGG) signaling pathways. The KEGG MAPK signaling pathway gene set had the largest number and highest fraction of its phosphokinases present in this list of overrepresented pathways **(Figure 2.4A, Supp Figure 2.S1E)**. The KEGG MAPK gene set contains nodes involved in the ERK1/2, JNK, p38, and ERK5 pathways. Thus, this analysis suggests that signaling through one or more of those pathways may regulate PDAC response to hypoxia.

To extend this analysis to the scRNA-seq data (88), we developed a linear model of the relationship between signaling ontologies and Hallmark Hypoxia gene set enrichment in human PDAC ductal cells. We first calculated enrichment scores for the KEGG signaling pathways and Hallmark Hypoxia gene set using pathway and gene set overdispersion analysis (Pagoda2). We then trained a least absolute shrinkage and selection operator (LASSO) regression model to perform automatic variable selection of the KEGG signaling pathway gene sets for predicting Hallmark Hypoxia enrichment, followed by training an ordinary least squares regression model and performing additional variable selection via minimization of the Akaike information criterion (AIC). Of the 30 KEGG signaling pathway gene sets that were sufficiently overdispersed to obtain Pagoda2 scores, 19 were retained by the LASSO model, and 16 of these were retained after AIC selection. The final linear model was statistically significant and identified the KEGG MAPK gene set as most predictive of Hallmark Hypoxia enrichment in human ductal cells **(Figure 2.4B)**. An identical analysis performed using the published mouse ductal cell scRNA-seq data (88) identified HIF-1 and MAPK signatures as most predictive of Hallmark Hypoxia enrichment **(Supp Figure 2.S8A)**. We will return to the role of HIFs but note for now the consistent role of MAPK signaling implied across our analyses.

Based on the computational model results, we tested inhibitors of the p38, JNK, and ERK1/2 MAPK pathways for their ability to antagonize hypoxia-mediated EMT. MEK and JNK inhibitors suppressed vimentin expression and promoted E-cadherin expression in hypoxic culture **(Figure 2.4C, Supp Figure 2.S8B,C)**. Inhibitor concentrations were selected for their ability to impact EMT without causing cell death. Surprisingly, p38 inhibition promoted vimentin expression in both 21% and 1% O_2, which could indicate a role for p38 in antagonizing EMT, as has been reported (132,133). Combined inhibition of MEK and JNK had an additive effect, suggesting that both pathways may participate in hypoxia-mediated EMT. An additive effect was

also seen for EMT protein markers in PDX 395 cells **(Figure 2.4D)** and EMT transcript markers in HPAF-II cells **(Supp Figure 2.S8D)**.

Given the role of MAPK signaling in growth factor-driven EMT (32,134,135), we compared MAPK activation in growth factor- and hypoxia-driven EMT. For growth factors, pc-Jun, c-Jun, and pERK abundance increased acutely 24 hr after treatment and returned to untreated levels by 120 hr. In hypoxic culture, elevated c-Jun expression and ERK phosphorylation persisted at 120 hr, with a concomitant reduction in E-cadherin expression **(Figure 2.4E, Supp Figure 2.S8E).** Because changes in total c-Jun expression were more robustly detected than changes in its phosphorylation, c-Jun expression was typically used throughout this study as a proxy for JNK activity. This choice is supported by prior work showing that JNK activity promotes c-Jun expression (136-138) and by our observation that c-Jun expression was suppressed by JNK inhibition **(Supp Figure 2.S8F)**. siRNA-mediated knockdown of ERK1/2 and c-Jun, alone or in combination, also impeded EMT in hypoxic culture **(Supp Figure 2.S8G,H)**. Note that ERK1/2 knockdown did not suppress c-Jun expression **(Supp Figure 2.S8G)**, further supporting our use of c-Jun expression as a specific readout for JNK signaling.

To identify the driver of MAPK signaling in hypoxia, a human phospho-kinase array (37 phosphorylated and two total protein targets) and phosphorylated receptor tyrosine kinase array (71 targets) were used **(Supp Figure 2.S9A,B)**. Both arrays detected increased phosphorylation of Src family kinases (SFKs). Given that SFKs can participate in MAPK activation, we tested the relationship between SFKs and MAPKs in hypoxia and found that SFK inhibition antagonized nuclear c-Jun accumulation and ERK phosphorylation **(Figure 2.4F,G)**. SFK inhibition also antagonized hypoxia-driven EMT, halving the number of vimentin-positive cells and promoting a more clustered cell configuration **(Figure 2.4H)**. We also screened for hypoxia-induced cytokines at the protein (Luminex) and transcript (qRT-PCR) levels, but these measurements did not identify any upregulated cytokines that regulate EMT in HPAF-II cells (not shown).

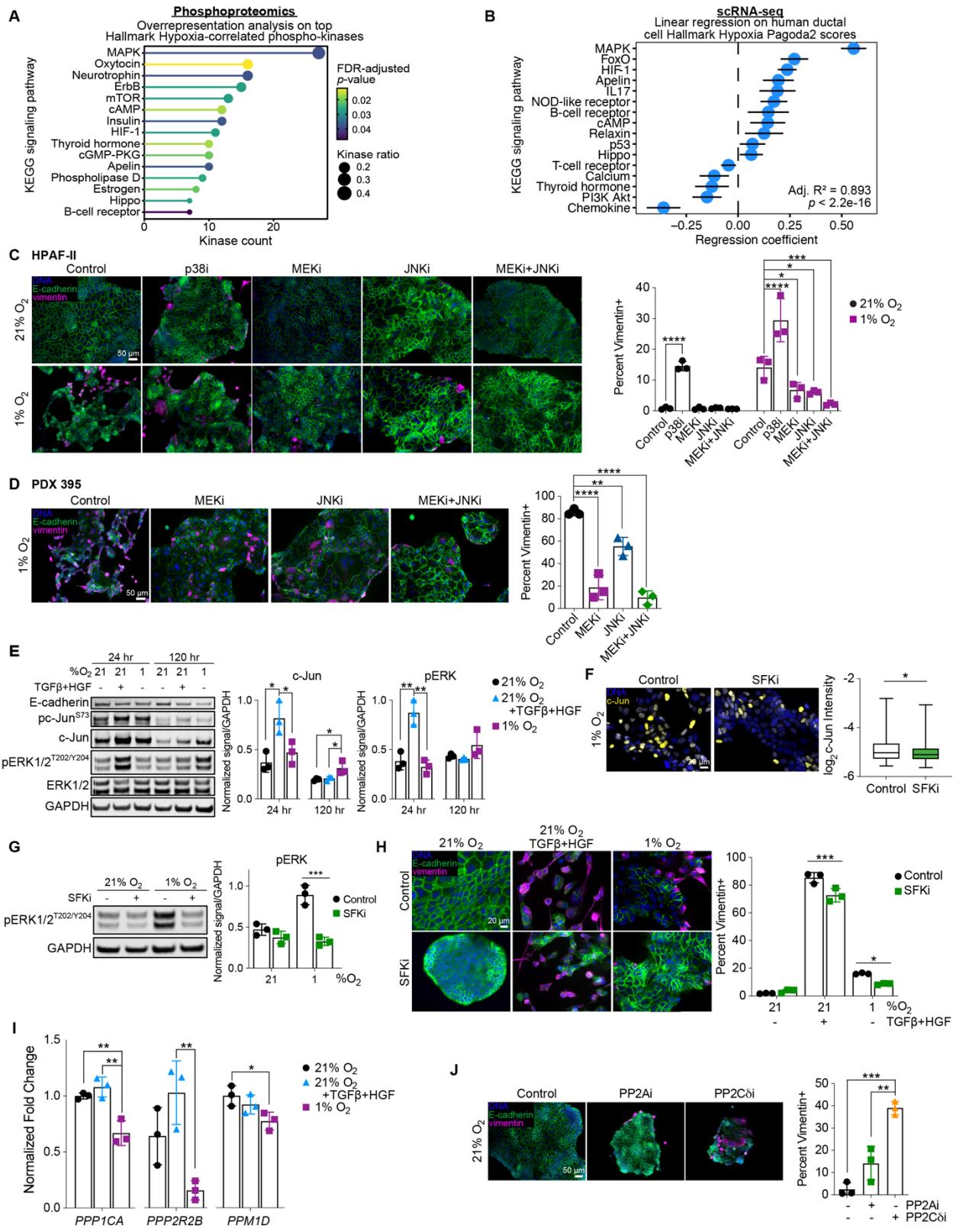

Figure 2.4 Hypoxia promotes EMT through MAPK signaling and suppression of protein phosphatase expression

(A) Overrepresentation analysis for the indicated KEGG signaling pathways was performed using the list of kinases whose overall phosphorylation was significantly and positively correlated with Hallmark Hypoxia protein enrichment in the CPTAC PDAC Discovery Study (78). The 15 overrepresented KEGG signaling pathway gene sets (out of 46) based on kinase ratio are shown (FDR-adjusted $p < 0.05$). Kinase count indicates the number of kinases appearing in each gene set with significant and positive correlations with Hallmark Hypoxia enrichment. Kinase ratio indicates the fraction of kinases in each gene set that are significantly and positively correlated with Hallmark Hypoxia enrichment. (P.J.M.) **(B)** Coefficients are shown for the regularized linear regression model predicting Hallmark Hypoxia Pagoda2 scores based on KEGG signaling pathway Pagoda2 scores for scRNA-seq data (88). Error bars denote 95% confidence intervals. (P.J.M.) **(C)** HPAF-II cells were cultured for 120 hr in 21% O_2 or 1% O_2 with 1 μM CI-1040 (MEKi), 10 μM SP600125 (JNKi), 10 μM SB203580 (p38i), or DMSO. $n = 3$, two-way ANOVA with Sidak's multiple comparisons test. **(D)** PDX 395-derived cells were cultured in 1% O_2 with 1 μM CI-1040 (MEKi), 10 μM SP600125 (JNKi), a combination, or DMSO for 120 hr, with inhibitors replenished every 48 hr. Cells were then fixed and stained with antibodies for the indicated proteins. Immunofluorescence microscopy and quantitative image analysis was performed. $n = 3$, one-way ANOVA with Dunnett's multiple comparison test against the untreated (control) condition. **(E)** HPAF-II cells were cultured in 21% O_2 with or without 10 ng/mL TGFβ + 50 ng/mL HGF, or in 1% O_2, and lysed 24 and 120 hr after treatment. Immunoblotting was performed for the indicated proteins. $n = 3$, one-way ANOVA with Tukey's multiple comparisons test at each time point. **(F)** HPAF-II cells were cultured for 120 hr in 21% O_2 or 1% O_2 with 10 μM PP2 (Src family kinase inhibitor, SFKi) or DMSO, and immunofluorescence microscopy was performed for nuclear c-Jun. $n = 3$, mixed-effects analysis with Tukey's multiple comparisons test. **(G)** HPAF-II cells were treated as in (F), and lysates were analyzed by immunoblotting for the indicated proteins. $n = 3$**,** two-way ANOVA with Sidak's multiple comparison test. **(H)** HPAF-II cells were cultured in 21% O_2 with or without 10 ng/mL TGFβ and 50 ng/mL HGF or in 1% O_2 for 120 hr. Cells were pre-treated with 10 μM PP2 or DMSO 24 hr prior to hypoxia or growth factor treatment. $n = 3$, two-way ANOVA with Sidak's multiple comparison test. **(I)** qRT-PCR was performed for PP1A, PP2A, and PP2C subunit transcripts on RNA isolated from HPAF-II cells treated as described in (D) for 120 hr. *CASC3* was used as a control gene for normalization. $n = 3$, one-way ANOVA with Tukey's multiple comparisons test for each subunit independently. **(J)** HPAF-II cells were cultured for 120 hr in 21% O_2 with 5 μM LB100 (PP2Ai), 1.5 μM sanguinarine chloride (PP2Cδi), or DMSO. $n = 3$, one-way ANOVA with Tukey's multiple comparisons test. * $p < 0.05$, ** $p < 0.01$, *** $p < 0.001$, **** $p < 0.0001$

Lacking leads for potential cytokine inducers of SFK activity, we hypothesized that phosphatase expression may be suppressed in hypoxia. We specifically considered protein phosphatase 2 (PP2A), a serine/threonine phosphatase holoenzyme with catalytic, regulatory, and scaffolding subunits (139), due to its regulation of MAPK and SFK signaling (140,141). To test this hypothesis, we first analyzed the PDAC tumor scRNA-seq data (88) and found that transcripts for PP2A, as well as PP2C and PP1A, were negatively correlated with the HIF gene signature **(Supp Figure 2.S10)**. This finding was confirmed in HPAF-II cells, where transcripts for multiple protein phosphatase subunits (catalytic, regulatory, and scaffolding) were decreased by hypoxia but not by growth factors **(Figure 2.4I).** Furthermore, inhibition of PP2A or PP2Cδ at 21% O_2 promoted vimentin expression **(Figure 2.4J)** and the accumulation of c-Jun and ERK in the

nucleus **(Supp Figure 2.S9C-E)** in HPAF-II cells. Thus, suppressed expression of MAPK-regulating serine/threonine phosphatases may be a hypoxia-specific mechanism for EMT.

To further probe the relevance of MAPK signaling for hypoxia-mediated EMT, we returned to the mouse models used in Figure 2.2. In KPCY and subcutaneous tumors, nuclear c-Jun abundance was elevated in hypoxic YFP+ cells **(Figure 2.5A,B)**. In PDX tumors, c-Jun was also more abundant in hypoxic cells, and nuclear c-Jun was found preferentially in vimentin-positive cells **(Figure 2.5C)**. PDX tumors also exhibited elevated pERK staining in vimentin-positive cells **(Figure 2.5D)**. These results further support a role for JNK and ERK signaling in hypoxia-mediated EMT in PDAC. Interestingly, hypoxia-mediated EMT, while durable, is reversible via MEK and JNK inhibition in cell culture experiments **(Figure 2.5E, Supp Figure 2.S9F)**.

To investigate the ability of MAPK antagonism to abrogate EMT *in vivo*, MEK and JNK inhibitors were tested in mice bearing orthotopic PDX 395 tumors. For both HYP+ and HYP- cells, MEK or JNK inhibition reduced the fraction of cells that were vimentin+, but this effect was only significant when MEK and JNK inhibitors were combined **(Figure 2.5F)**. EMT inhibition was accompanied by anticipated reductions in ERK phosphorylation and c-Jun nuclear accumulation **(Supp Figure 2.S9G,H)**. These results confirm that ERK and JNK cooperate to drive EMT in both hypoxic and normoxic tumor cells and demonstrate that small-molecule inhibitors may be able to interrupt and reverse this process *in vivo*, even in areas with limited vascularization.

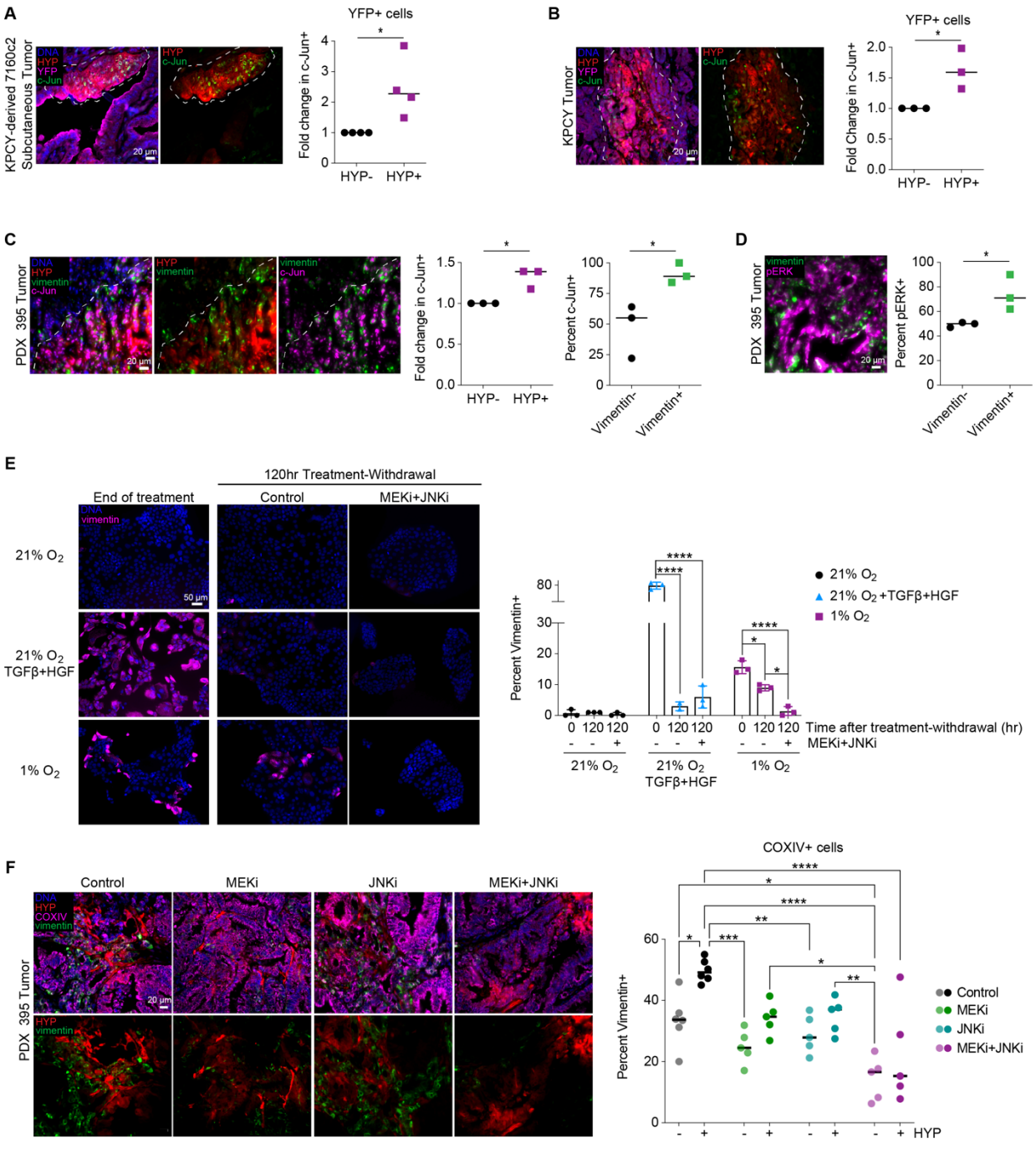

Figure 2.5 Hypoxic PDAC tumor tissue is enriched for markers of MAPK signaling, and MAPK inhibition prevents EMT in hypoxic tumor cells

(A) Sections of KPCY tumors were stained for the indicated proteins, and image analysis was performed to quantify YFP+/c-Jun+ cells that were positive or negative for Hypoxyprobe (HYP). Data are reported as fold change in the percent c-Jun+ cells from HYP- to HYP+. *n* = 3, with t test. White dotted line separates regions enriched for HYP+ or HYP- cells. **(B)** Sections of subcutaneous tumors formed from KPCY-derived 7160c2 cells were stained for the indicated proteins, and image analysis was performed as described in

(A). *n* = 4, with t test. **(C)** Sections of PDX 395 orthotopic tumors were stained for the indicated proteins, and image analysis was performed to quantify c-Jun+ cells that were HYP- or HYP+ or vimentin- or vimentin+. c-Jun+ data are reported as fold change in percent c-Jun+ cells that were HYP- or HYP+. *n* = 3, with t test. **(D)** Sections of PDX 395 tumors were stained to probe for correlations in pERK and vimentin, and image analysis was performed to quantify the percent of vimentin- or vimentin+ cells that were pERK+ cells. *n* = 3, with t test. **(E)** HPAF-II cells were cultured in 21% O_2 with or without 10 ng/mL TGFβ + 50 ng/mL HGF or in 1% O_2 for 120 hr. Cells were then re-plated and cultured for another 120 hr at 21% O_2 without exogenous growth factors and with 1 μM CI-1040 (MEKi) and 10 μM SP600125 (JNKi) or DMSO. At the indicated times, cells were fixed and stained for vimentin. Immunofluorescence microscopy with quantitative image analysis for the percentage of vimentin+ cells was performed. *n* = 3, two-way ANOVA with Tukey's multiple comparisons test. **(F)** Mice bearing orthotopic PDX 395 tumors were treated for nine days with selumetinib (MEKi), SP600125 (JNKi), selumetinib+SP600125, or vehicle control. Tumor sections were stained for COXIV, HYP, and vimentin, and quantitative image analysis was performed. *n* = 5 - 6, two-way ANOVA with Tukey's multiple comparisons test. * $p < 0.05$, ** $p < 0.01$, *** $p < 0.001$, **** $p < 0.0001$

HIFs play a supporting role in hypoxia-driven EMT

To probe the role of HIFs in hypoxia-mediated EMT, we first utilized RNA interference in HPAF-II cells. Transient knockdown of *HIF1A* (HIF-1α) and/or *EPAS1* (HIF-2α) antagonized vimentin expression in hypoxia **(Figure 2.6A, Supp Figure 2.S11A)**. At the transcriptional level, however, there was no statistically significant effect of HIF knockdown on *VIM*, *SNAI1*, or *CDH1* at 1% O_2 **(Figure 2.6B)**. Vimentin can be post-translationally modified (142) which could account for the discrepancy in protein and transcript changes, that we also saw with JNK inhibition alone **(Supp Figure 2.S8D)**. Further, with stable knockdown of both transcripts, there was not a significant decrease in vimentin positivity **(Figure 2.6C, Supp Figure 2.S11B)**. To test the role of HIF expression on EMT *in vivo*, we analyzed tumors from a pancreas-specific *Kras*-mutant *Hif1a*-knockout (*Kras*^{G12}*Hif1a*^{KO}) mouse (59). Focusing on cells that could be definitively determined as epithelial-derived through E-cadherin staining, we observed comparable amounts of E-cadherin+/vimentin- cells and an insignificant decrease in E-cadherin+/vimentin+ cells in *Hif1a*^{KO} versus *Hif1a*-replete tumors **(Supp Figure 2.S11C-E)**. *Hif1a*^{KO} tumors did display more E-cadherin-/vimentin+ cells, but some of those are likely to be fibroblasts. The ambiguous effects of *Hif1a* knockout on EMT may be consistent with prior reports that pancreas-specific *Hif1a* depletion in *Kras*$^{LSL\text{-}G12D/+}$/*Trp53*$^{LSL\text{-}R172H/+}$/*Pdx1-Cre* mice actually resulted in more advanced neoplasia and increased metastasis (143).

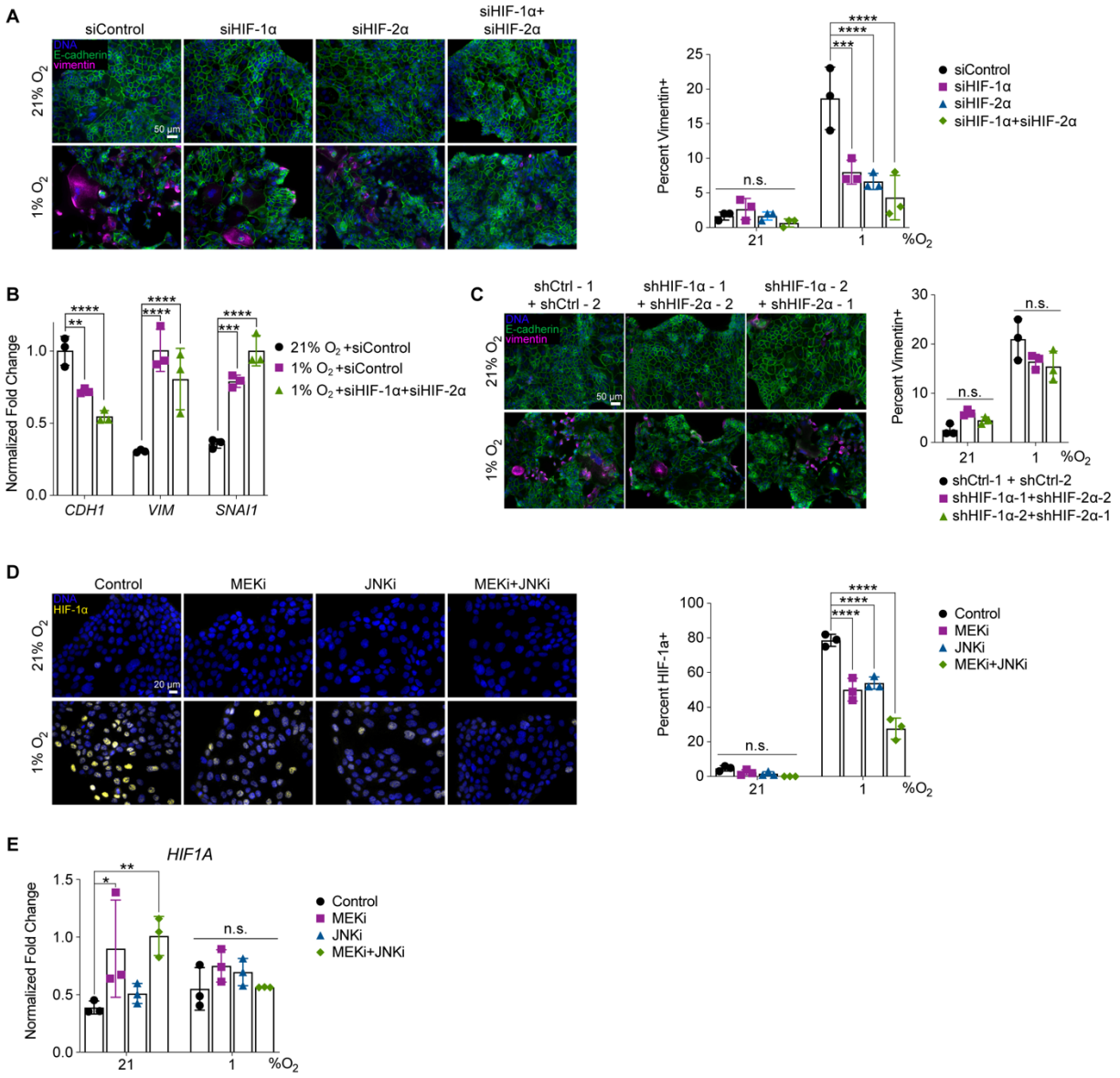

Figure 2.6 HIF expression plays a supporting role in hypoxia-mediated EMT and is regulated by MAPK signaling

(A,B) HPAF-II cells were transfected with HIF-1α or HIF-2α siRNA, a combination of the two, or control siRNA. 24 hr later, cells were switched to a 1% O_2 environment or maintained in 21% O_2 and allowed to grow for 120 hr. **(A)** Immunofluorescence microscopy for the indicated targets was performed, with quantification of vimentin+ cells. *n* = 3, two-way ANOVA with Tukey's multiple comparisons test, comparisons made against the control condition for 21% or 1% O_2. **(B)** qRT-PCR was performed for *CDH1, VIM,* and *SNAI1*. *CASC3* was used as a control gene for normalization. *n* = 3, two-way ANOVA with Tukey's multiple comparisons test. **(C)** Immunofluorescence microscopy was performed on HPAF-II cells engineered with stable expression of HIF-1α and HIF-2α shRNAs or control shRNAs. Cells were cultured in 21% or 1% O_2 for 120 hr prior to fixing and staining with antibodies against the indicated proteins. *n* = 3, two-way ANOVA with Tukey's multiple comparisons test. **(D)** HPAF-II cells were pre-treated with 1 μM CI-1040 (MEKi), 10 μM SP600125 (JNKi), a combination, or DMSO for 24 hr, then cultured in 21 or 1% O_2 for 4 hr. *n* = 3, two-way ANOVA with Tukey's multiple comparisons test, comparisons against control condition

for 21% or 1% O_2. **(E)** qRT-PCR for *HIF1A* was performed using RNA isolated from HPAF-II cells cultured for 120 hr in 21% O_2 or 1% O_2 with 1 μM CI-1040 (MEKi),10 μM SP600125 (JNKi), a combination, or DMSO. *CASC3* was used as a control gene for normalization. n = 3, two-way ANOVA with Tukey's multiple comparisons test, comparisons against the control condition within either 21% or 1% O_2. * $p < 0.05$, ** $p < 0.01$, *** $p < 0.001$, **** $p < 0.0001$

Because MAPKs regulate HIF expression in some settings (144,145), we tested the effects of MEK and JNK inhibitors on HIF expression. Each inhibitor antagonized HIF-1α accumulation in hypoxia, and the combination of inhibitors was even more effective **(Figure 2.6D)**. However, *HIF1A* transcripts were unaffected by the inhibitors **(Figure 2.6E)**. Therefore, in addition to their HIF-independent roles in EMT, ERK and JNK stabilize HIF-1α post-translationally in hypoxia. Collectively, our data suggest that HIFs may play a supporting, but not indispensable, role in EMT.

Hypoxia-driven EMT depends on histone methylation

Due to the durable and heritable nature of hypoxia-driven EMT, we hypothesized that epigenetic modifications could be involved. Based on prior work that found that TGFβ-mediated EMT depends on dimethylation of lysine 36 on histone H3 (H3K36me2) and that this epigenetic mark promotes *Zeb1* and *Snai1* expression (34), we probed for changes in H3K36me2 in hypoxia. H3K36me2 abundance was increased in HPAF-II cells treated with growth factors or cultured in 1% O_2 **(Figure 2.7A)**. Furthermore, H3K36me2 persisted longer in cells exposed to hypoxia than in those treated with growth factors **(Supp Figure 2.S12A)**, mirroring the persistence of mesenchymal traits described previously.

To understand the basis for altered histone methylation in hypoxia, we investigated the activity and expression of the methyltransferase NSD2 and the lysine demethylase KDM2A, which are critical in TGFβ-mediated EMT (34). The activities of certain lysine demethylases in the Jumonji C (JmjC) domain-containing family, including KDM5A and KDM6A, are sensitive to (patho)physiologically relevant changes in oxygen tension (63,64). Therefore, we characterized

the oxygen-dependent activity of FLAG-tagged and purified KDM2A **(Supp Figure 2.S12B-G)**. Measurements confirmed an interaction strength between KDM2A and H3K36me2 consistent with other pairs of histones and demethylases represented by an H3K36me2 K_M = 108 ± 12 μM and revealed an O_2 K_M = 57 ± 17 μM **(Figure 2.7B,C, Supp Figure 2.S12H)**. While this O_2 K_M is several-fold lower than those reported for KDM5A and KDM6A (63,64), it clearly falls between the oxygen concentrations observed in normal pancreas (1.21-12.05%, or 11.9-118.6 μM) and PDAC tumors (0-0.69%, or 0-6.78 μM) (39,146). Thus, KDM2A activity can be expected to be substantially compromised in hypoxic regions of PDAC tumors. Interestingly, *KDM2A* transcripts were slightly elevated by hypoxia **(Supp Figure 2.S12I)**. While prior studies have shown KDM2A expression to be HIF-1α-dependent (147), this relationship was absent in HPAF-II cells **(Supp Figure 2.S12I)**. KPCY-derived cell lines (34) also displayed increased H3K36 dimethylation in response to hypoxia **(Figure 2.7D, Supp Figure 2.S12J)**, demonstrating the generality of this phenomenon across different cell backgrounds.

To probe for a possible effect of hypoxia on the rate of histone methylation, we tested for changes in NSD2 expression in hypoxia. NSD2 was significantly more abundant in HPAF-II cells at 1% O_2 than at 21% O_2 without growth factors **(Figure 2.7E)**. Interestingly, *NSD2* transcripts were depleted in hypoxic HPAF-II cells, and scRNA-seq patient data demonstrate a negative correlation between *NSD2* abundance and the HIF gene signature **(Supp Figure 2.S13A,B)**. Changes in *NSD2* abundance in hypoxia were insensitive, however, to knockdown of HIF-1α and HIF-2α or inhibition of MEK and JNK **(Supp Figure 2.S13C,D)**. Searching for possible post-translational mechanisms to explain the elevated expression of NSD2 in hypoxia, we noted that dephosphorylation by PP2Cδ promotes NSD2 proteasomal degradation (148) and recalled that *PPM1D*, which encodes PP2Cδ, was depleted in hypoxia **(Figure 2.4I)**. Consistent with the potential mechanism implied, NSD2 expression was elevated in response to PP2Cδ inhibition, and to a lesser degree in response to PP2A inhibition **(Figure 2.7F)**. While NSD2 knockdown

impeded H3K36 dimethylation in response to hypoxia or growth factors, it preferentially antagonized EMT in response to hypoxia **(Figure 2.7G, Supp Figure 2.S13E)**, indicating that growth factors may be less dependent on NSD2 for EMT. Hypoxia-mediated EMT and H3K36 dimethylation were also Nsd2- and Kdm2a- dependent in engineered KPCY-derived cell lines described in previous work (34). In baseline-mesenchymal 3077c4 cells, *Nsd2* knockout impeded H3K36 dimethylation and vimentin expression and promoted E-cadherin expression in both 21% and 1% O_2 **(Supp Figure 2.S13F)**. In baseline-epithelial 6694c2 cells, *Kdm2a* knockout promoted vimentin expression and decreased E-cadherin expression in both 21% and 1% O_2, with 1% O_2 causing an even stronger EMT **(Supp Figure 2.S13G)**. Previously reported RNA-sequencing of these cell lines (34) reveals that PP2A and PP2C subunits, as well as dual-specificity phosphatases (DUSPs), are altered in response to *Kdm2a* or *Nsd2* knockout, which provides a mechanistic link between histone methylation and MAPK activation.

We further found that MEK and JNK inhibition antagonized H3K36 dimethylation and NSD2 expression in 1% O_2, but that NSD2 expression could be rescued by co-inhibition of PP2Cδ **(Figure 2.7H)**. Knockdown of HIF-1α and/or HIF-2α also antagonized H3K36 dimethylation in 1% O_2 **(Supp Figure 2.S13H).** Collectively, these results suggest that low oxygen tension reduces KDM2A activity, which causes a suppression of serine/threonine phosphatase expression (34) that stabilizes NSD2 expression directly (through reported phosphatase/NSD2 interactions) and indirectly (through regulation of MAPK activity).

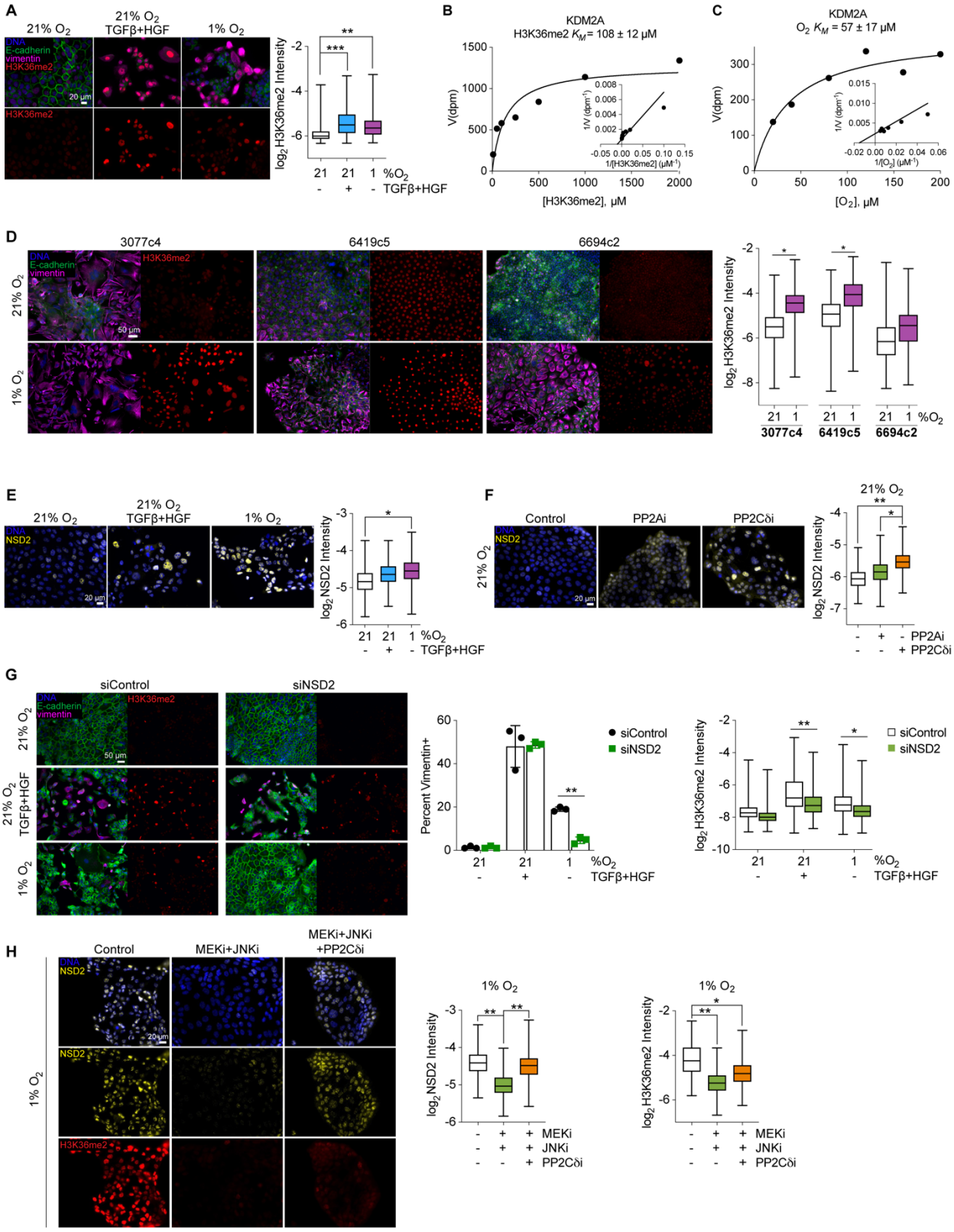

Figure 2.7 Hypoxia lowers the activity of KDM2A and stabilizes NSD2 expression to promote a histone methylation-dependent EMT

(A) HPAF-II cells were cultured in 21% O_2 with or without 10 ng/mL TGFβ + 50 ng/mL HGF or in 1% O_2 for 120 hr, and H3K36 dimethylation (H3K36me2) was measured by immunofluorescence microscopy. *n* = 3, mixed-effects analysis with Tukey's multiple comparisons test. **(B-C)** Michaelis-Menten saturation curves were created with associated Lineweaver-Burk plots for KDM2A binding kinetics for **(B)** H3K36me2 and **(C)** oxygen, where velocity (*V*) is reported as disintegration parts per minute (dpm). Plots show data for one representative run, with solid lines corresponding to the model fits to the data shown. (S.K.S.) **(D)** KPCY-derived cell lines 3077c4, 6419c5, and 6694c2 were cultured in 21% or 1% O_2 for 120 hr. Cells were then fixed and stained with antibodies against the indicated proteins, and immunofluorescence microscopy was performed. *n* = 3, mixed-effects analysis for H3K36me2 per cell line. **(E)** Immunofluorescence microscopy was performed for NSD2 expression in HPAF-II cells treated as in (A). *n* = 3, mixed-effects analysis with Tukey's multiple comparisons test against the 21% O_2 condition. **(F)** HPAF-II cells were cultured for 120 hr in 21% O_2 with 5 μM LB100 (PP2Ai), 1.5 μM sanguinarine chloride (PP2Cδi), or DMSO. Immunofluorescence microscopy was performed for NSD2. *n* = 3, mixed-effects analysis with Tukey's multiple comparisons for all conditions. **(G)** HPAF-II cells were transfected with control or NSD2 siRNA. 24 hr later, cells were treated as described in (A) for 120 hr. Immunofluorescence microscopy was performed for the indicated proteins. *n* = 3, two-way ANOVA for vimentin positivity with Sidak's multiple comparisons test and mixed-effects analysis for H3K36me2 with Tukey's multiple comparisons test. **(H)** HPAF-II cells were cultured in 1% O_2 with 1 μM CI-1040 (MEKi), 10 μM SP600125 (JNKi), and 1.5 μM sanguinarine chloride (PP2Cδi), or DMSO for 120 hr. *n* = 3, mixed-effects analysis with Tukey's multiple comparisons test. * $p < 0.05$, ** $p < 0.01$, *** $p < 0.001$

2.5 DISCUSSION

This study establishes that hypoxia and EMT are so typically related in PDAC that statistically significant relationships can be established from three types of patient data and four different mouse models. In the integrated molecular mechanism we propose **(Figure 2.8)**, low oxygen tension reduces KDM2A activity, resulting in H3K36 dimethylation and decreased protein phosphatase expression. Loss of phosphatases promotes SFK and MAPK signaling, which cooperates with reduced PP2Cδ activity to stabilize NSD2 expression, creating a reinforcing positive feedback that leads to a durable EMT. ERK and JNK also stabilize HIF-1α, which plays a supporting, but not primary, role. Collectively, ERK, JNK, and H3K36me2 promote the expression of c-Jun, HIF-1α and other transcription factors that drive EMT.

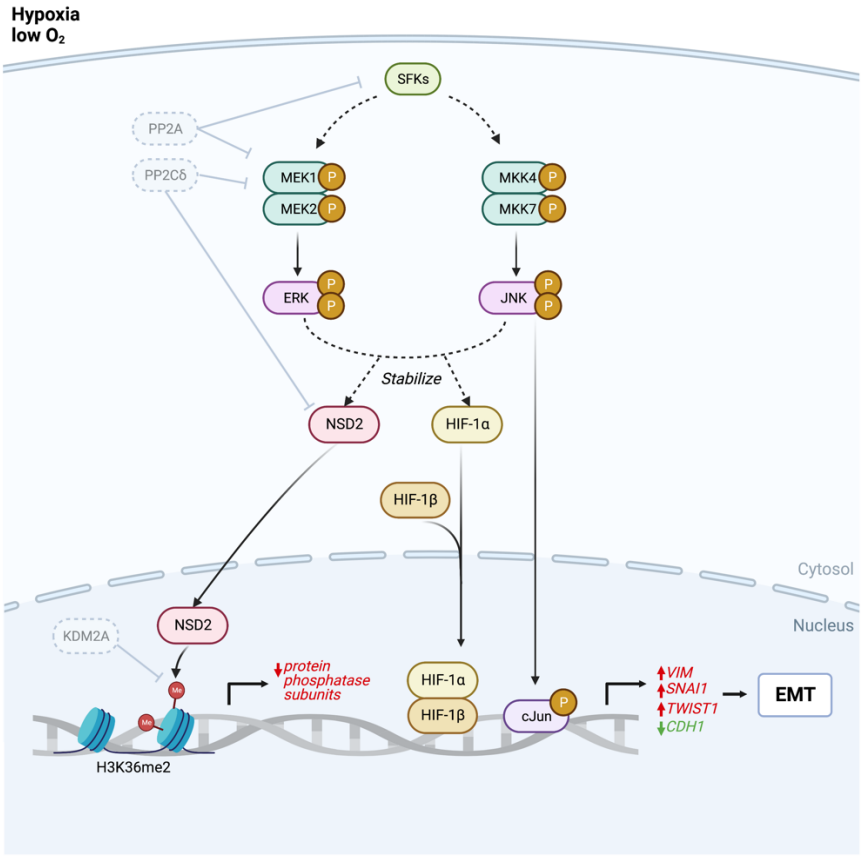

Figure 2.8 Hypoxia promotes EMT through the integrated regulation of histone methylation and MAPK signaling

Hypoxia suppresses KDM2A activity resulting in dimethylation of H3K36, which in turn suppresses expression of protein phosphatase subunits. Decreased protein phosphatase expression promotes SFK and MAPK signaling to stabilize NSD2, HIF-1α, and nuclear c-Jun expression. Elevated NSD2 expression further promotes H3K36 dimethylation, reinforcing the integrated kinase signaling/histone methylation regulatory loop. Collectively, this promotes expression of EMT-regulating genes. Figure created with BioRender.com.

Even with these mechanistic connections established, there remains some uncertainty about the rate-limiting step for epithelial reversion and H3K36 demethylation after hypoxic cells are returned to a normoxic environment. Previously hypoxic cells do revert to an epithelial state quickly after kinase inhibitors are applied. Thus, one possibility is that hypoxic cells become stuck in a metastable mesenchymal state that can only be reversed by severe intervention. EMT can exhibit hysteresis, with bistable or even tristable states (149), depending on the cell type and duration of EMT-induction (150). Further, JNK (151), ERK (152), and HIF-1α (153) signaling can all exhibit bistability depending on the initiating signaling event. Epigenetic modifications maintained by bistable signaling feedbacks could confer a cellular memory effect leading to persistent EMT (154).

Previous work has identified MAPK signaling as a target for PDAC combination therapy. For example, MEK/ERK inhibitors have been combined with anti-PD-L1 (155) and PI3K inhibitors (156), and low-dose “vertical inhibition” of RAF and ERK may promote a mesenchymal-epithelial transition in KRAS-mutant PDAC (157). ERK1/2 inhibition as a monotherapy for PDAC is ineffective due to an autophagic response that sustains viable tumor cells, but combined ERK and autophagy inhibition can suppress PDAC tumor growth (158). JNK signaling is activated in PDAC by treatment with 5-fluorouracil plus leucovorin (5-FU+LEU) or FOLFOX (5-FU+LEU plus oxaliplatin), and JNK inhibition reduces FOLFOX chemoresistance (137). Our findings provide specific motivation for pursuing combinations of MAPK inhibitors for the complete antagonism of hypoxia-mediated EMT, which may potential PDAC response to chemotherapy.

Due to the broad significance of HIFs across oncology, inhibitors of HIF dimerization, DNA binding, expression, and synthesis have been created or identified. While there has only been limited success of these inhibitors thus far in clinical trials (159), HIF inhibitors could potentially be useful components of combination therapies for PDAC. Indeed, in the mechanism we elucidated, HIFs played an important supporting role, but they were not solely responsible for hypoxia-mediated EMT.

Although we focused on the role of H3K36me2, other epigenetic changes, including histone 3 lysine 4 acetylation (H3K4Ac), H3K4me2, and H3K27me3, have been reported to regulate EMT marker genes (e.g., *CDH1, VIM*) (35,36). We focused on H3K36me2 given its reported role in EMT in PDAC specifically (34). Enzymes that modify epigenetic marks are also being considered as drugs targets. While most of the small number of clinical trials directly targeting histone methylation are focused on lymphomas, there are some initial phase trials in solid tumors (160). Inhibitors have been identified against methyltransferases (161), the methyltransferase enhancer EZH2 (160), and histone deacetylases (HDAC) (162). While HDAC inhibition alone is ineffective in PDAC due to a potential tumor supportive effect on stromal cells (163), HDAC inhibitors combined with MEK inhibitors (164) or gemcitabine (165) may hold promise. The critical role that NSD2 plays in hypoxia-mediated EMT in PDAC provides rationale for targeting of NSD2. Due to the documented role of NSD2 in multiple cancers (166), NSD2 inhibitors are in pre-clinical development, with multiple compounds identified that target the methyl-transferring SET domain (167,168).

While the accumulation of NSD2 we observed in hypoxia was apparently post-translationally regulated, others have reported hypoxia- and HIF-1α-dependent *NSD2* transcript accumulation in melanoma cells (169). Thus, different mechanisms may regulate NSD2 abundance in hypoxia, and these may leverage different NSD2 protein domains. We found there are several core HIF-binding sites (5'-RCGTG-3') (170) in the *NSD2* promoter region. However,

other transcription factors cooperate with HIF in a tissue- and gene-specific manner (171), which may explain why HIF does not regulate *NSD2* transcription in all settings (170). Our work demonstrates that hypoxia can also regulate NSD2 through downregulation of PP2Cδ, which dephosphorylates and destabilizes NSD2 (148), and through MAPK activity. The latter effect may occur through the presence of NSD2 PEST domains, protein motifs that can slow protein turnover when phosphorylated (172,173). The online tool ePESTfind reports that NSD2 has two regions (531 – 546 and 615 – 656) with high PEST scores (>5). Further, using the online iGPS algorithm (174) with a lenient threshold predicts that JNK and ERK phosphorylate NSD2 threonine 544 and serines 631 and 639. Thus, hypoxia may stabilize NSD2 in part through a MAPK-dependent process involving PEST phosphorylation.

Of course, hypoxia also promotes profound metabolic changes that contribute to aggressive disease in PDAC (175), and metabolic reprogramming can be accompanied by changes in EMT markers and phenotypes (176). In pancreas cancer cells, hypoxia-mediated expression of the mesenchymal protein N-cadherin in hypoxic culture is glucose- and glutamine-dependent, indicating that glycolytic and glutaminolytic activity influence hypoxia-mediated EMT (177). Further, MEK and JNK are involved in the Warburg effect by interacting with key metabolic regulators in glycolysis (178), and some epigenetic modifiers are energy sensors that respond to intracellular energy levels (179). Thus, there are likely to be metabolic dependencies involved in the process we elucidated that have yet to be explored.

While our analysis focused on ductal epithelial cells, tumor hypoxia may also affect stromal cells including cancer-associated fibroblasts (CAFs) and tumor-associated macrophages (TAMs). In PDAC, inflammatory CAFs secrete growth factors and cytokines (e.g., TGFβ, IL-6, TNFα) that have been identified as EMT agonists (48). Pancreatic stellate cells, the progenitors of PDAC CAFs, secrete IL-6 in hypoxic culture (180). Hypoxia-mediated ERK activation drives TAM polarization to a pro-inflammatory M2 phenotype in lung cancer (181), in which M2-like TAMs

have been shown to secrete cytokines to promote EMT in PDAC (182). Therefore, it is possible that tumor hypoxia could promote EMT in neoplastic cells through mechanisms that depend on other cell types present in the tumor microenvironment.

The observation that hypoxia generally led to heterogeneous effects among cells prompts the question of why only some cells respond to hypoxia by undergoing EMT. In colon cancer cells, baseline differences in signaling activity among cells revealed by scRNA-seq correlated with a baseline EMT state (77). Such effects could underlie the phenomena we observed. For example, nuclear c-Jun accumulation and H3K36me2 were only strongly apparent in a subset of cells. While we have not focused on this question here, it is worth exploring the degree to which signaling heterogeneities may explain EMT phenotypic heterogeneities in the hypoxic PDAC setting.

Finally, the durable nature of hypoxia-mediated EMT could make this mechanism especially likely to contribute to metastatic dissemination. At the same time, our finding that hypoxia-driven EMT can persist for weeks may challenge the typical view that a mesenchymal-epithelial transition is required for metastatic outgrowth. Additional work is needed to investigate these questions.

2.6 ACKNOWLEDGEMENTS

We thank Dr. Marieke Jones (UVA) for her invaluable guidance with statistical analyses. We thank Dr. John Tobias (University of Pennsylvania), Dr. Danielle Gilkes (Johns Hopkins), and Dr. Shayn Peirce-Cottler (UVA) for helpful technical discussions. We acknowledge Dr. Yi Zhang (Harvard) for creating the original *KDM2A* plasmid, Dr. Jing-Yi Chen (I-Shou University) for providing a sample of the *KDM2A* plasmid, Dr. David Tuveson (Cold Springs Harbor Laboratory) for sharing annotated scRNAseq data, Dr. Kevin Janes (UVA) for providing the GFP plasmid, Dr. Robert Norgard (University of Pennsylvania) for assistance in providing KPCY tumor sections, and the senior authors of the CPTAC PDAC Discovery Study for assistance interpreting their datasets.

2.7 SUPPLEMENTAL MATERIAL

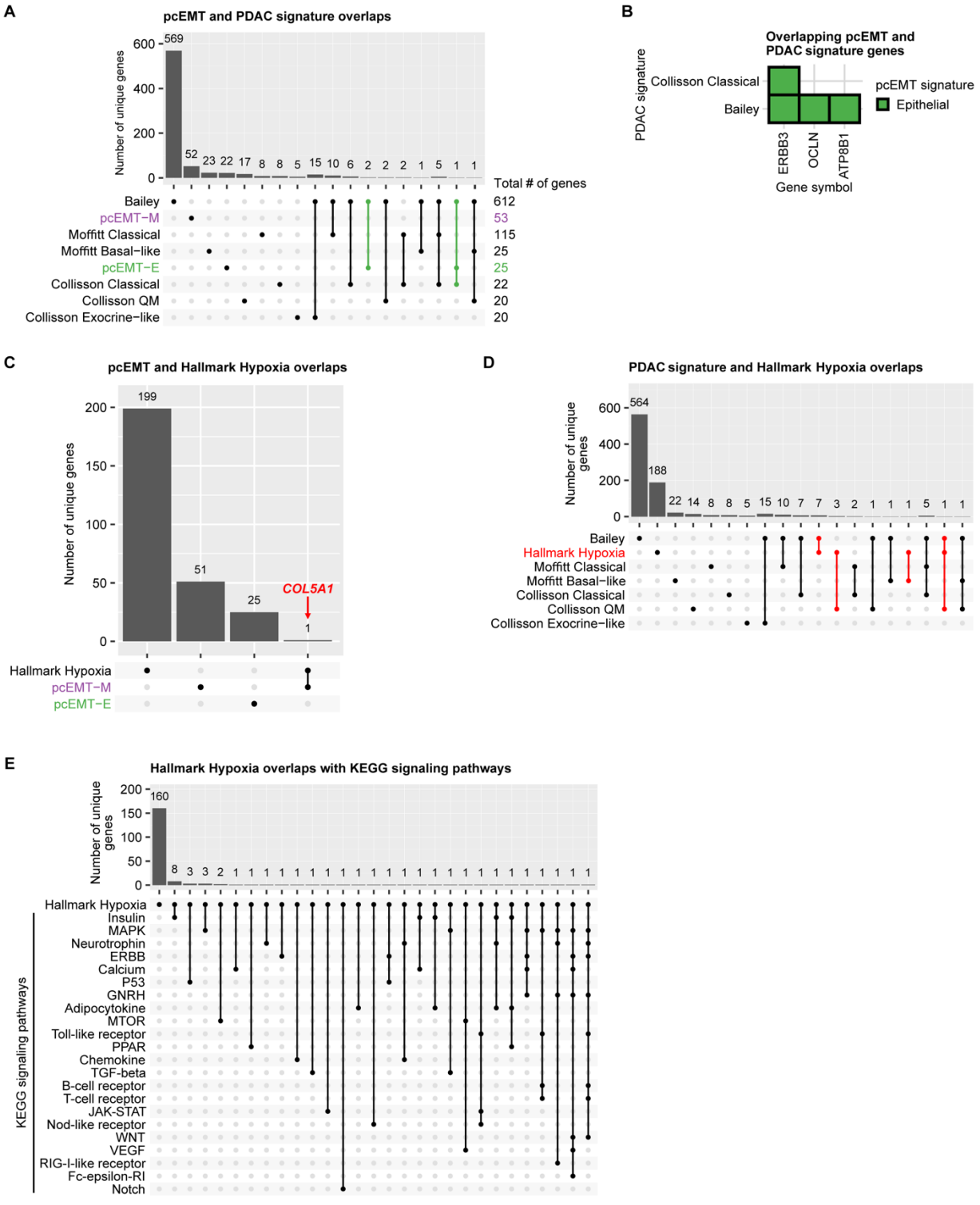

Supp Figure 2.S1 There is little overlap among the pan-cancer EMT (pcEMT), Hallmark Hypoxia, and established PDAC subtype gene signatures

(A) An UpSet plot shows the number of unique genes for comparisons made among the pcEMT signature and Collisson, Moffitt, and Bailey PDAC signatures. Note that subtypes are not shown for the Bailey PDAC signature because the genes defining each subtype were not explicitly defined by the original authors. UpSet plots were formatted left to right to show entries for single gene sets (which reflect the number of genes unique to those gene sets alone) followed by entries showing intersections across gene sets, with each type of entry arranged in rank order by cardinality. Bars are highlighted in green where at least one other gene set shares one or more gene features with the epithelial component of the pcEMT signature (pcEMT-E). **(B)** pcEMT genes overlapping with the indicated PDAC signatures are shown. **(C)** An UpSet plot was created for the pcEMT-E, pcEMT-M, and Hallmark Hypoxia gene sets Only *COL5A1* is common to the pcEMT-M and Hallmark Hypoxia gene sets. **(D)** An UpSet plot was created for comparisons among the Hallmark Hypoxia, Bailey, Collison, and Moffitt gene sets. Bars are highlighted in red where at least one other gene set shares one or more gene features with the Hallmark Hypoxia gene set. **(E)** An UpSet plot was created for comparisons among the Hallmark Hypoxia and indicated KEGG signaling pathway gene sets. (P.J.M.)

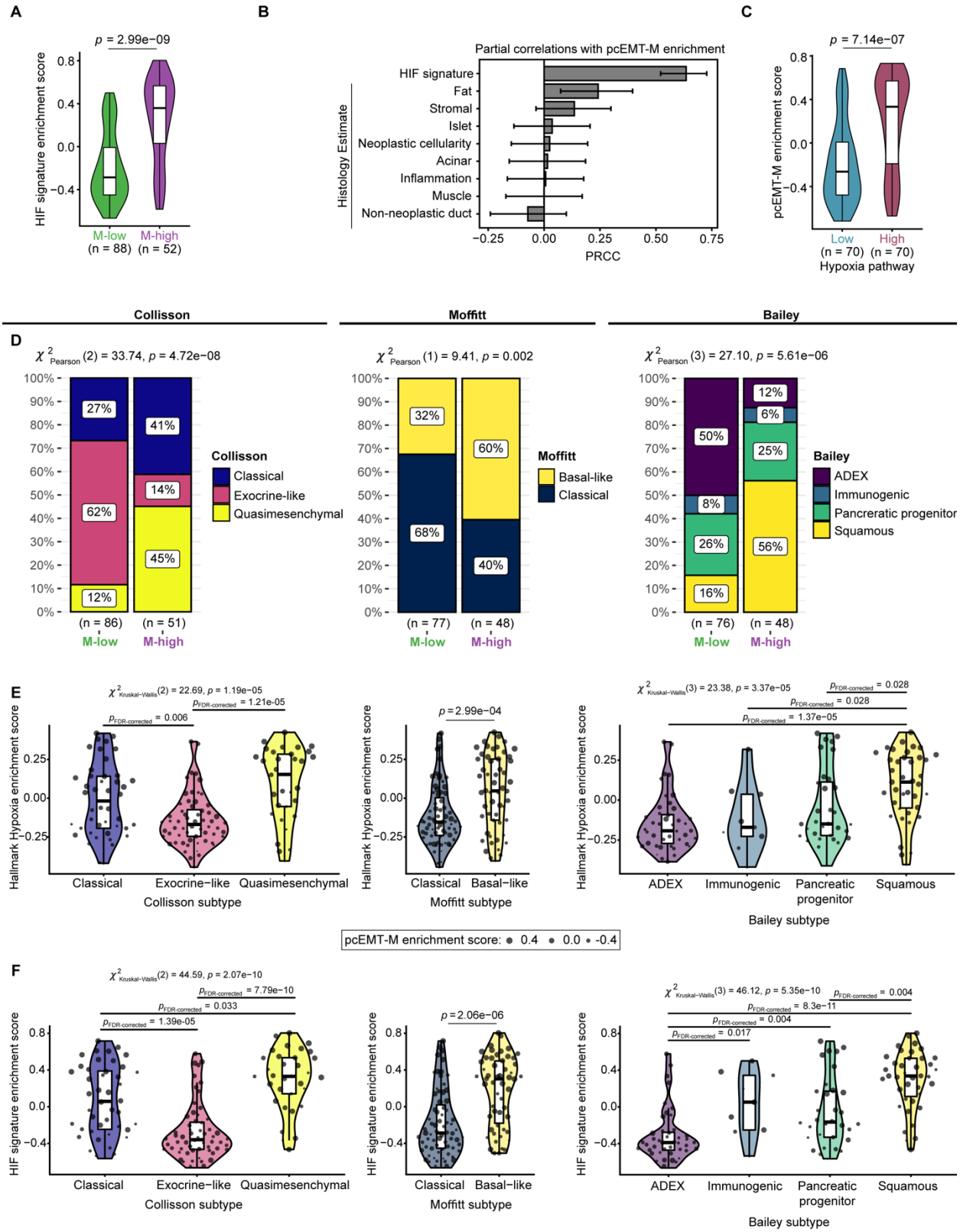

Supp Figure 2.S2 Across different classification schemes, aggressive PDAC subtypes are correlated with an increase in hypoxic gene signatures

(A) CPTAC PDAC tumor proteomics data were clustered by non-negative matrix factorization using the protein analogs of the pcEMT signature as features, as shown in Figure 2.1. HIF signature GSVA enrichment scores were calculated for the resulting clusters of mesenchymal-high (M-high) and mesenchymal-low (M-low) tumors, with a Mann-Whitney U test. **(B)** Partial rank correlation coefficients (PRCCs) of the indicated variables were calculated with respect to protein enrichment (GSVA) scores for the mesenchymal portion of the pcEMT signature (pcEMT-M). HIF signature enrichment scores were calculated from the CPTAC PDAC global proteomics data using GSVA. Histology estimates were used as provided with the CPTAC data. Error bars denote 95% confidence intervals. **(C)** Protein enrichment of pcEMT-M was computed by GSVA and compared between hypoxia-high and hypoxia-low CPTAC PDAC tumors. Hypoxia status was used as previously described (78), with a Mann-Whitney U test. **(D)** Comparisons are shown of Collisson, Moffitt, and Bailey subtype proportions across pcEMT M-low and -high tumor groups for CPTAC PDAC tumors. Collisson, Moffitt, and Bailey subtype classifications were used as reported previously (78). The results of Pearson's chi-squared test comparing the proportions of PDAC subtypes between the two pcEMT groups are shown above each plot. **(E)** Hallmark Hypoxia GSVA enrichment scores were calculated from protein expression of CPTAC PDAC tumors and compared across subtypes within the Collisson, Moffitt, and Bailey classification systems. Results of the Kruskal-Wallis test or Mann-Whitney U test are shown above each plot. Pairwise comparisons for the Collisson and Bailey subtypes were computed using the Dunn test, and *p* values were adjusted for multiple comparisons using the Benjamini-Hochberg/FDR method. **(F)** HIF signature GSVA scores were calculated from protein expression of CPTAC PDAC tumors and compared across subtypes within the Collisson, Moffitt, and Bailey classification systems. The size of dots in (E) and (F) indicates the pcEMT-M enrichment score for each tumor. Results of the Kruskal-Wallis test or Mann-Whitney U test are shown above each plot. Pairwise comparisons for the Collisson and Bailey comparisons were computed using the Dunn test, and *p* values were adjusted for multiple comparisons using the Benjamini-Hochberg/FDR method. (P.J.M.)

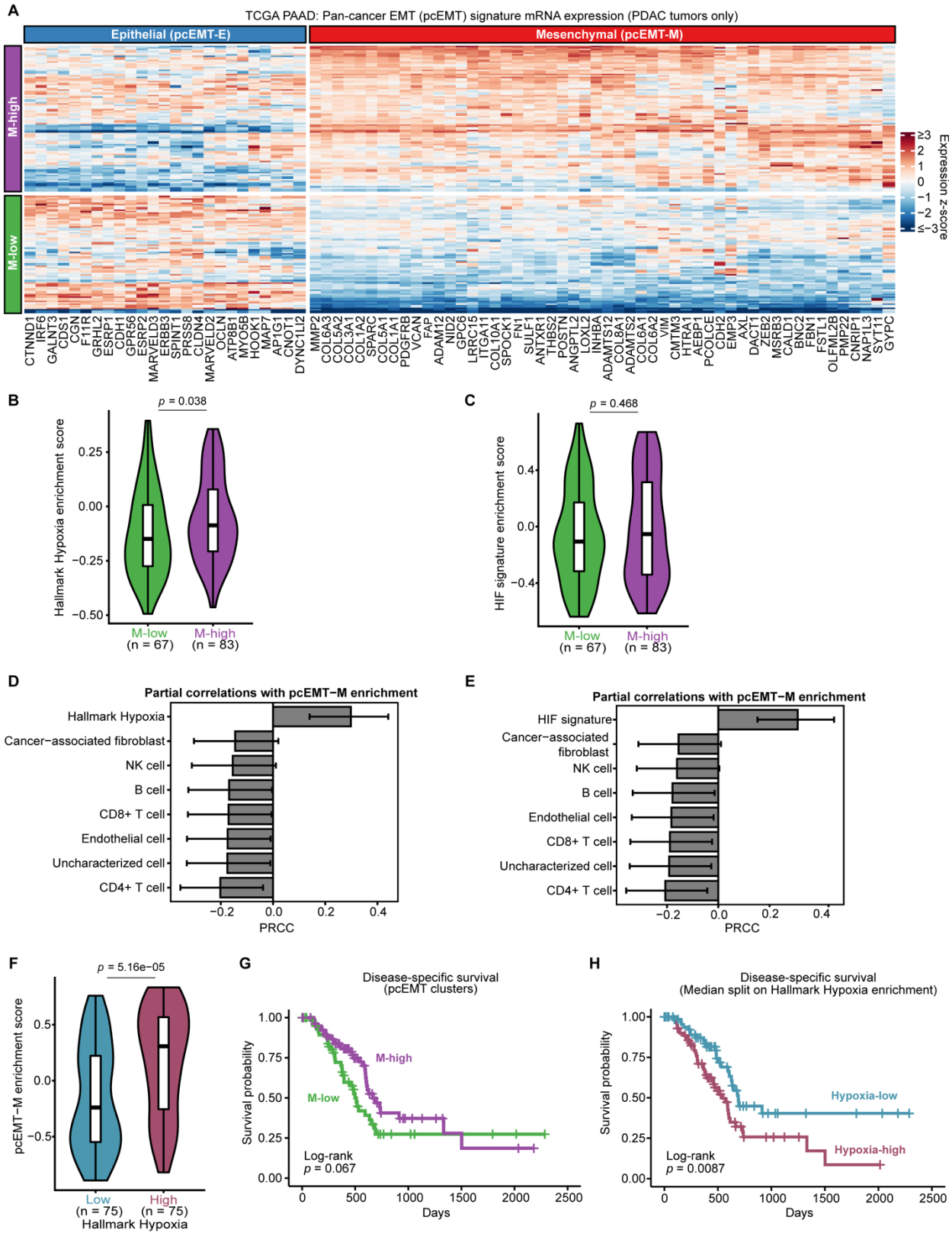

Supp Figure 2.S3 EMT and hypoxia gene enrichment are correlated in TCGA PDAC tumors

(A) TCGA PAAD tumor samples were clustered using non-negative matrix factorization (NMF) of log_2(TPM+1) expression data for genes from the pan-cancer EMT (pcEMT) signature. Heatmap indicates per-gene, z-scored log_2(TPM+1) expression values. The left vertical side bar indicates the assigned NMF cluster for each tumor. The top horizontal side bar indicates the phenotype associated with each gene as described in the original pcEMT signature (89). **(B)** Hallmark Hypoxia or **(C)** HIF target signature GSVA (enrichment) scores were calculated for TCGA PAAD study PDAC tumors and compared across the NMF-assigned pcEMT clusters. The Mann-Whitney U test indicated that there was a statistically significant difference in medians between the clusters. **(D,E)** Partial rank correlation coefficients (PRCCs) of the indicated TCGA PAAD immune deconvolution cell type estimates (estimated using the EPIC algorithm) and **(D)** Hallmark Hypoxia signature or **(E)** HIF target signature GSVA scores were calculated with respect to GSVA scores for the mesenchymal portion of the pcEMT signature (pcEMT-M). Error bars denote 95% confidence intervals for the indicated PRCCs. **(F)** pcEMT-M GSVA scores were calculated for TCGA PAAD study PDAC tumors and compared when tumors are split into hypoxia-high and hypoxia-low groups based on the median Hallmark Hypoxia GSVA score. **(G)** Kaplan-Meier survival curves were calculated for PDAC patients from the TCGA PAAD study, with stratification based on tumor pcEMT groups from NMF clustering, with log-rank test. **(H)** Kaplan-Meier survival curves were calculated for PDAC patients from the TCGA PAAD study, with stratification based on median Hallmark Hypoxia GSVA score, with log-rank test. (P.J.M.)

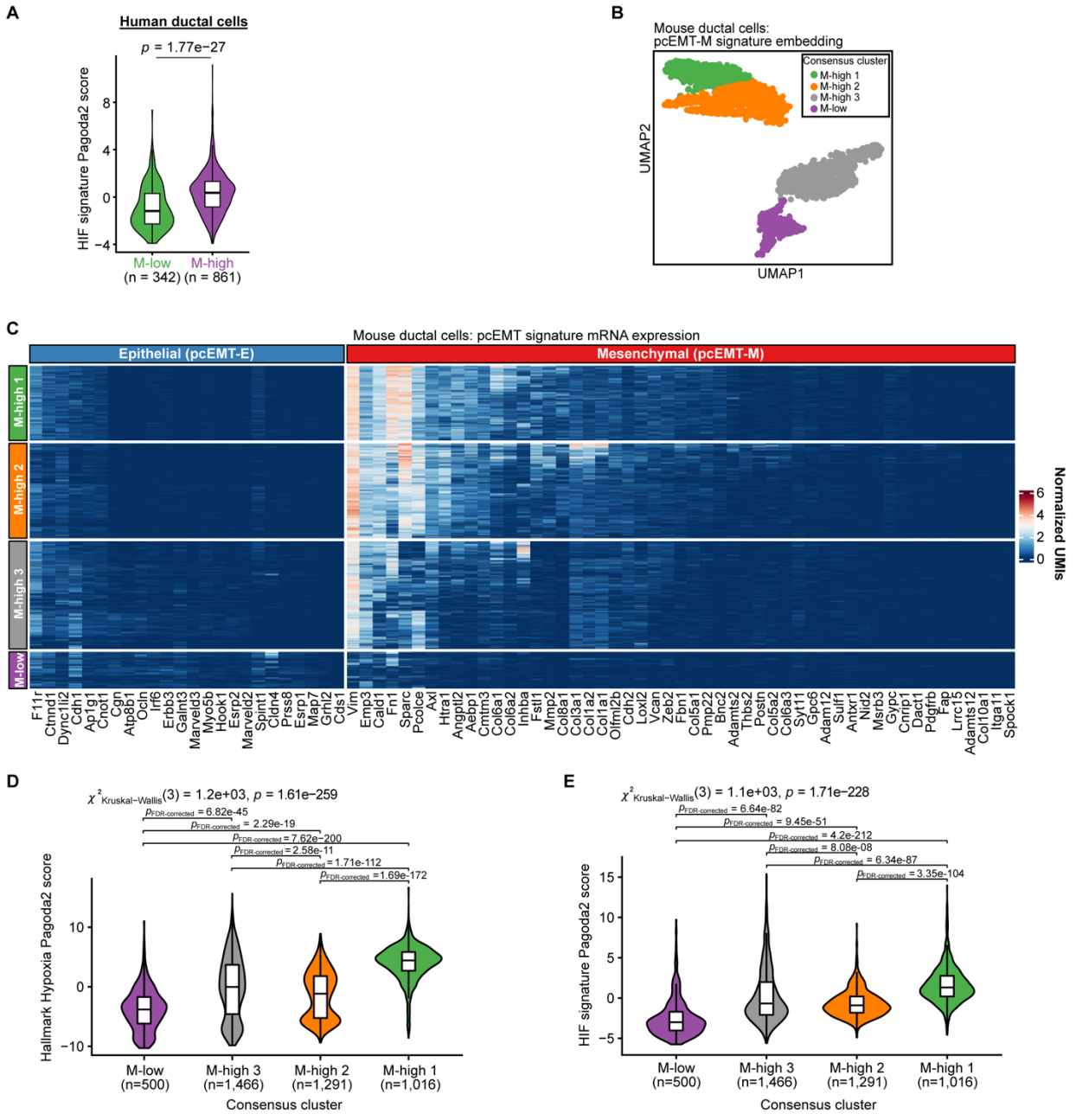

Supp Figure 2.S4 Mesenchymal mouse ductal cells are enriched for hypoxia-associated gene expression

(A) mRNA enrichment of the HIF target signature was compared between M-high and M-low human ductal cells (88) from Figure 2.1E, with Mann-Whitney U test. **(B)** Mouse ductal cells (88) were projected onto a 2D UMAP embedding of the mesenchymal portion of the pcEMT signature. The UMAP projection was then clustered using consensus clustering, and clusters were labeled by comparing the expression profiles of mesenchymal genes, as shown in (C). **(C)** A heatmap is shown of the consensus cluster-annotated heatmap of mRNA transcript abundances (normalized UMIs) for genes from the full pcEMT signature that are expressed in mouse ductal cells. **(D)** Hallmark Hypoxia Pagoda2 scores were compared across the mouse ductal cell pcEMT consensus clusters. The Kruskall-Wallis test indicated that there was a statistically significant difference in medians among the distributions. Pairwise comparisons were computed using the

Dunn test, and *p* values were adjusted for multiple comparisons using the Benjamini-Hochberg/FDR method. **(E)** HIF target signature Pagoda 2 scores were compared across the mouse ductal cell pcEMT consensus clusters. The Kruskall-Wallis test indicated that there was a statistically significant difference in medians among the distributions. Pairwise comparisons in panels (D) and (E) were computed using the Dunn test, and *p* values were adjusted for multiple comparisons using the Benjamini-Hochberg/FDR method. (P.J.M.)

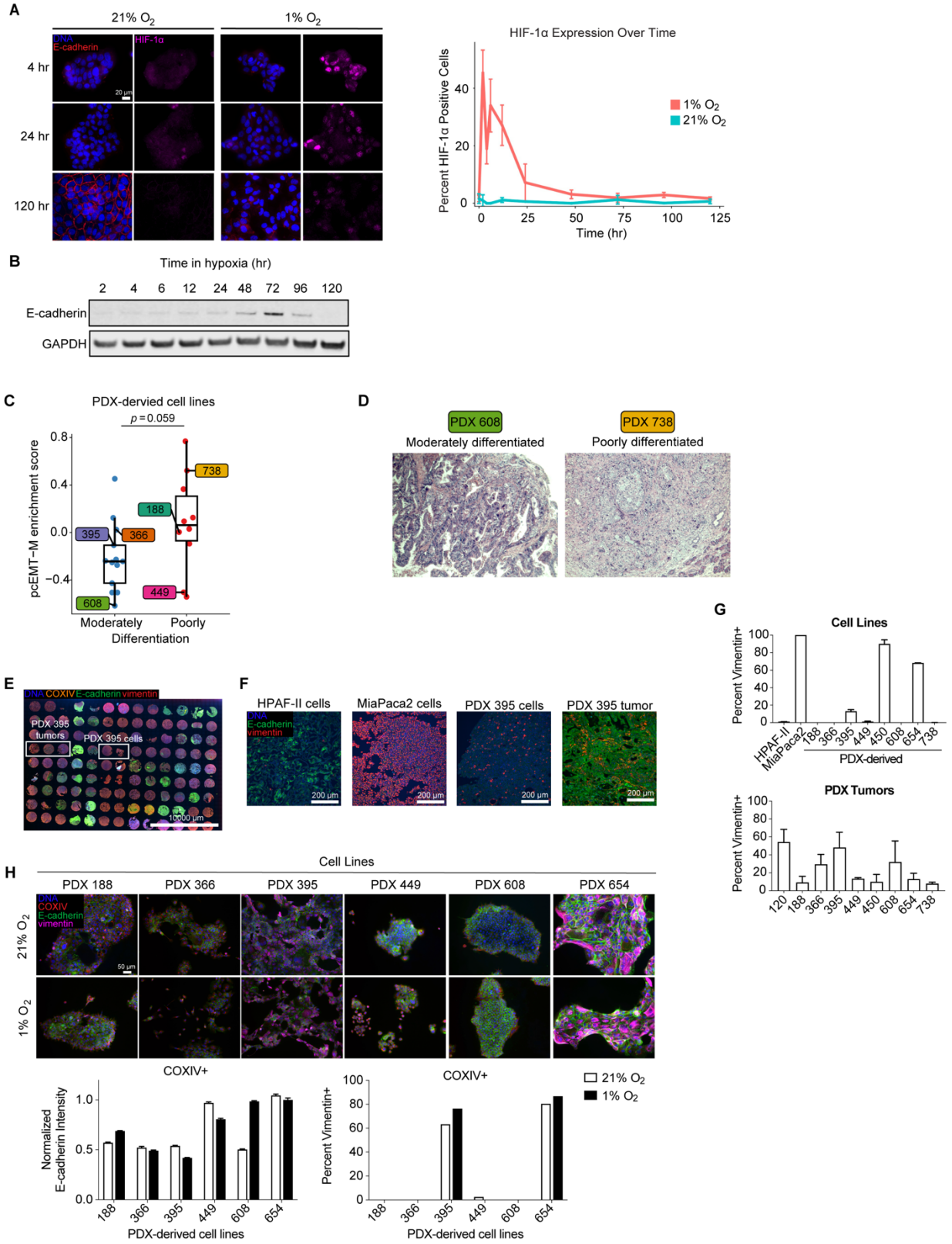

Supp Figure 2.S5 HIF-1α expression is transient in response to hypoxia, and PDX-derived cell lines exhibit evidence of hypoxia-mediated EMT

(A) HPAF-II cells were cultured in 21% or 1% O_2 for up to 120 hr. At the time points indicated, cells were fixed and stained with antibodies for E-cadherin and HIF-1α. Fluorescence microscopy was performed, with quantitative image analysis for nuclear HIF-1α protein. Microscopy is shown for three representative time points, with *n* = 3. **(B)** HPAF-II cells were cultured in 1% O_2 for up to 120 hr and lysed at the indicated times. Lysates were analyzed by immunoblotting for the indicated proteins. **(C)** pcEMT-M signature mRNA enrichment (GSVA scores) was compared for moderately versus poorly differentiated human PDAC patient tumors, with Mann-Whitney U test. GSVA scores were calculated from RNA-seq data obtained from PDX tumors derived from the original patient tumors. (P.J.M.) **(D)** Representative images of H&E-stained sections of patient tumors used for histological grading of differentiation, with 608 and 738 exemplifying moderately and poorly differentiated tumors, respectively. Images taken with 10× objective, with 10× ocular. **(E)** A tissue microarray of PDX tumors and PDAC cell lines was stained with antibodies for E-cadherin, vimentin, and COXIV (human-specific), and fluorescence microscopy was performed. PDX 395 cell and tumor samples are boxed. **(F)** High-magnification images are shown from the tissue microarray in panel (E) of HPAF-II cells (epithelial baseline), MiaPaca2 cells (mesenchymal baseline), PDX 395 tumor, and the PDX 395-derived cell line. Exposure settings set based on the highest expressing sample to not overexpose; therefore, lower expressing cells may appear to have little to no expression. **(G)** Immunofluorescence microscopy of the tissue microarray was quantified the fraction of COXIV+ cells that were also vimentin+ for both cell lines and PDX tumors. **(H)** PDX-derived cell lines were cultured in 21% or 1% O_2 for 120hr and fixed. Immunofluorescence microscopy was performed for the indicated proteins, and images were quantified for junctional E-cadherin intensity for COXIV+ (human) cells and percent of COXIV+ cells that were also vimentin+. *n* = 1, with >1000 cells.

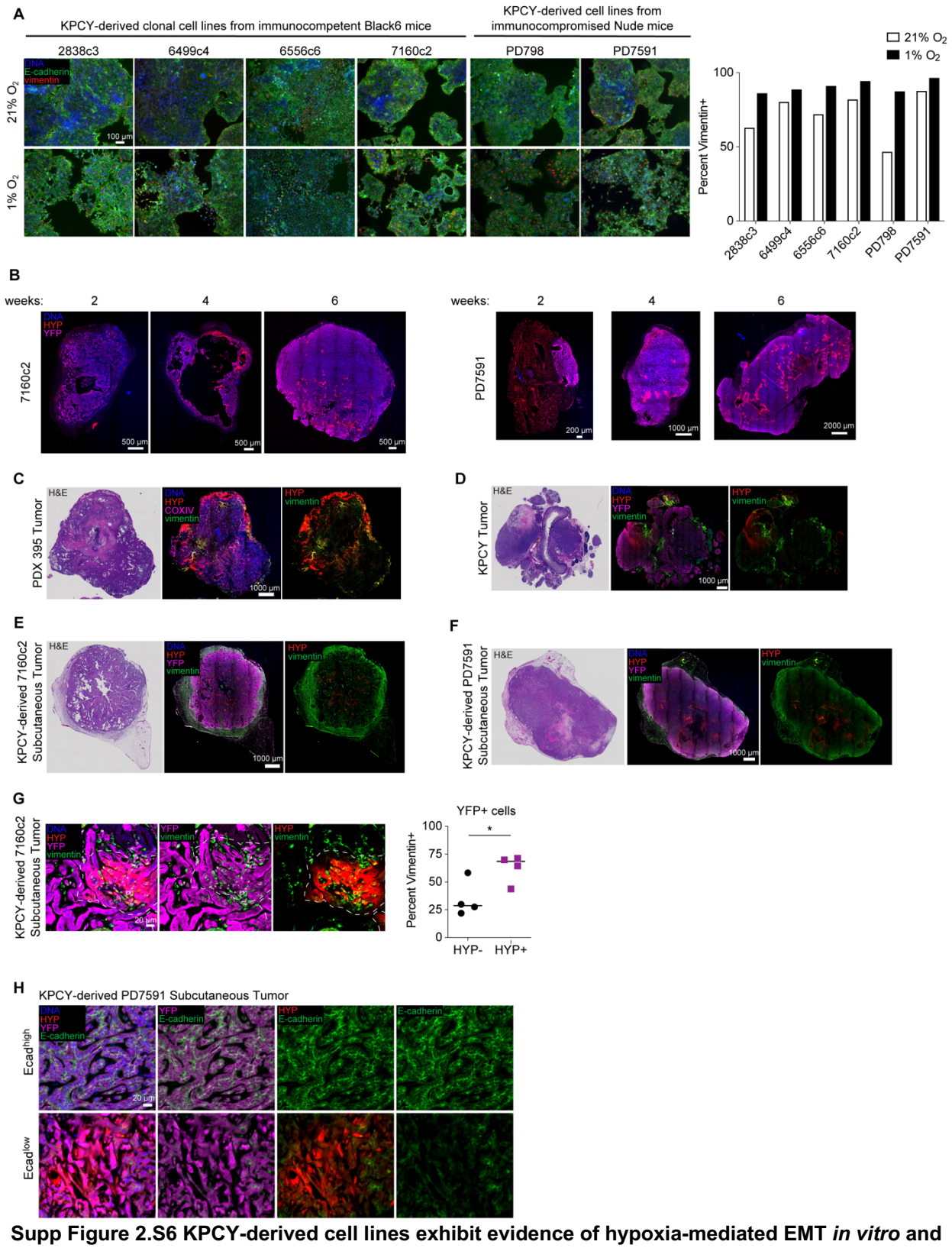

Supp Figure 2.S6 KPCY-derived cell lines exhibit evidence of hypoxia-mediated EMT *in vitro* and *in vivo*

(A) KPCY-derived cell lines were cultured in 21% or 1% O_2 for 120 hr, fixed, and stained with antibodies for E-cadherin and vimentin. Immunofluorescence microscopy was performed, with quantitative image analysis to determine the percent of vimentin+ cells, *n* = 1, with >2000 cells. **(B)** Subcutaneous tumors were formed in mice using KPCY-derived cell lines and allowed to grow for two, four, or six weeks. Fluorescent immunohistochemical staining was performed on tumor sections, which were stained with antibodies for Hypoxyprobe (HYP) and YFP (ductal cells) and imaged, *n* = 1. **(C)** Sections of orthotopically implanted PDX 395 tumor were subjected to H&E staining or to fluorescent immunohistochemistry using antibodies against COXIV (human specific), vimentin, and HYP. Visible color (H&E) or fluorescence microscopy was performed. Images are representative of *n* = 4. **(D)** Sections of KPCY autochthonous tumors were subjected to H&E staining and fluorescent immunohistochemistry for YFP, vimentin, and HYP. Microscopy shown is representative of *n* = 4. **(E, F)** Sections of subcutaneous tumors formed by implanting the KPCY-derived 7160c2 or PD7591 cell line were imaged as described in panel (D). Microscopy shown is representative of *n* = 4 for 7160c2 or *n* = 6 for PD7591. **(G)** Sections of subcutaneous tumors generated from 7160c2 cells were stained for HYP, YFP, and vimentin. Fluorescence microscopy was performed, with quantitative image analysis for the fraction of YFP+/HYP- or YFP+/HYP+ cells that were vimentin+. *n* = 4, t test. * $p < 0.05$ **(H)** Sections of subcutaneous PD7591 tumors were stained for HYP, YFP, and E-cadherin. Representative images show $Ecad^{high}$ and $Ecad^{ow}$ tissue regions, as described in Figure 2.2I. *n* = 4.

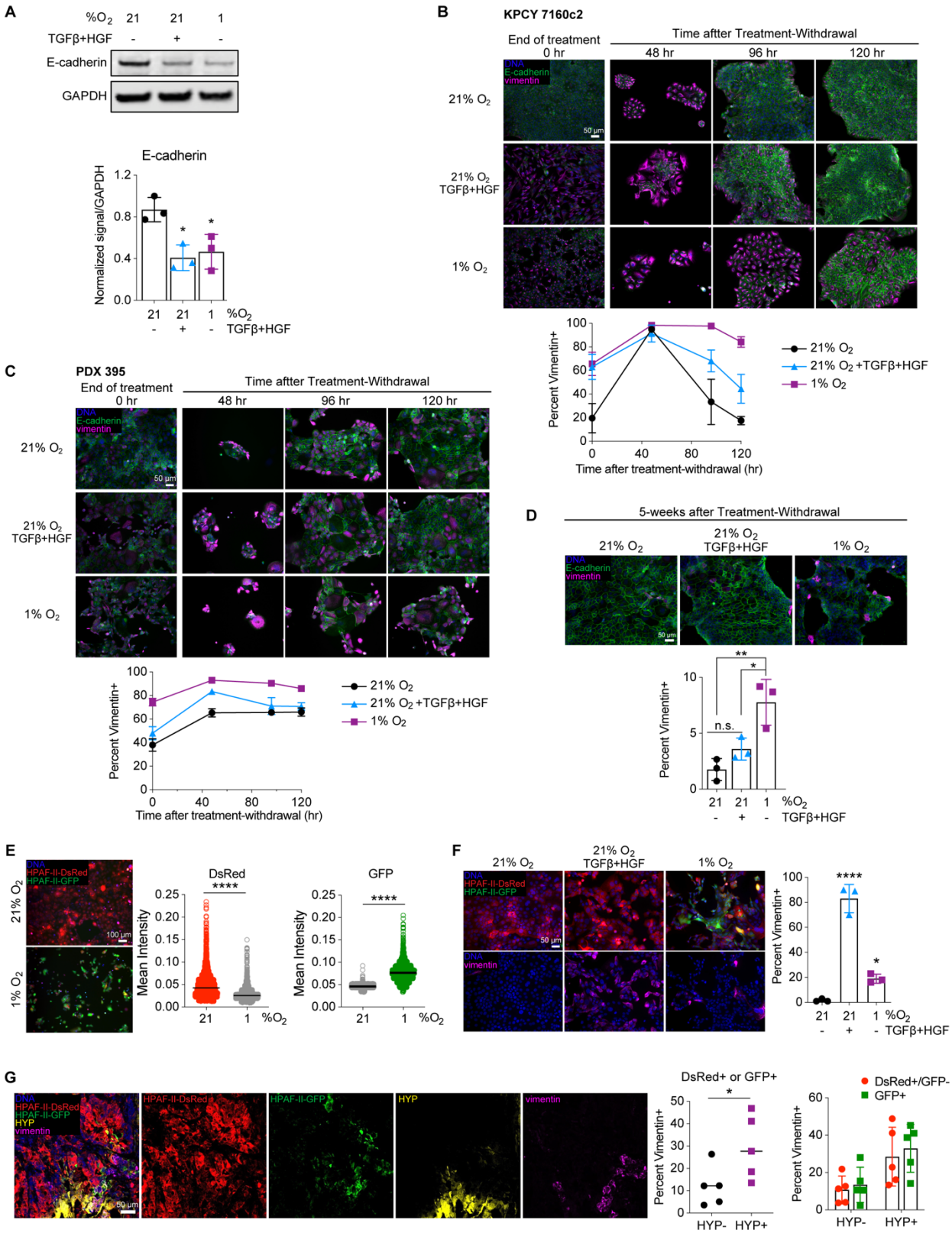

Supp Figure 2.S7 Hypoxia-mediated EMT is more durable than growth factor-driven EMT

(A) HPAF-II cells were cultured for 120 hr in 21% O_2, with or without 10 ng/mL TGFβ + 50 ng/mL HGF or in 1% O_2 for 120 hr. Cells lysates were analyzed by immunoblotting for the indicated proteins. *n* = 3, one-way ANOVA with comparison to 21% O_2. **(B)** KPCY 7160c2 and **(C)** PDX 395 cells were cultured as described in (A). Cells were then re-plated and cultured in 21% O_2 without growth factors. At the indicated times, cells were fixed. Cells were stained with antibodies against the indicated proteins, and immunofluorescence microscopy was performed with quantitative image analysis for the percentage of vimentin-positive cells. *n* = 3, data represented as mean ± s.e.m. **(D)** HPAF-II cells were treated and re-plated as described in panels (B) and (C). Five weeks after treatment-withdrawal, with passaging as needed to maintain cell health, cells were fixed and stained for the indicated proteins. Immunofluorescence microscopy with quantitative image analysis was performed. *n* = 3, one-way ANOVA with Tukey's multiple comparisons test across all groups. **(E)** HPAF-II engineered with the hypoxia fate-mapping system were cultured in 21% or 1% O_2 for 12 days. Live cells were imaged for DsRed or GFP expression, and quantification of each fluorescent protein per cell was performed. *n* = 3, t-test. **(F)** HPAF-II hypoxia fate-mapping cells were cultured as described in (A). *n* = 3, one-way ANOVA with Dunnett's multiple comparisons test against 21% O_2. **(G)** Fluorescent immunohistochemistry was performed on sections of orthotopic mouse tumors formed using HPAF-II hypoxia fate-mapping cells. Antibody staining for DsRed, GFP, vimentin, and Hypoxyprobe (HYP) was performed, followed by five-color confocal microscopy and quantitative image analysis. *n* = 5, with t test used to compare vimentin+ HPAF-II cells (DsRed+ or GFP+) that were HYP- or HYP+ and two-way ANOVA with Sidak's multiple comparison test used for a similar comparison where DsRed+/GFP- and GFP+ cells were split out separately. * $p < 0.05$, ** $p < 0.01$, *** $p < 0.001$, **** $p < 0.0001$

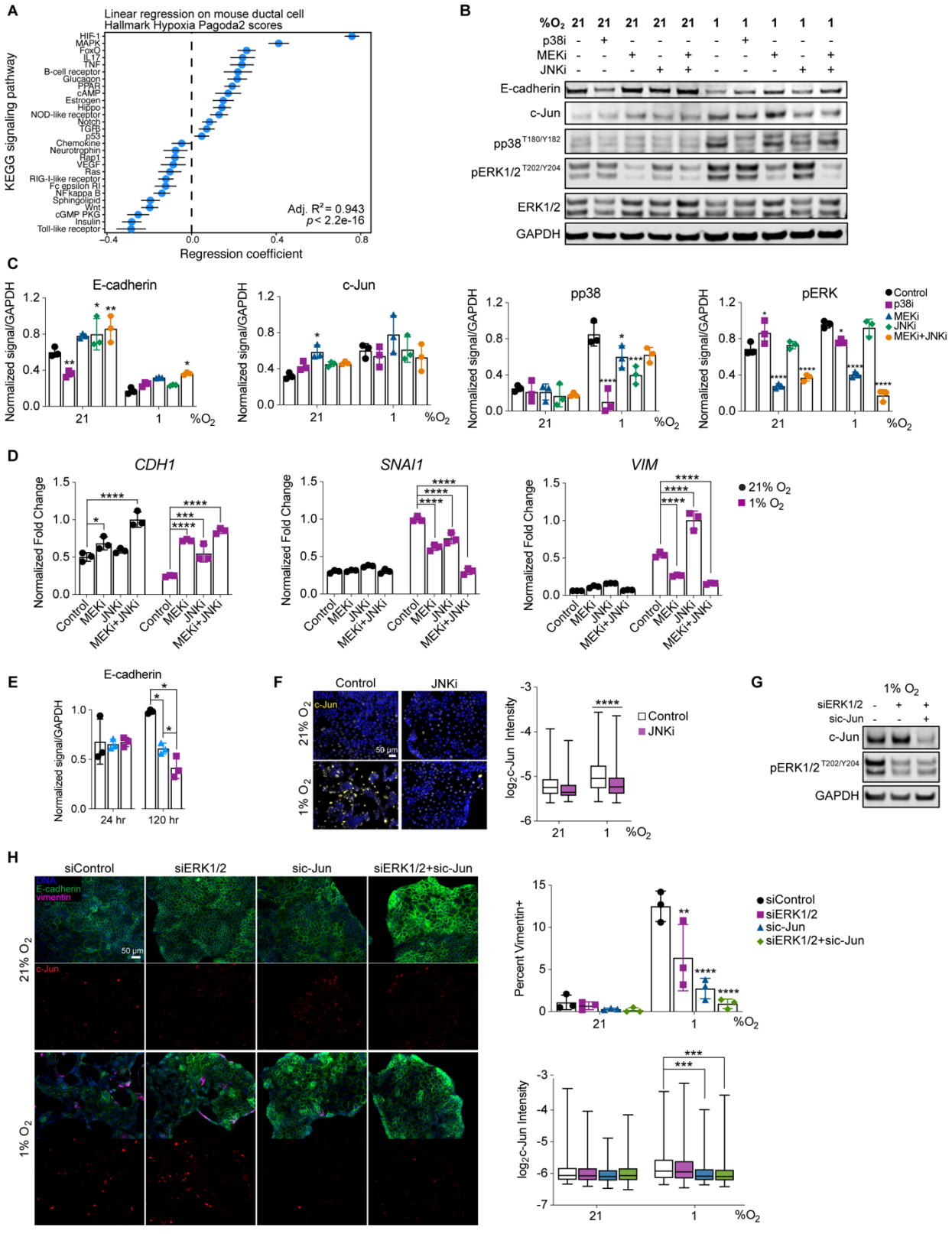

Supp Figure 2.S8 Hypoxia-driven EMT is MAPK-dependent

(A) Coefficients for the different KEGG signaling pathways are shown for the best LASSO+AIC-selected linear regression model of Hallmark Hypoxia Pagoda2 scores in mouse ductal cells. Pagoda2 scores for the indicated KEGG signaling pathways as the independent variables in the model. Error bars denote 95% confidence intervals for the indicated regression coefficient estimates. (P.J.M.) **(B,C)** HPAF-II cells were cultured in 21% or 1% O_2 with 10 μM SB203580 (p38i), 1 μM CI-1040 (MEKi), 10 μM SP600125 (JNKi), or DMSO for 120 hr, with inhibitors replenished every 48 hr. Cell lysates were analyzed by immunoblotting for the indicated proteins. *n* = 3, two-way ANOVA with Tukey's multiple comparison test against the untreated (control) condition. **(D)** HPAF-II cells were treated as described in panel (C) with the indicated inhibitors. RNA was extracted, and qRT-PCR was performed for the indicated transcripts. *CASC3* was used as a control gene for normalization. *n* = 3, two-way ANOVA with Sidak's multiple comparison test against the untreated (control) condition. **(E)** HPAF-II cells were treated and lysed as described in Figure 2.4E and quantification was performed for E-cadherin. *n* = 3, one-way ANOVA with Tukey's multiple comparisons test at each time point. **(F)** HPAF-II cells were cultured for 120 hr in 21% or 1% O_2 with 10 μM SP600125 (JNKi) or DMSO, with inhibitor replenished every 48 hr. Cells were fixed and stained for c-Jun, and image analysis was performed. *n* =3, mixed-effects analysis with Tukey's multiple comparisons test. **(G)** HPAF-II cells were transfected with siRNA targeting ERK1/2 and c-Jun or control siRNA and cultured at 1% O_2 for 24 hr. Lysates were analyzed by immunoblotting for the indicated proteins. **(H)** HPAF-II cells were transfected with siRNA targeting ERK1/2 and/or c-Jun or control siRNA. 24 hr later, cells were switched to 1% O_2 or maintained at 21% O_2. 120 hr later, cells were fixed and stained with antibodies against the indicated proteins. Immunofluorescence microscopy was performed with quantitative image analysis for the indicated proteins. *n* = 3, two-way ANOVA for vimentin positivity and mixed-effects analysis for c-Jun expression, with Tukey's multiple comparisons test. * $p < 0.05$, ** $p < 0.01$, *** $p < 0.001$, **** $p < 0.0001$

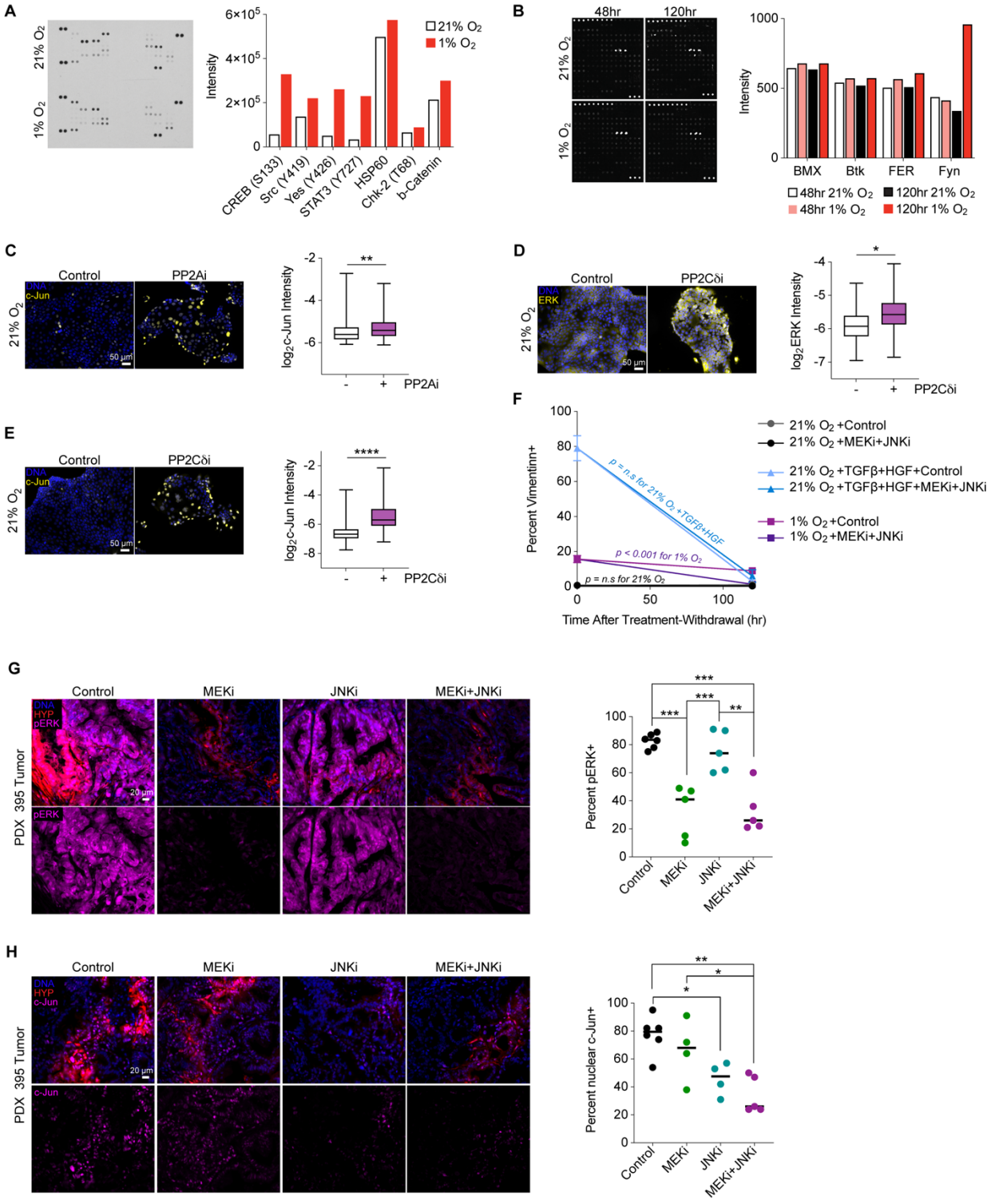

Supp Figure 2.S9 Hypoxia-mediated EMT is MAPK- and SFK-dependent

(A) The Proteome Profiler Human Phospho-kinase Array (R&D Systems; 37 phosphorylated kinases and 2 total proteins) was used to analyze lysates from HPAF-II cells cultured for 120 hr in 21% or 1% O_2. Quantification for the top seven targets that were preferentially abundant in 1% O_2 is displayed. *n* = 1. **(B)**

The Human Receptor Tyrosine Kinase Phosphorylation Array (RayBiotech; 71 targets) was used to analyzed lysates from HPAF-II cells cultured for 48 or 120 hr in 21% or 1% O_2. Quantification for the top four targets that were preferentially abundant in 1% O_2 is displayed. n = 1. **(C)** HPAF-II cells were cultured for 120 hr at 21% O_2 with 5 μM LB100 (PP2Ai) or DMSO, with inhibitors replenished every 48 hr. Cells were fixed and stained for c-Jun. Immunofluorescence microscopy was performed with image analysis for nuclear c-Jun expression. n = 3, mixed-effects analysis. **(D, E)** HPAF-II cells were cultured for 120 hr in 21% O_2 with 1.5 μM sanguinarine chloride (PP2Cδi) or DMSO, with inhibitors replenished every 48 hr. Cells were fixed and stained for c-Jun or ERK1/2. Immunofluorescence microscopy was performed with image analysis for nuclear c-Jun or nuclear ERK1/2. n = 3, mixed-effects analysis. **(F)** Rate of change in percent vimentin+ cells from Figure 2.5E. Comparisons were made against the control (DMSO) condition of fitted y-intercepts and slopes. The null hypothesis was that a single curve could capture both the control and MEKi+JNKi conditions. The null hypothesis was only rejected for 1% O_2. **(G,H)** PDX 395 tumors were treated twice daily for nine days with selumetinib (MEKi), SP600125 (JNKi), selumetinib+SP600125, or vehicle control, as described in Figure 2.5F. Tumor sections were stained and quantified for percent **(G)** pERK+ and **(H)** nuclear c-Jun+ cells. n = 4 - 6, one-way ANOVA with Tukey's multiple comparisons test. * $p < 0.05$, ** $p < 0.01$, *** $p < 0.001$, **** $p < 0.0001$

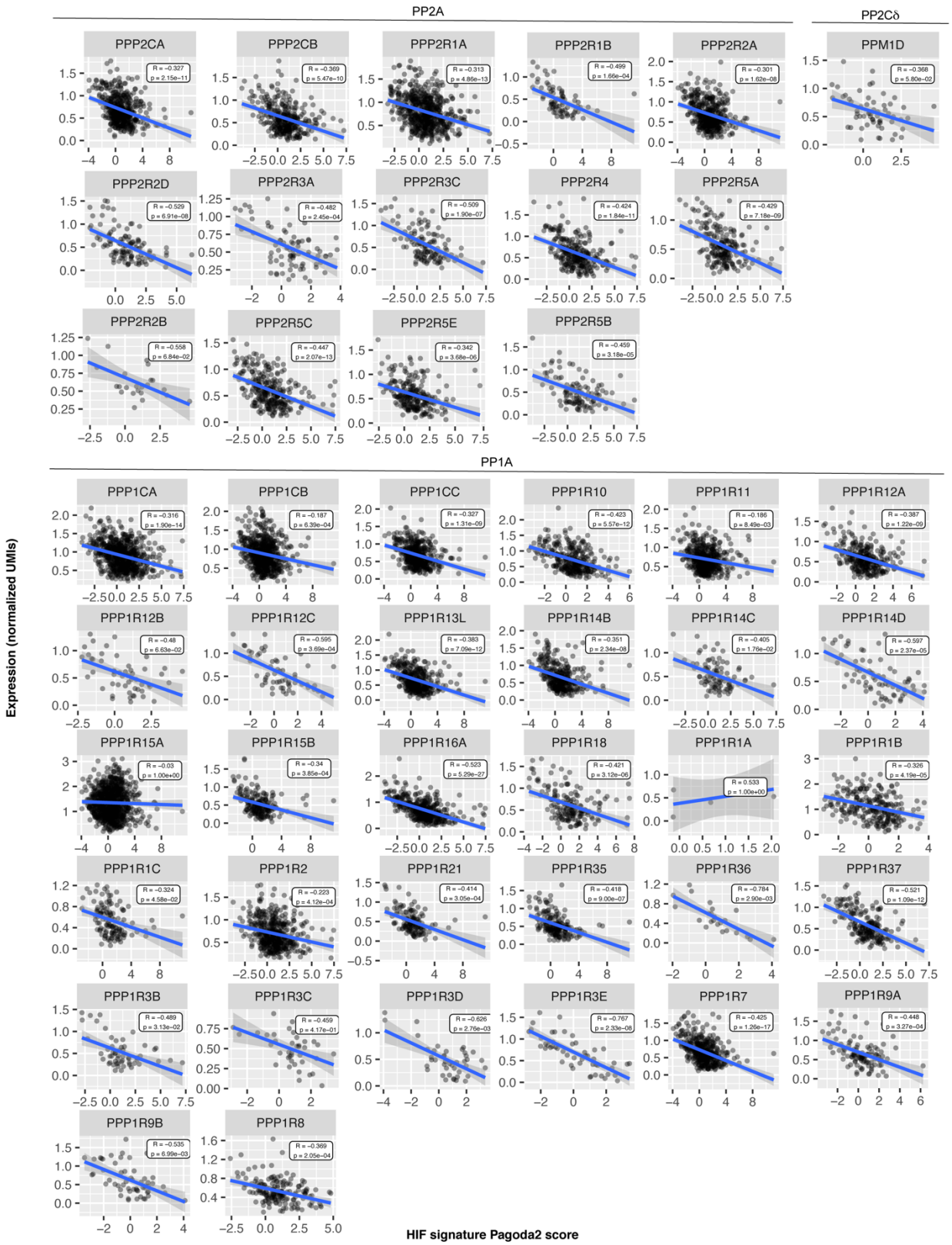

Supp Figure 2.S10 PP2A, PP2Cδ, and PP1A subunits are negatively correlated with HIF signature in PDAC patient tumors

Pearson correlation coefficients were computed between HIF signature Pagoda2 enrichment scores and the mRNA expression data of PP2A, PP2Cδ, and PP1A subunits using previously published scRNA-seq data (88). Only cells with non-zero expression of the indicated genes were retained in these analyses. The statistical significance of each correlation is indicated by *p*. (P.J.M.)

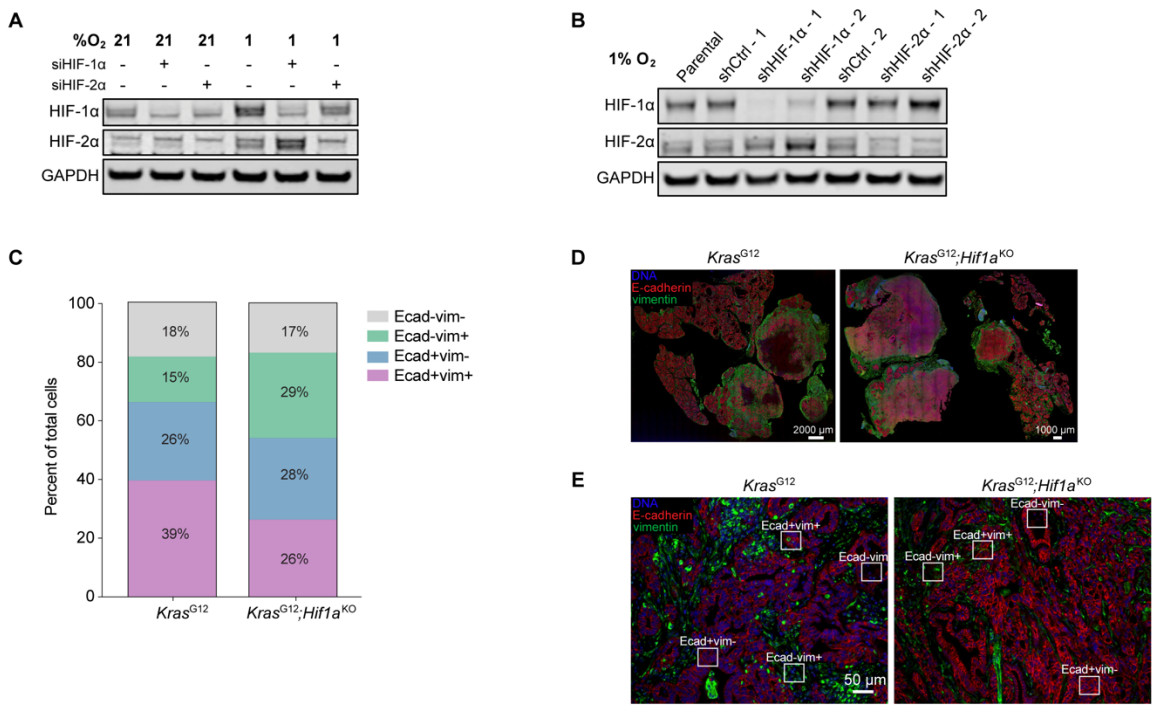

Supp Figure 2.S11 HIFs are involved in hypoxia-mediated EMT but are not the sole regulators
(A) HPAF-II cells were transfected with siRNA targeting HIF-1α or HIF-2α or control siRNA. 24 hr later, cells were switched to 1% O_2 for 4 hr and lysed. Lysates were analyzed by immunoblotting for the indicated proteins. **(B)** HPAF-II cells engineered with stable shRNA-mediated knockdown of HIF-1α and HIF-2α or control shRNAs were cultured in 1% O_2 for 4 hr and lysed. Lysates were analyzed by immunoblotting for the indicated proteins. **(C)** Sections of pancreas tumors from mice harboring tissue-specific *Kras*^{G12} and *Kras*^{G12};*Hif1a*^{KO} mutations (59) were stained for E-cadherin and vimentin and quantified by image analysis for the fraction of cells exhibiting the protein expression patterns indicated. *n* = 3, t test per protein combination revealed no significance between conditions for any protein combinations. **(D)** Representative images of *Kras*^{G12} and *Kras*^{G12};*Hif1a*^{KO} tumors are shown. **(E)** Representative images are shown with examples of Ecad-vim-, Ecad-vim+, Ecad+vim+, and Ecad+vim- cells.

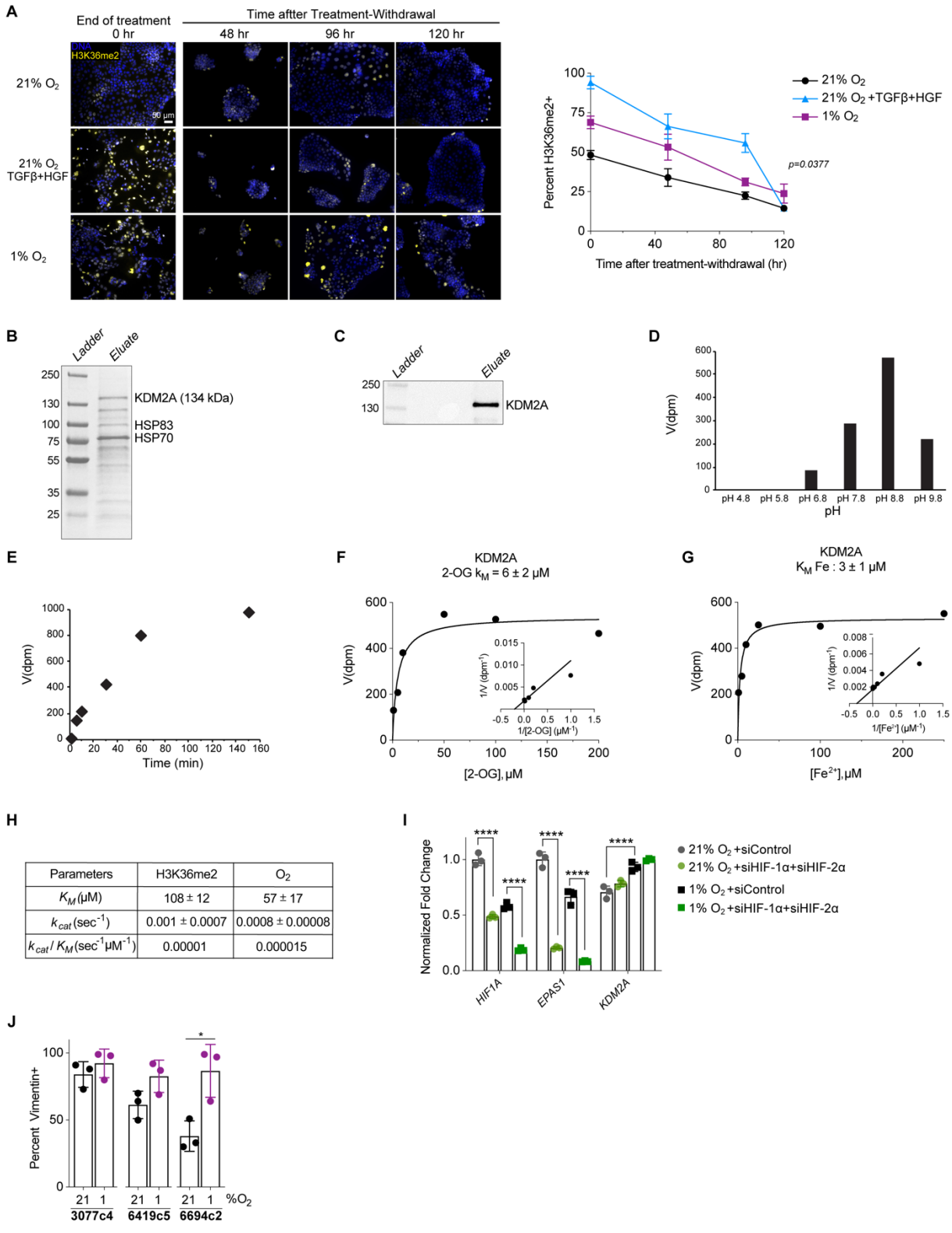

Parameters	H3K36me2	O_2
K_M (μM)	108 ± 12	57 ± 17
k_{cat} (sec^{-1})	0.001 ± 0.0007	0.0008 ± 0.00008
k_{cat} / K_M ($sec^{-1}\mu M^{-1}$)	0.00001	0.000015

Supp Figure 2.S12 H3K36 dimethylation and KDM2A activity are regulated by oxygen tension

(A) HPAF-II cells were cultured for 120 hr in 21% O_2 with or without 10 ng/mL TGFβ + 50 ng/mL HGF or in 1% O_2. Cells were then re-plated on coverslips and cultured in 21% O_2 without additional growth factors for up to 120 hr. Cells were fixed at the indicated times after re-plating. Cells were then stained with an H3K36me2 antibody, and immunofluorescence microscopy was performed with image analysis for percent H3K36me2-positive cells. $n = 3$, with data represented as mean ± s.e.m. $p = 0.0377$ for nonlinear regression with extra sum-of-squares F test comparing slopes. **(B)** SDS-PAGE with Coomassie blue staining was performed for recombinant FLAG-affinity purified sample containing KDM2A protein. (S.K.S.) **(C)** Immunoblotting was performed with anti-FLAG M2 antibody to confirm the protein was purified, with the middle lanes left empty. (S.K.S.) **(D)** Screening was performed to determine the optimum pH for measuring the kinetics of KDM2A-catalyzed reactions. pH 8.8 was selected based on this analysis. Where velocity (V) is reported as disintegration parts per minute (dpm). (S.K.S.) **(E)** The rate of KMD2A-catalyzed reaction was measured at multiple time points to determine the range over which linearity was maintained. A 30-min reaction time was selected based on this analysis. (S.K.S.) **(F-G)** Michaelis-Menten saturation curves with Lineweaver-Burk plots as insets are shown for the kinetic analysis of KDM2A-catalyzed reactions as a function of 2-oxoglutarate (2-OG) or Fe^{2+} concentration. Plots show data for one representative run, with solid lines corresponding to the model fits to the data shown. (S.K.S) **(H)** For Figure 2.7B,C, the fitted values of the Michaelis constant (K_M) and enzyme turnover rate (k_{cat}) are shown. Values are mean ± standard deviation for $n = 3$ independent biochemical measurements. (S.K.S.) **(I)** HPAF-II cells were transfected with siRNA targeting HIF-1α and HIF-2α or a control siRNA. 24 hr later, cells were moved to 1% O_2 or maintained at 21% O_2 for 120 hr. RNA was extracted, and qRT-PCR was performed for *HIF1A, EPAS1,* and *KDM2A*. *CASC3* was used as a control gene for normalization. $n = 3$, two-way ANOVA with Tukey's multiple comparisons test. **(J)** KPCY-derived cell lines 3077c4, 6419c5, and 6694c2 were treated as described in Figure 2.7D, and quantification of vimentin was performed. $n = 3$, one-way ANOVA. * $p < 0.05$, **** $p < 0.0001$

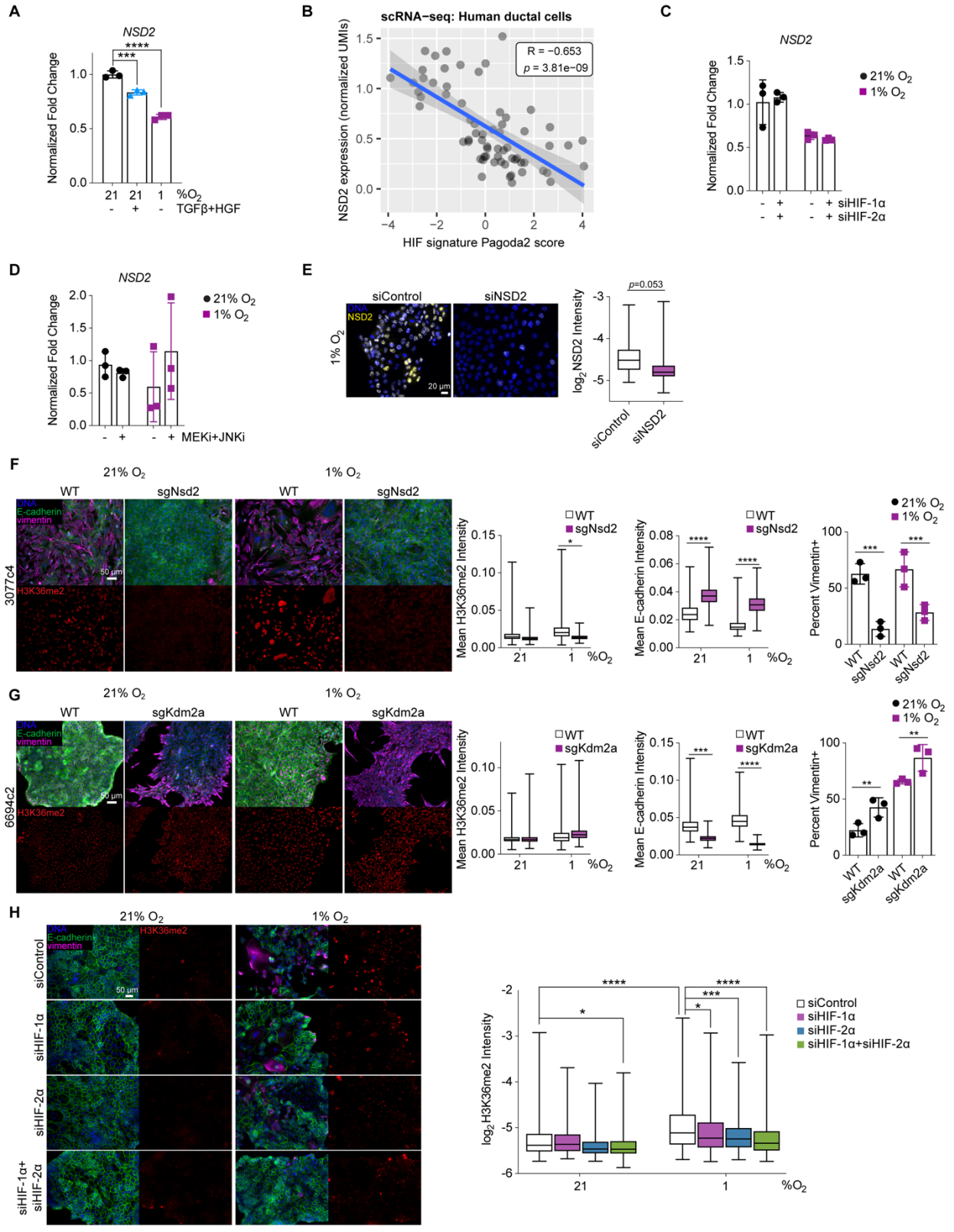

Supp Figure 2.S13 *NSD2* transcript expression is not HIF- nor MAPK-dependent, but Nsd2 or Kdm2a knockout impacts EMT in murine cells

(A) qRT-PCR was performed for *NSD2* mRNA from HPAF-II cells cultured in 21% O_2 with or without 10 ng/mL TGFβ + 50 ng/mL HGF or cultured in 1% O_2 for 120 hr. *CASC3* was used as a control gene for normalization. *n* = 3, one-way ANOVA with Tukey's multiple comparisons test. **(B)** The Pearson correlation coefficient was computed for the relationship between *NSD2* gene expression and HIF signature enrichment in human PDAC ductal cells using previously published scRNA-seq data (88). Only cells with non-zero expression of *NSD2* were retained in this analysis. (P.J.M.) **(C)** HPAF-II cells were transfected with siRNA targeting HIF-1α, HIF-2α, both HIFs, or control siRNA. 24 hr later, cells were moved to 1% O_2 or maintained at 21% O_2 for 120 hr. RNA was then extracted from cells, and qRT-PCR was performed for *NSD2*. *CASC3* was used as a control gene for normalization. *n* = 3. **(D)** qRT-PCR was performed for *NSD2* using RNA extracted from HPAF-II cells cultured for 120 hr in 21% or 1% O_2 with 1 μM CI-1040 (MEKi) and 10 μM SP600125 (JNKi) or DMSO. *CASC3* was used as a control gene for normalization. *n* = 3. **(E)** HPAF-II cells were transfected with siRNA targeting NSD2 or control siRNA. 24 hr later, cells were moved to 1% O_2 and maintained for 120 hr. Immunofluorescence microscopy was performed for nuclear NSD2. *n* = 3, mixed-effects analysis. **(F)** 3077c4 cells with *Nsd2* knockout, **(G)** 6694c2 cells with *Kdm2a* knockout, and their respective wild type counterparts were cultured for 120 hr in 21% or 1% O_2. Cells were then fixed and stained with antibodies for the indicated proteins, and immunofluorescence microscopy was performed with quantitative image analysis. *n* = 3, mixed effects analysis with Tukey's multiple comparison test. These KPCY-derived cell lines were described previously *(34).* **(H)** HPAF-II cells were transfected with siRNA targeting HIF-1α, HIF-2α, both HIFs, or control siRNA. 24 hr later, cells were moved to 1% O_2 or maintained at 21% O_2 for 120 hr. Cells were then fixed and stained with antibodies for the indicated proteins, and immunofluorescence microscopy with quantitative image analysis was performed. *n* = 3, one-way ANOVA with Tukey's multiple comparisons test. * $p < 0.05$, ** $p < 0.01$, *** $p < 0.001$, **** $p < 0.0001$

Supp Table 2.S1 Software and algorithms

RESOURCE	IDENTIFIER	SOURCE
CPTAC Data via LinkedOmics	http://www.linkedomics.org/data_download/CPTAC-PDAC/	
CPTAC Data via the Proteomic Data Commons	https://pdc.cancer.gov/pdc/browse/).	
TCGA PAAD RNA-seq Data	https://xenabrowser.net/datapages/?cohort=TCGA%20Pancreatic%20Cancer%20(PAAD)&removeHub=https%3A%2F%2Fxena.treehouse.gi.ucsc.edu%3A443	
R v4.1.2	https://www.r-project.org	R Development Core Team
Bioconductor v3.14	https://bioconductor.org/	(183)
clusterProfiler v4.0.5 (R package)	https://doi.org/doi:10.18129/B9.bioc.clusterProfiler	(106,184)
ComplexHeatmap v2.8.0 (R package)	https://doi.org/doi:10.18129/B9.bioc.ComplexHeatmap	(114)
ConsensusClusterPlus v1.56.0 (R package)	https://doi.org/doi:10.18129/B9.bioc.ConsensusClusterPlus	(101)
Cowplot v1.1.1 (R package)	https://wilkelab.org/cowplot/index.html	
DreamAI v0.1.0 (R package)	https://github.com/WangLab-MSSM/DreamAI	(87)
EPIC v1.1.5 (R package)	https://github.com/GfellerLab/EPIC	(95)
ggplot2 v3.3.5 (R package)	https://rdocumentation.org/packages/ggplot2/versions/3.3.5	(112)
ggstatsplot v0.9.0 (R package)	https://www.rdocumentation.org/packages/ggstatsplot/versions/0.9.0	(110)
ggupset v0.3.0 (R package)	https://github.com/const-ae/ggupset	
glmnet v4.1.-2 (R package)	https://rdocumentation.org/packages/glmnet/versions/4.1-2	(108)
GSVA v1.40.1 (R package)	https://doi.org/doi:10.18129/B9.bioc.GSVA	(102)
Hmisc v4.6-0 (R package)	https://github.com/harrelfe/Hmisc	Frank Harrell
immunedeconv v2.0.4 (R package)	https://github.com/icbi-lab/immunedeconv	(94)
msigdbr v7.4.1 (R package)	https://igordot.github.io/msigdbr/index.html	Igor Dolgalev
NMF v0.23.0 (R package)	https://www.rdocumentation.org/packages/NMF/versions/0.23.0	(96)
pagoda2 v1.0.6 (R package)	https://www.rdocumentation.org/packages/pagoda2/versions/1.0.6	(104)
survival v3.2-13 (R package)	https://rdocumentation.org/packages/survival/versions/3.2-13	Terry Therneau
Survminer v0.4.9 (R package)	https://rpkgs.datanovia.com/survminer/index.html	
tidyHeatmap v1.3.1 (R package)	https://rdocumentation.org/packages/tidyHeatmap/versions/1.3.1	(113)

Supp Table 2.S2 qRT-PCR Primers

Target		Sequence (5' → 3')
CASC3	Forward	ACCTCGGAAAGGGCTCTTCTT
	Reverse	CGACCCTCATCCTTCCATAGC
CDH1	Forward	CATCAGGCCTCCGTTTCTG
	Reverse	GGAGTTGGGAAATGTGAGCA
VIM	Forward	TCTCTGAGGCTGCCAACCG
	Reverse	CGAAGGTGACGAGCCATTTCC
SNAI1	Forward	CTTCCAGCAGCCCTACGAC
	Reverse	CGGTGGGGTTGAGGATCT
TWIST1	Forward	CGGGAGTCCGCAGTCTTA
	Reverse	TGAATCTTGCTCAGCTTGTC
HIF1A	Forward	TGCTCATCAGTTGCCACTTC
	Reverse	TCCTCACACGCAAATAGCTG
EPAS1	Forward	GCGCTAGACTCCGAGAACAT
	Reverse	TGGCCACTTACTACCTGACCCTT
PGK1	Forward	AAGTCGGTAGTCCTTATGAGC
	Reverse	CACATGAAAGCGGAGGTTCT
SLC2A1	Forward	AGGTGATCGAGGAGTTCTAC
	Reverse	TCAAAGGACTTGCCCAGTTT
PPP1CA	Forward	GCTGCTGGCCTATAAGATCAA
	Reverse	GTCTCTTGCACTCATCGTAGAA
PPP2R2B	Forward	TGCAGCTTACTTTCTTCTGTCT
	Reverse	GTAGCCTTCTGGCCTCTTATC
PPM1D	Forward	CCTGTTAGAAGGAGCACAGTTAT
	Reverse	GTTCAGGTGACACCACAAATTC
KDM2A	Forward	CCGATTGTGTCAGGAGCCAG
	Reverse	CACAGGACTGCTTCATGCGTC
NSD2	Forward	CCCACCATACAAGCACAT
	Reverse	TCAGACACTCCGAATCAAA

CHAPTER 3: SINGLE-CELL RNA-SEQUENCING REVEALS MICROENVIRONMENTAL CONTEXT-SPECIFIC ROUTES FOR EPITHELIAL-MESENCHYMAL TRANSITION IN PANCREAS CANCER CELLS[2]

3.1 ABSTRACT

In the PDAC tumor microenvironment, multiple factors initiate the epithelial-mesenchymal transition (EMT) that occurs heterogeneously among transformed ductal cells, but it is unclear if different drivers promote EMT through common or distinct signaling pathways. Here, we use single-cell RNA sequencing (scRNA-seq) to identify the transcriptional basis for EMT in pancreas cancer cells in response to hypoxia or EMT-inducing growth factors. Using clustering and gene set enrichment analysis, we find EMT gene expression patterns that are unique to the hypoxia or growth factor conditions or that are common between them. Among the inferences from the analysis, we find that the FAT1 cell adhesion protein is enriched in epithelial cells and suppresses EMT. Further, the receptor tyrosine kinase AXL is preferentially expressed in hypoxic mesenchymal cells in a manner correlating with YAP nuclear localization, which is suppressed by FAT1 expression. AXL inhibition prevents EMT in response to hypoxia but not growth factors. Relationships between FAT1 or AXL expression with EMT were confirmed through analysis of patient tumor scRNA-seq data. Further exploration of inferences from this unique dataset will reveal additional microenvironment context-specific signaling pathways for EMT that may represent novel drug targets for PDAC combination therapies.

[2] A version of Chapter 3 will be submitted to a peer-reviewed journal as, Brown BA and Lazzara MJ, Single-cell RNA sequencing reveals microenvironment context-specific routes for epithelial-mesenchymal transition in pancreas cancer cells

3.2 INTRODUCTION

In pancreatic ductal adenocarcinoma (PDAC), an especially aggressive tumor subtype exists that is enriched in mesenchymal characteristics. The mesenchymal phenotype is associated with decreased survival and increased resistance to therapy relative to other subtypes (9-11,185) and correlates with gene signatures for ductal cell epithelial-mesenchymal transition (EMT) (185). EMT occurs in response to varied initiating factors in the PDAC tumor microenvironment, including receptor ligands such as transforming growth factor beta (TGFβ), hepatocyte growth factor (HGF), and epidermal growth factor (24,25,32), and the low oxygen tension (hypoxia) resulting from PDAC tumor hypovascularity (79,80,84,185). It is unclear if different modes of EMT induction use distinct or common signaling pathways.

EMT occurs heterogeneously in PDAC tumors and cell populations (13,17,186). Even in cell culture conditions, where spatial variation in extrinsic EMT-driving factors is minimal, phenotypic heterogeneity is observed, and the degree of heterogeneity depends on cell background and mode of EMT induction (185). Heterogeneity is also affected by the durability of the transition, which is greater in response to hypoxia than growth factors (185). EMT heterogeneity endows differential chemoresistance to a subset of cells within tumors (186) and, as with any form of cell-to-cell heterogeneity, creates challenges for understanding the signaling or transcriptional processes that govern the phenotype (187). Prior work provides clues about the basis for EMT heterogeneity in different cancer cell settings, although generally without investigating fundamentally different classes of EMT-inducing conditions in parallel. In a colon cancer cell line subjected to single-cell RNA sequencing (scRNA-seq), variability in Wnt pathway activity due to intrinsic heterogeneity in the expression of key signaling network nodes correlates with the baseline mesenchymal state (77). Further, ATAC-seq revealed enrichment of the transcription factor RUNX2 in Wnt-high cells, which was confirmed via *in vivo* overexpression of RUNX2 promoting metastasis and in clinical samples, RUNX2 correlated to poor survival (77). In

MCF10A breast cancer cells treated with TGFβ, scRNA-seq demonstrates that some cells activate different EMT signaling pathways in series while others activate them in parallel (with Notch playing a particularly important role), leading to variability among cells in the rate of EMT progression and contributing to apparent phenotypic heterogeneity in a snapshot view (30). In lung, prostate, breast, and ovarian cancer cells treated with a diverse set of growth factors including TGFβ, EGF, and TNFα, scRNA-seq reveals minimal overlap of differentially expressed genes despite some common changes in the expression of genes associated with EMT (e.g., *EPCAM, VIM*) or specific EMT-regulating signaling pathways (e.g., *JUN, EGFR*), suggesting distinct transcriptional and signaling regulatory programs even among ligands for receptor kinases (29).

Here, we performed scRNA-seq on a baseline epithelial pancreas cancer cell line that was treated with a combination of TGFβ and HGF or cultured under hypoxic conditions. Both conditions produced a heterogeneous EMT among cells, enabling the identification of regulatory transcriptional processes that lead to or restrain EMT in a context-specific manner using clustering and gene set enrichment analysis. Among the inferences from the analysis, we found that expression of the FAT1 cell adhesion protein and Hippo pathway activity, which is regulated by FAT1 (188) and suppresses YAP nuclear localization (189), are generally enriched in epithelial cells. We further identified the receptor tyrosine kinase AXL, which is transcriptionally regulated by YAP (190) and can drive EMT in other cancers (191,192), as a hypoxia-specific driver of EMT in pancreas cancer cells. This and other inferences from our analysis were confirmed in an analysis of PDAC patient tumors. In addition to these experimentally validated predictions, the dataset gathered here provides a wealth of additional inferences that can be pursued to understand the context-specific basis for EMT induction in a pancreas cancer cell background.

3.3 METHODS

Cell culture

HPAF-II cells (Carl June, University of Pennsylvania) were cultured in RPMI with 10% fetal bovine serum (FBS), 1 mM L-glutamine, 100 units/mL penicillin, and 100 µg/mL streptomycin. The Genetic Resources Core Facility at the John Hopkins University School of Medicine authenticated the HPAF-II cells by performing short tandem repeat profiling via GenePrint 10 (Promega) and comparing to the ATCC database. HPAF-II cells were assessed for mycoplasma using the MycoAlert PLUS Detection Kit (Lonza). Cells were cultured in a Thermo Scientific Forma Steri-Cycle i160 incubator at 5% CO_2 and 37ºC for normal culture. For hypoxic culture at 1% O_2, cells were grown in a Tri-Gas version of the same incubator, which allows for N_2 to displace O_2. The lower limit of the incubator is 1%. Following plating, cells cultured under normal 21% O_2 conditions for 16 hr then either maintained in 21% or transferred to the tri-gas incubator.

Growth factors and inhibitors

Recombinant human TGFβ and HGF (Peprotech) were used at 10 ng/mL and 50 ng/mL, respectively. During treatment, complete medium with growth factors was replenished every 48 hr. The AXL inhibitor dubermatinib (MedChemExpress) was used at 40 nM, MEK inhibitor CI-1040 (LC Laboratories) was used at 1 µM, and JNK inhibitor SP600125 (LC Laboratories) was used at 10 µM. Stocks of all inhibitors were prepared in DMSO.

Antibodies

Antibodies against vimentin (Santa Cruz Biotechnology, sc-373717), E-cadherin (clone ECCD2, Invitrogen, 13-1900), FAT1 (BiCell, 50501), AXL (Cell Signaling Technology, #8661), YAP (Santa Cruz Biotechnology, sc-101199), and GAPDH (Santa Cruz Biotechnology, sc-32233) were used. For a nuclear stain, Hoechst 33342 (Invitrogen, H1399) was used.

Coverslip immunofluorescence

Cells were cultured on 18-mm glass coverslips in 6-well plates. At the conclusion of an experiment, cells were fixed with 4% paraformaldehyde in PBS for 20 min and then permeabilized with 0.25% Triton-X 100 in PBS for 5 min. Primary antibodies were added to coverslips in a humidified chamber overnight at 4°C. Coverslips were washed five times with 0.1% Tween 20 in PBS, then incubated for 1 hr at 37°C in a humidified chamber with Alexa Fluor secondary antibodies and Hoechst nuclear stain. All antibodies were diluted in Intercept Blocking Buffer (Licor, 927-60001). Following the staining and washing steps, coverslips were mounted on glass slides with ProLong Gold Antifade Mountant.

Fluorescence microscopy and automated image analysis

Coverslips were imaged on a Zeiss Axiovert Observer.Z1 fluorescence microscope, using a 20 or 63× objective and ZEN image processing software to produce .czi files. Within a particular experiment, across replicates and conditions, imaging was performed using the same exposure times and image settings. Four frames were imaged at random for each biological replicate, yielding at least 1000 cells per replicate. For image analysis, CellProfiler v3.1.9 (Broad Institute) was used to quantify signal intensity and localization (121-123). Discrete cells were identified based on the nuclear stain as the primary object for the analysis pipeline. For percent-positive measurements, a threshold was set based on a negative control consisting of a sample stained with a secondary antibody only. All cells were subject to the same threshold, and a percentage was calculated based on the number of cells with signal above background relative to the total cell number. For intensity measurements, the mean intensity per object was measured. For nuclear measurements, the nuclear stain was used to restrict the signal to the nuclear domain.

Western blotting

Cells were lysed using a standard cell extraction buffer (Invitrogen, FNN0011) supplemented with protease and phosphatase inhibitors (Sigma-Aldrich, P8340, P5726, P0044). Crude lysates were centrifuged at 14,000 rpm for 10 min at 4°C, and supernatants were retained as clarified lysates. Total protein concentration was measured with a micro-bicinchoninic acid (BCA) assay (Pierce). Equal protein amounts were mixed with 10× NuPAGE reducing agent, 4X LDS sample buffer and MilliQ water. Samples were heated for 10 min at 100°C and loaded onto a 1.5 mm NuPAGE gradient (4-12%) gel (Invitrogen, NP0336BOX). After electrophoresis, gels were transferred to a 0.2 µm nitrocellulose membrane using the TransBlot Turbo Transfer System (BioRad). Membranes were blocked with Intercept Blocking Buffer (IBB; Licor, 927-60001) for 1 hr on an orbital shaker. Primary antibodies were diluted at 1:1000 in IBB, then incubated with membranes overnight at 4°C. Membranes were washed with 0.1% Tween-20 in PBS by shaking three times for 5 min each. Secondary antibodies were diluted 1:10,000 in IBB and incubated with shaking for 2 hr at room temperature. Membranes were washed as previously described with 0.1% Tween-20 in PBS. Membranes were imaged on a LiCor Odyssey. Image Studio software was used for band densitometry.

Single-cell RNA sequencing

scRNA-seq was performed by the UVA Genome Analysis and Technology Core. HPAF-II cells were cultured in 6-well plates with three biological replicates per condition, with approximately one million cells per replicate at the conclusion of the experiment. For sequencing, three biological replicates were pooled together prior to preparing the samples. Cells were prepared using the 10× Genomics® Sample Preparation Demonstrated Protocol, *Single Cell suspensions from Cultured Cell Lines for Single Cell RNA Sequencing* (Manual CG00054 Rev B). After confirming cell viability and single cells, Next Generation Sequencing (NGS) Library

preparation was performed for 3' RNA gene expression. For quality control of the library, a Qubit Fluorometer (Thermo Fisher), TapeStation D5000 HS system (Agilent), and MiSeq – 300 cycle nano (Illumina) were used. Sequencing was performed using Illumina NextSeq™2000 with P2 – 100 cycle v3 to allow for 25,000 reads per cell.

Gene sets and signatures

The pan-cancer EMT signature (89) was used as the primary feature set for clustering based on EMT markers. The HIF target signature was used as previously published (90). Hallmark gene sets were obtained from the Molecular Signatures Database, including Hallmark Hypoxia and Hallmark EMT (91). Gene sets from the Kyoto Encyclopedia of Genes and Genomes (KEGG) (92,93) were accessed within R using the *clusterProfiler* package.

Pre-processing of scRNAseq data

10× genomics data was aligned to the human genome and filtered to contain only cells with barcodes using CellRanger by the UVA Bioinformatics Core. This created a filtered dataset of 1910 (normoxic), 2493 (TGFβ+HGF), and 2441 (hypoxic) cells. Software and R packages used are cited in **Supp Table 3.S1**. The code used to analyze the data can be accessed here: https://github.com/lazzaralab/Brown-et-al_PDAC-scRNAseq. The *Seurat* R package was used to filter, normalize, scale, and cluster the data. The data was filtered to remove low-quality cells and doublets, by filtering out cells that express too few or too many genes and excessive mitochondrial gene counts. The R package *scRNABatchQC* (193) was used to determine the threshold for these metrics. Cells that had greater than 1882 genes, fewer than 8500 genes, and less than 15 percent mitochondrial genes were retained for analysis. After quality control steps, a dataset of 1703 (normoxic), 2178 (TGFβ+HGF), and 2148 (hypoxic) cells was available for analysis. Using *Seurat*,

the data was normalized by log-transforming and scaled for the mean expression to be 0 and the variance across cells to be 1.

Principal components analysis and clustering

To reduce the dimensionality of the data, we performed principal component analysis (PCA) for either all features or a subset of features (i.e., pcEMT gene set, HIF-target gene set, or Hallmark Hypoxia gene set, as noted in the results). For analysis including all genes, the number of principal components (PCs) to include was determined by calculating 1) the point where the PCs only contribute 5% of standard deviation and the PCs cumulatively contribute 90% of the standard deviation, and 2) the percent change in variation between consecutive PCs is less than 0.1%, and using the lower value of 1) and 2) for the number of PCs to include in downstream analysis (as adapted from the Harvard Chan Bioinformatics Core). The *Seurat* package was used to employ k-nearest neighbor (kNN) clustering on a PCA projection of the data using the optimal dimensionality determined as described above. For analysis including all genes, the optimal resolution for the number of clusters was determined by calculating the silhouette score (as adapted from Roman Hillje), and the resolution was constrained when restricting the data to two clusters for comparison of E and M. Using *Seurat*, a UMAP projection was employed to visualize the clusters created from kNN clustering.

Gene expression and gene set enrichment

The *Seurat* package was used to calculate and visualize differential gene expression between the clusters, to visualize gene expression by violin plots, and for scatter plots. The R package *Escape* was used for gene set enrichment analysis (GSEA) calculations for individual cells. Per cell enrichment values were calculated using ssGSEA, as previously described (194). Significant differences between clusters were determined by performing ANOVA. Enrichment

plots for the Response to Hypoxia were performed by calculating a mean rank order for a gene set using ssGSEA across each condition. The R package *UCell* was used for scoring gene signatures based on the Mann-Whitney U statistic (195). Gene set variation analysis (GSVA) was utilized to determine the enrichment of Kyoto Encyclopedia of Genes and Genomes (KEGG) signaling pathways using the R packages *GSVA* and *limma* for statistical testing. GSVA scores were calculated and fit to a linear model, followed by empirical Bayes statistics for differential enrichment analysis, as previously described [as adapted from Roman Hillje (102)]. The log-odds that the gene set is differentially enriched was displayed.

siRNA-mediated knockdowns

Silencer^{TM} Select siRNA against FAT1 s5033 (Thermo Fisher, 4392420) and *Silencer*^{TM} Select negative control siRNA (Thermo Fisher, 4390843) were used with Lipofectamine RNAiMAX (Thermo Fisher) per manufacturer recommendations.

Quantitative reverse transcription PCR (qRT-PCR)

RNA was extracted using the RNeasy Kit (Qiagen, #74104) and reverse transcribed using High-Capacity cDNA Reverse Transcription Kit (Applied Biosciences, #4368814). qRT-PCR was performed using PowerUp SYBR Green (Applied Biosciences, #A25741) per manufacturer protocol using a QuantStudio3 system (Applied Biosystems). Measurements were analyzed with the ddCt method (124). Data are displayed as a normalized fold changes, using *CASC3* as a housekeeping gene. Primer sequences are provided in **Supp Table 3.S2**.

Statistical analyses for experimental studies

Prism 9 for macOS was used for all experimental statistical analyses. Figure captions include details on the analyses conducted. For two-way ANOVA, the post hoc test was chosen

based on the comparison made, with Tukey's multiple comparisons used when considering all conditions and Sidak's multiple comparisons used when considering specific comparisons within a larger dataset.

3.4 RESULTS

EMT occurs heterogeneously in response to growth factors or hypoxia.

HPAF-II human pancreas cancer cells were driven to undergo EMT by treatment with exogeneous TGFβ+HGF or culture in 1% O_2. The combination of growth factors for receptors that independently promote EMT was used to activate downstream effectors broadly and thereby increase the odds that regulatory processes unique to growth factors or hypoxia are identified. HPAF-II cells were used because they are baseline epithelial and an established model for well-differentiated PDAC (196). As we have observed previously (185), the extent of mesenchymal transition differed between growth factors and hypoxia as EMT drivers, with hypoxia promoting vimentin expression in only a minority of cells and growth factors causing most cells to express abundant vimentin **(Figure 3.1A)**. Thus, both conditions produced a heterogeneous EMT among cells but to different degrees. These observations motivate the possibility that different molecular pathways are responsible for EMT in response to the different drivers and prompt exploration of the basis for heterogeneity of EMT for each condition.

Given that EMT is highly regulated by transcription factors (e.g., Slug, ZEB1) and the feasibility of single-cell transcriptomics, we utilized single-cell RNA-sequencing (scRNA-seq) to probe the transcriptional basis for EMT heterogeneity. We performed scRNA-seq on HPAF-II cells cultured in 21% O_2 with or without TGFβ+HGF or cultured in 1% O_2. As expected, cells cultured in 1% O_2 were enriched in hypoxia-inducible factor (HIF) target genes (90) **(Supp Figure 3.S1A,B)**, confirming that a hypoxic response occurred. Given the inherent technical noise in expression for any single gene in the data set, we performed principal component analysis (PCA) to allow for a group of genes to be used for subsequent clustering. The number of principal components (PC) for PCA projection was calculated by computing the variance in the dataset explained as a function of PC and using 0.1% as a cutoff **(Supp Figure 3.S2A)**. Using a projection into 20 PCs, the aggregated data for all three conditions was clustered using k-nearest neighbors

(kNN). The optimal number of clusters was determined by computing silhouette scores per cell for up to 10 clusters. Three clusters provided the highest mean silhouette score **(Supp Figure 3.S2B)**. Clustered cells were then visualized in a UMAP projection **(Figure 3.1B),** and clusters corresponded well with treatment conditions **(Figure 3.1C)**. To investigate the basis for cluster separation, we identified the top 10 differentially expressed genes (DEGs) by cluster **(Figure 3.1D)**. Of note, DEGs for cluster 0 included the mesenchymal-associated genes *VIM* and *LGALS1*. For Cluster 1, DEGs of note included the hypoxia-associated genes *PGK1* and *SLC2A1*. For Cluster 2, DEGs of note included *MKI67* and *TUBA1B*, which play important roles in proliferation (a process most characteristic of the epithelial state). To identify the top differentially regulated cell processes among clusters, enrichment scores were calculated on a per cell basis for the 50 Hallmark Gene Sets **(Figure 3.1E)**. The top three gene sets that were significantly differentially enriched among the three clusters include Hallmark Hypoxia (most expressed in Cluster 1), Hallmark E2F Targets (mostly expressed in Cluster 2), and Hallmark EMT (most expressed in Clusters 0 and 1). Thus, in addition to hypoxic response and proliferation, EMT represents one of the most significant overall differences among clusters, despite inter- and intra-condition differences in EMT induction.

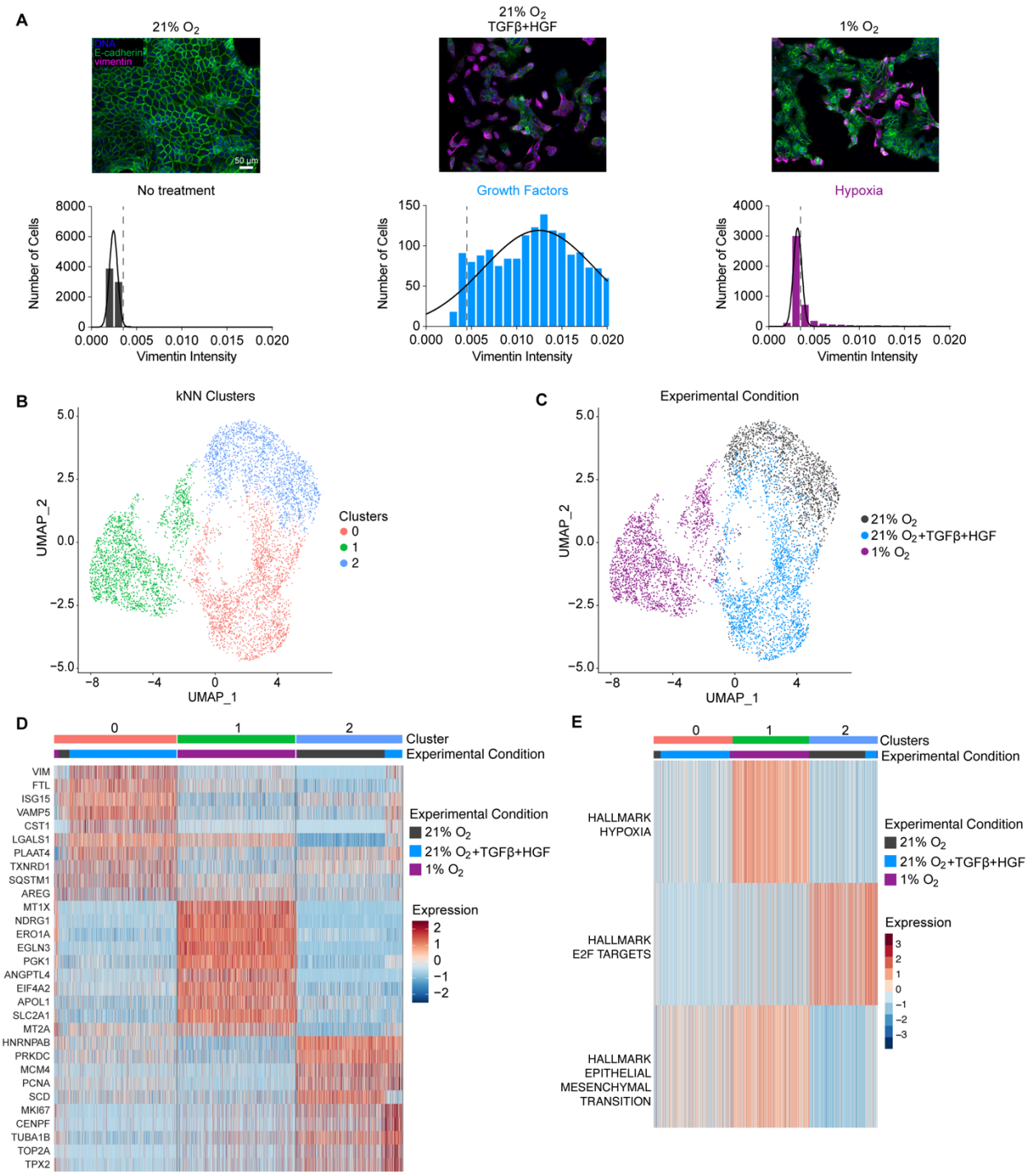

Figure 3.1 EMT is heterogenous across and within each treatment condition

(A) HPAF-II cells were cultured in 21% O_2 with or without 10 ng/mL TGFβ and 50 ng/mL HGF or cultured in 1% O_2 for 120 hr. Immunofluorescence microscopy was performed for the indicated proteins. Histograms show vimentin intensities across all biological replicates. *n* = 3. The dotted vertical line denotes the threshold for the intensity vimentin positivity. **(B)** UMAP projection of k-Nearest Neighbor (kNN) clustering performed on all genes for the aggregated scRNA-seq data from HPAF-II cells as treated in (A). **(C)** For the same UMAP projection shown in (B), cells are color-coded based on experimental condition. **(D)** The top 10 differentially expressed genes per cluster with respect to the other two clusters were calculated. **(E)** Gene

set enrichment analysis was performed per cell for the 50 Hallmark gene sets. Displayed are the top three significantly differentially enriched gene sets among the three clusters as calculated by ANOVA.

Differential gene expression between epithelial and mesenchymal cells reveals the governing signaling pathways.

Given the relevance of EMT gene regulation in explaining variance among conditions, we next identified cells directly as epithelial or mesenchymal to probe the transcriptional differences between them. The full data set was re-clustered using the previously described approach but using features from a patient-derived pan-cancer EMT (pcEMT) signature (89), which contains 77 genes associated with epithelial or mesenchymal cell states and specifying two clusters **(Figure 3.2A)**. This created one cluster enriched in epithelial (E) genes and one enriched in mesenchymal (M) genes **(Figure 3.2B)**. Cells with no treatment (21% O_2) overlapped primarily with the E cluster, while TGFβ+HGF-treated cells overlapped primarily with the M cluster; cells cultured at 1% O_2 were roughly evenly split between the E and M clusters **(Figure 3.2C)**. Differences between the clusters are also apparent in UMAP projections color-coded by the expression of the EMT markers *CDH1* (E-cadherin) and *VIM* (vimentin) **(Figure 3.2D)**. As expected, the top 10 differentially expressed genes for the two clusters included cell-adhesion markers (i.e., *CDH17*, *CEACAM5*) and mesenchymal genes (i.e., *VIM* and *LGALS1*) **(Figure 3.2E)**.

To identify regulators of EMT across the three experimental conditions, gene set variation analysis (GSVA) enrichment scores were calculated for Kyoto Encyclopedia of Genes and Genomes (KEGG) signaling pathways for a comparison of the E and M clusters. Hippo signaling was the most differentially enriched pathway **(Figure 3.2F)** and was preferentially active in the E cluster **(Figure 3.2G)**. This is consistent with findings that Hippo activity promotes YAP/TAZ degradation in epithelial cells and that Hippo suppression promotes YAP/TAZ nuclear localization and expression of EMT transcription factors (197).

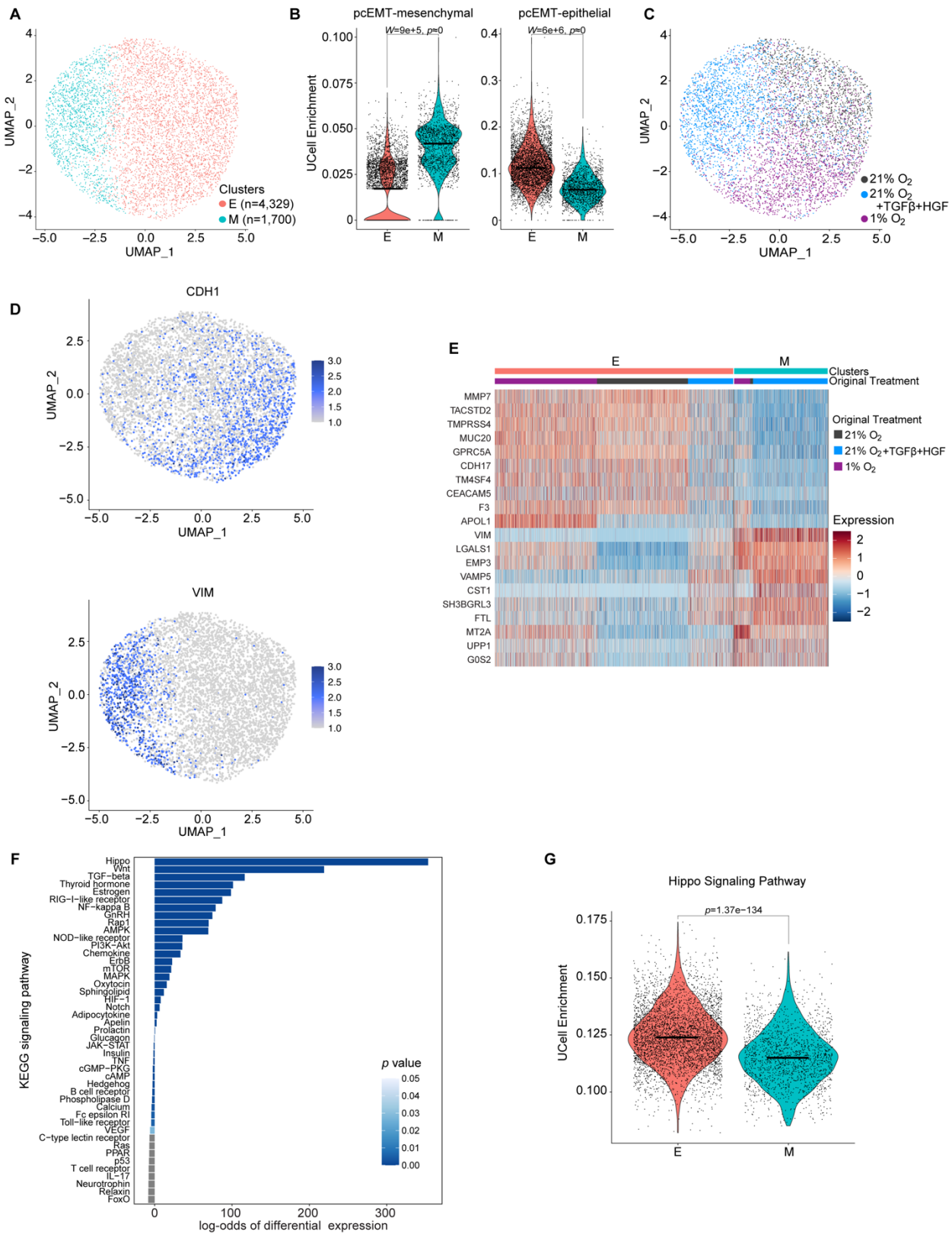

Figure 3.2 Cells were clustered on EMT-gene signature into epithelial and mesenchymal clusters to determine that the Hippo pathway is enriched in epithelial cells

(A) Aggregated scRNA-seq data from HPAF-II cells cultured in 21% O_2 with or without 10 ng/mL TGFβ and 50 ng/mL HGF or cultured in 1% O_2 were subjected to k-nearest neighbor clustering on the pcEMT gene signature into two clusters and UMAP projections were created. **(B)** Scores for gene enrichment were calculated with UCell for the epithelial and mesenchymal portions of the pcEMT gene signature, identifying one cluster enriched in epithelial genes and one enriched in mesenchymal genes. A Mann-Whitney test was performed, and the bar denotes the median. **(C)** The experimental conditions were mapped to the UMAP projection shown in (A). **(D)** Expression of the epithelial gene *CDH1* and the mesenchymal gene *VIM* were displayed on the UMAP projection from (A). **(E)** The top 10 differentially expressed genes per cluster were calculated. **(F)** Gene set variation analysis for KEGG signaling pathways was performed comparing the epithelial (E) and mesenchymal (M) clusters of the aggregated data set. **(G)** Scores for enrichment of the KEGG Hippo Signaling Pathway were calculated for the E and M clusters. A Mann-Whitney test was performed, and the bar denotes the median.

Growth factors and hypoxia drive unique and shared differentially expressed genes between epithelial and mesenchymal cells.

To identify common and distinct transcript features associated with EMT in response to growth factors and hypoxia, cells were separated by treatment condition prior to clustering based on the pcEMT gene signature **(Figure 3.3A-C)**. Surveying pcEMT genes by enrichment scores for epithelial and mesenchymal genes **(Figure 3.3D)** or using a heatmap **(Figure 3.3E)**, demonstrates that the clusters identified for each treatment condition are enriched in E or M genes. The proportion of cells falling into E and M clusters differed by treatment condition, as expected based on the immunofluorescence results in Figure 3.1A. M clusters from growth factor and hypoxic conditions were enriched in mesenchymal genes, and growth factor-treated mesenchymal cells had an overall lower expression of epithelial genes compared to hypoxic mesenchymal cells. Based on the heatmap, some genes are consistently enriched across E or M clusters regardless of treatment (e.g., *VIM* in M clusters). However, some genes are only enriched in E or M clusters for a particular condition (e.g., *AXL* in hypoxic M cells). When cells are projected in a two-PC space based on the pcEMT gene set, there is clear overlap of the three epithelial clusters but good separation for the mesenchymal clusters **(Figure 3.3F)**, indicating that different modes of EMT lead to differential enrichment of EMT-associated genes.

To understand the regulation of EMT in the three settings, the top 50 differentially expressed genes between the E and M clusters were identified for the three experimental conditions **(Supp Figure 3.S3A-C)**. Of the top 50 genes per treatment, three were shared among each of the E clusters (*ERBB3*, *GPX2*, *MMP7*), and three were shared among each of the M clusters (*VIM*, *LGALS1*, *EMP3*) **(Figure 3.3G,H)**. Further, among the top 50 differentially expressed genes, there were some genes common between just two of the E clusters (e.g., *FAT1* and *CDH17* for 21% O_2 and growth factor-treated) or M clusters (e.g., *AXL* and *ITGA5* for 21% and 1% O_2), as well as many that were unique to a treatment condition (e.g., *LOXL2* for 1% O_2 M cluster). However, it is important to note that this analysis identified the top differentially expressed genes between the E and M clusters per treatment, meaning that genes appearing as unique or among just two clusters could still be altered in other conditions but not among the top 50 differentially expressed genes.

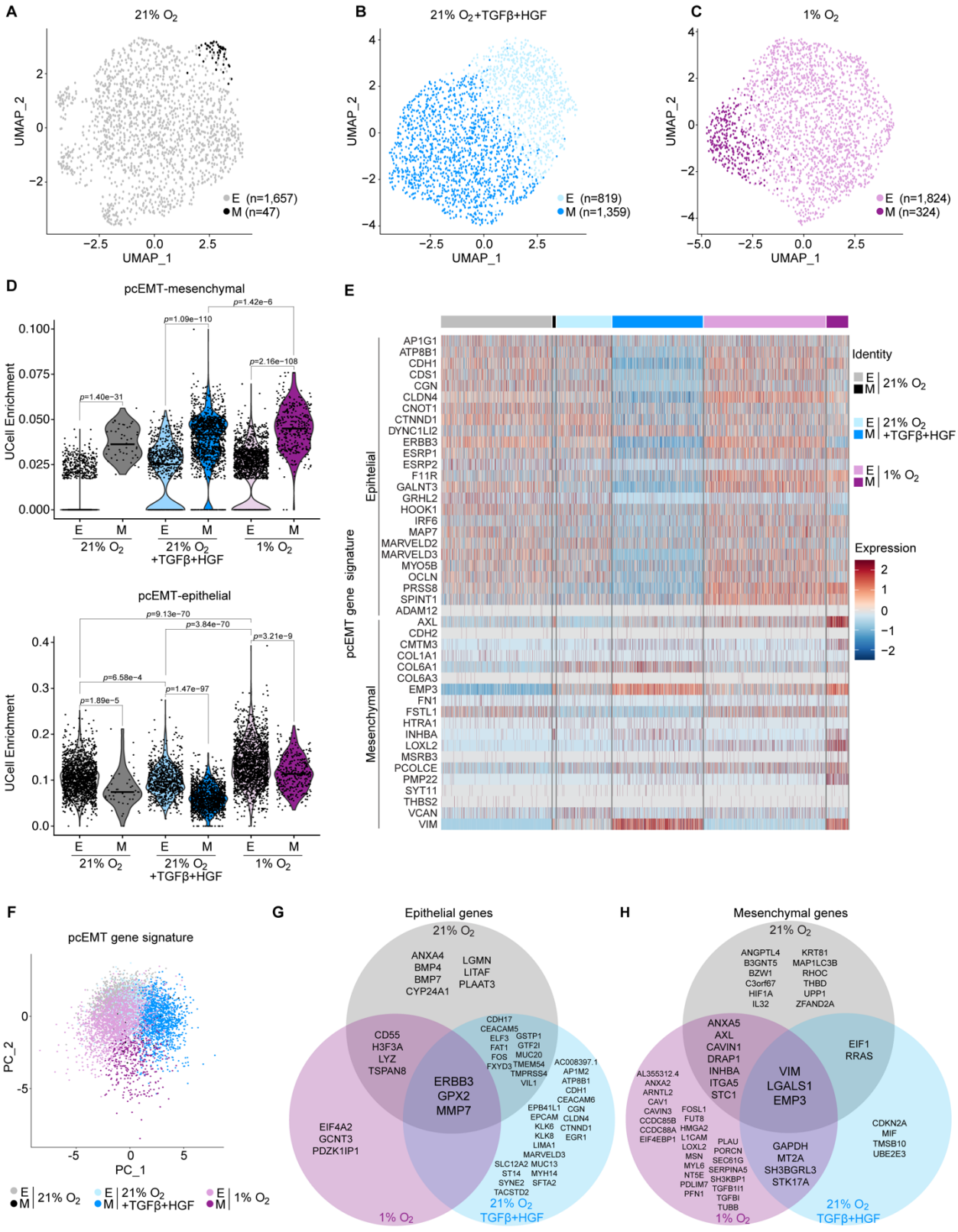

Figure 3.3 Growth factor- and hypoxia-driven EMT promote both unique and shared differential gene expression patterns

(A-C) HPAF-II cells cultured in **(A)** 21% O_2, **(B)** 21% O_2 with 10 ng/mL TGFβ and 50 ng/mL HGF, or **(C)** 1% O_2 were subjected to k-nearest neighbor clustering on the pcEMT gene signature into two clusters and UMAP projections were created. **(D)** Scores for gene enrichment were calculated with UCell for the epithelial and mesenchymal portions of the pcEMT gene signature, identifying one clustered enriched in epithelial genes (E) and one enriched in mesenchymal genes (M). A Kruskal-Wallis test with Dunn pairwise comparisons was performed, and the bar denotes the median. **(E)** The heatmap displays the expression of the pcEMT genes for each of the E and M clusters by treatment condition. Only genes expressed in more than 50 cells are displayed. **(F)** A two-component PCA based on the pcEMT gene set features is shown for the aggregated data. Cells are color-coded by treatment condition and E/M identify based on clustering performed in panels (A)-(C). **(G,H)** The top 50 differentially expressed genes were calculated per condition between the E and M clusters, as shown in Supp Figure 3.S3. Venn diagrams display the unique and shared **(G)** epithelial and **(H)** mesenchymal genes out of those top 50 differentially expressed per condition.

FAT1 is enriched in epithelial cells.

After surveying the results of Figure 3.3 and the literature, we sought to investigate and validate the functions of gene products that could be hypothesized to maintain the epithelial state or promote EMT. *FAT1* enrichment was common to the 21% O_2 and growth factor-treated epithelial clusters for the top 50 differentially expressed genes **(Figure 3.3G)**. Direct examination of *FAT1* expression demonstrates its enrichment in epithelial cells across for all three conditions **(Figure 3.4A)**. While *FAT1* was not among the top 50 differentially expressed genes for the hypoxic condition, *FAT1* was still significantly depleted in hypoxic M cells, with an even larger fold change than growth factor-treated E to M cells **(Figure 3.4A)**. FAT1 suppression promotes a hybrid EMT in squamous cell carcinoma (198), and FAT1 activates the Hippo pathway in head and neck squamous cell carcinoma (188). In the aggregated data set, *FAT1* expression positively correlates with Hippo pathway enrichment **(Figure 3.4B)**. Based on this, we probed the relevance of *FAT1* and its gene product in determining the epithelial phenotype.

To analyze the role *FAT1* in the intact tumor setting, we used a published scRNA-seq data set of six PDAC patient tumors (88). Limiting the analysis to ductal cells only, the pcEMT signature was used to create two clusters **(Figure 3.4C)**, which were annotated as E and M based on their differential enrichment for mesenchymal and epithelial genes **(Figure 3.4D, Supp Figure 3.S4)**. Ductal cells in the epithelial cluster displayed greater *FAT1* expression than those in the mesenchymal cluster **(Figure 3.4E)**, consistent with the findings in HPAF-II cells.

To probe these inferences functionally *in vitro*, we knocked down *FAT1* in HPAF-II cells **(Figure 3.4F)**. *FAT1* depletion suppressed *CDH1* and promoted *VIM* transcript expression **(Figure 3.4G)** and promoted vimentin protein expression **(Figure 3.4H)**. FAT1-depleted cells also displayed increase nuclear accumulation of YAP **(Figure 3.4I)**, consistent with prior reports that FAT1 antagonizes YAP signaling by assembling the Hippo pathway (188). YAP nuclear localization was most common in vimentin-positive hypoxic cells **(Figure 3.4J)**. Thus, FAT1 depletion may promote YAP nuclear localization and resultant EMT.

We further tested whether the relationship between the current findings and our prior work demonstrating ERK and JNK signaling as required for hypoxia-mediated EMT (185). Combined MEK and JNK inhibition rescued *FAT1* expression in hypoxic culture **(Figure 3.4K)**, confirming key roles for these kinases in regulating *FAT1* as a feature of the epithelial cell state.

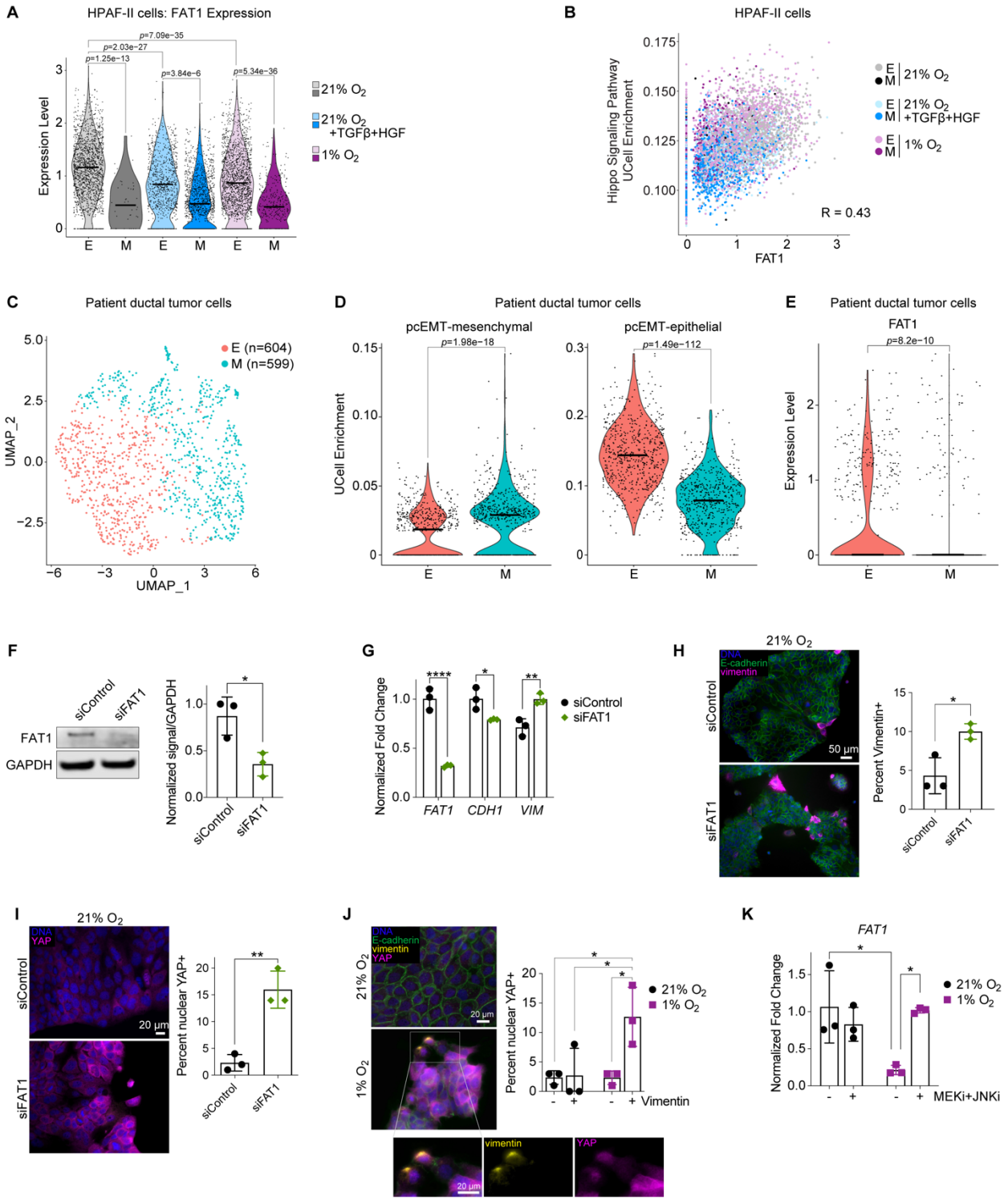

Figure 3.4 FAT1 expression is higher in epithelial cells

(A) The expression of *FAT1* per cell is displayed per E/M cluster per condition. A Kruskal-Wallis test with Dunn pairwise comparisons was performed, and the bar denotes the median. **(B)** The scatter plot displays the UCell enrichments for the KEGG Hippo Signaling Pathway and *FAT1* expression per cell for the

aggregated data as annotated by E/M clusters per condition. The Pearson correlation was calculated. **(C)** scRNA-seq from patient tumors (88) was subjected to the same analysis as with HPAF-II cells. A UMAP projection displays k-nearest neighbor clustering on the pcEMT gene signature into two clusters. **(D)** Scores for gene enrichment were calculated with UCell for the epithelial and mesenchymal portions of the pcEMT gene signature, identifying one cluster enriched in epithelial genes (E) and one enriched in mesenchymal genes (M). A Mann-Whitney test was performed, and the bar denotes the median. **(E)** The expression of *FAT1* per cell is displayed comparing the E and M cluster of the patient tumor data. A Wilcoxon test was performed, and the bar denotes the median. **(F)** HPAF-II cells were transfected with siRNA targeting FAT1 or control siRNA and cultured at 21% O_2 for 120 hr. Lysates were analyzed by immunoblotting for the indicated proteins. $n = 3$, t test. **(G)** qRT-PCR was performed for the indicated transcripts on RNA isolated from HPAF-II cells treated as described in (F). *CASC3* was used as a control gene for normalization. $n = 3$, two-way ANOVA with Sidak's multiple comparisons test comparing FAT1 to control siRNA for each transcript. **(H,I)** HPAF-II cells were treated as in (F) and immunofluorescence microscopy was performed for the indicated proteins. $n = 3$, t test. **(J)** HPAF-II cells were cultured in 21% or 1% O_2 for 120 hr and immunofluorescence microscopy was performed for the indicated proteins. $n = 3$, two-way ANOVA with Tukey's multiple comparison test. **(K)** HPAF-II cells were cultured in 21% or 1% O_2 with 1 μM CI-1040 (MEKi) and 10 μM SP600125 (JNKi), or DMSO for 120 hr, with inhibitors replenished every 48 hr. RNA was extracted, and qRT-PCR was performed for *FAT1*, with *CASC3* as a control gene for normalization. $n = 3$, two-way ANOVA with Tukey's multiple comparison test. * $p < 0.05$, ** $p < 0.01$, *** $p < 0.001$, **** $p < 0.0001$

AXL regulates hypoxia-mediated EMT.

The striking result in Figure 3.3E suggesting that *AXL* is primarily enriched in the hypoxic M cluster, and not in growth factor-treated M cells motivated investigation, motivated testing of AXL's function in hypoxia. In breast cancer, AXL can be a driver of EMT potentially through NFκB signaling (199), but AXL can also be a result of a mesenchymal transition with vimentin being required for AXL expression (191) . Therefore, it is unclear if AXL plays a supporting role in EMT or if it is a consequence of EMT. While little is known about the relationship between AXL and EMT in PDAC, AXL inhibition promotes PDAC chemosensitivity (200), making AXL an enticing target to explore.

To expand on the observation in Figure 3.3E, we confirmed that *AXL* is significantly enriched in hypoxic mesenchymal cells **(Figure 3.5A)**. To determine if this also occurs in the intact tumor microenvironment, we clustered ductal PDAC tumor cells from a published patient tumor scRNA-seq data set using the Hallmark Hypoxia gene set **(Figure 3.5B)**, which identified a cluster enriched in Hallmark Hypoxia and HIF-target genes, denoted as "HYP+" **(Figure 3.5C)**. HYP+ cells were then clustered using the pcEMT gene set features **(Figure 3.5D)**, which produced

clusters enriched in E or M genes **(Figure 3.5E)**. Within the pcEMT gene set, *AXL* was the most consistently differentially regulated gene between the E and M clusters **(Figure 3.5F)**. Consistent with the analysis of HPAF-II cells, *AXL* was preferentially enriched in hypoxic M cells **(Figure 3.5G)**. Interestingly, AXL inhibition prevented EMT in response to hypoxia but not in response to growth factors, suggesting a context-specific role for AXL in driving EMT **(Figure 3.5H)**.

Given the functional relevance of AXL, we sought to understand the protein expression of AXL in response to the EMT drivers. AXL intensity was greatest in hypoxic cells, but only nuclear AXL was increased in vimentin-positive cells. Increased nuclear AXL was observed in vimentin-positive cells from TGFβ+HGF or hypoxic treatment, with hypoxic mesenchymal cells displaying the highest overall nuclear AXL intensity **(Figure 3.6A)**. In some settings, nuclear AXL represents a proteolytic cleavage product of the full-length receptor containing a nuclear localization sequence (201), but there is still limited understanding for the role of nuclear AXL. Lysates of HPAF-II cells do not suggest the presence of a lower molecular weight cleavage in hypoxic culture though **(Figure 3.6B)**, despite the higher nuclear intensity by immunofluorescence microscopy. Given that YAP promotes *AXL* transcription (190), we tested for a correlation between YAP and AXL and found that nuclear AXL intensity was greatest in hypoxic cells displaying nuclear YAP **(Figure 3.6C)**. These results suggest a role of nuclear AXL in promoting EMT in mesenchymal hypoxic cells. Based on the aggregated analyses presented, we propose a mechanism wherein FAT1 loss inhibits the Hippo pathway and allows for YAP nuclear localization and resulting AXL expression, which promotes EMT.

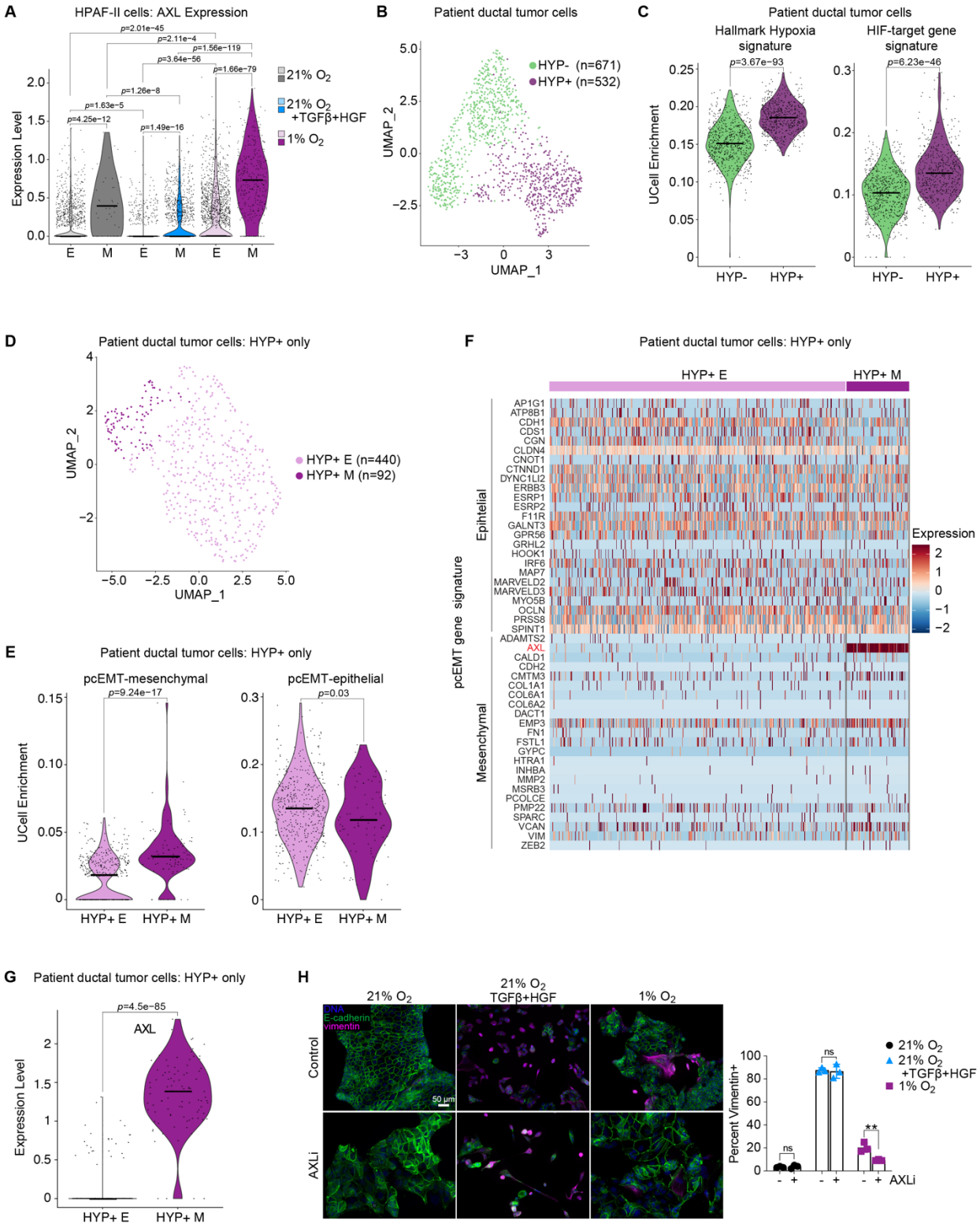

Figure 3.5 AXL is preferentially enriched in hypoxic mesenchymal cells

(A) The expression of *AXL* per cell is displayed per E/M cluster per condition. A Kruskal-Wallis test with Dunn pairwise comparisons was performed, and the bar denotes the median. **(B)** A UMAP projection

displays k-nearest neighbor (kNN) clustering on scRNA-seq from patient tumors (88) on the Hallmark Hypoxia gene set into two clusters. **(C)** Scores for gene enrichment were calculated with UCell for the Hallmark Hypoxia gene signature and HIF-target gene signature, identifying one clustered enriched in hypoxic genes (HYP+) compared to the other cluster (HYP-). A Mann-Whitney test was performed, and the bar denotes the median. **(D)** The HYP+ cluster from (B) was then subjected to kNN clustering using the pcEMT gene signature, as previously done with the HPAF-II data set. **(E)** Scores for gene enrichment were calculated with UCell for the epithelial and mesenchymal portions of the pcEMT gene signature, identifying one cluster enriched in epithelial genes (E) and one enriched in mesenchymal genes (M). A Mann-Whitney test was performed, and the bar denotes the median. **(F)** The heatmap displays the expression of the pcEMT genes for each of the E and M clusters for the HYP+ patient tumor ductal cells. **(G)** The expression of *AXL* per cell is displayed comparing the E and M cluster of the HYP+ patient tumor data. A Wilcoxon test was performed, and the bar denotes the median. **(H)** HPAF-II cells were cultured in 21% O_2 with or without 10 ng/mL TGFβ and 50 ng/mL HGF or cultured in 1% O_2, with 40 nM dubermatinib (AXLi) and or DMSO for 120 hr. Immunofluorescence microscopy was performed for the indicated proteins. $n = 3$, two-way ANOVA with Sidak's multiple comparison test. ** $p < 0.01$

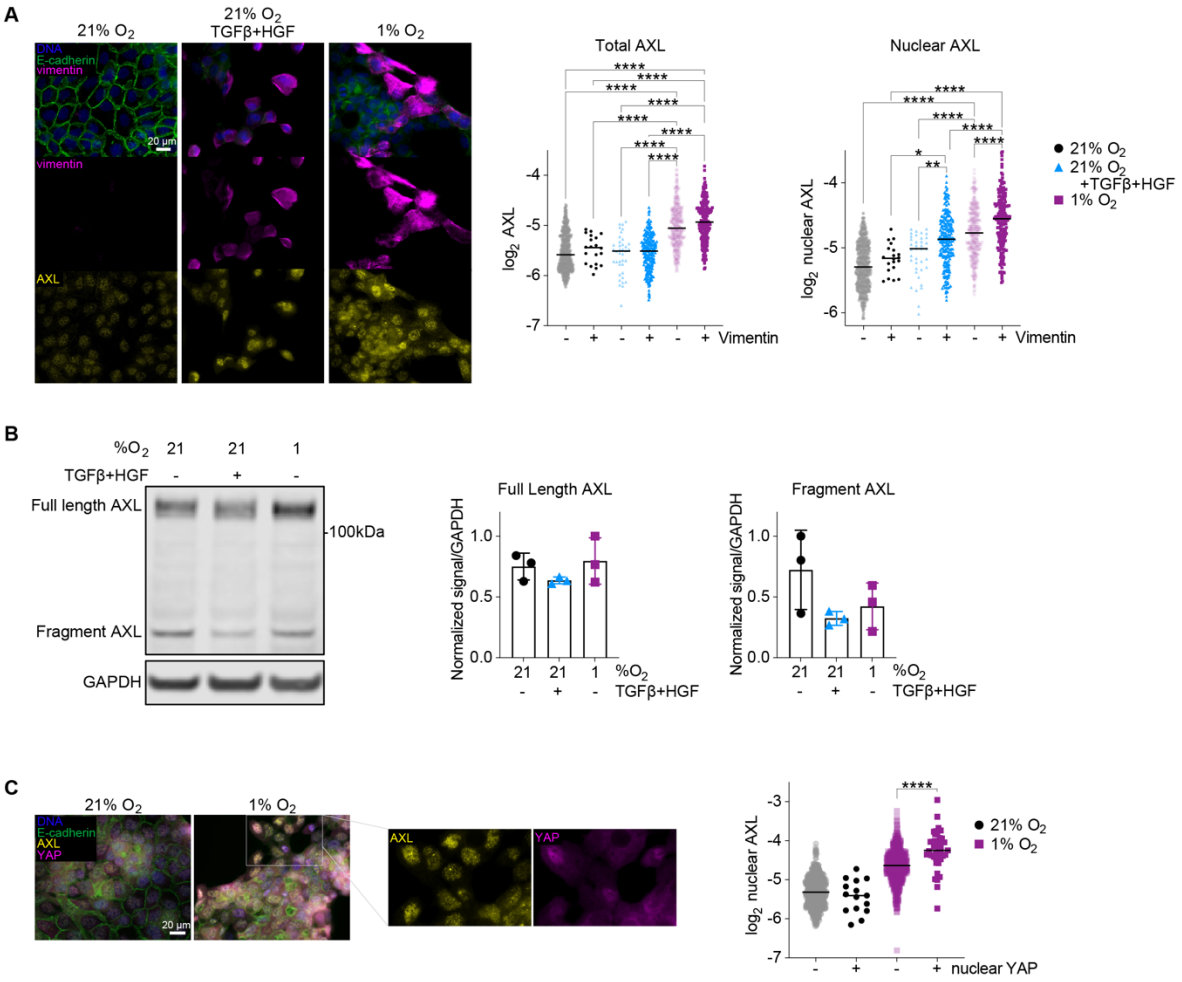

Figure 3.6 AXL is associated with YAP nuclear localization

(A) HPAF-II cells were cultured in 21% O_2 with or without 10 ng/mL TGFβ and 50 ng/mL HGF or cultured in 1% O_2 for 120 hr. Immunofluorescence microscopy was performed for the indicated proteins. *n* = 3, one-way ANOVA with Tukey's multiple comparisons test. **(B)** HPAF-II cells were cultured as in (A). Cells lysates were analyzed by immunoblotting for the indicated proteins. **(C)** HPAF-II cells were cultured in 21% or 1% O_2 for 120 hr and immunofluorescence microscopy was performed for the indicated proteins. *n* = 3, one-way ANOVA with Tukey's multiple comparisons test. * $p < 0.05$, ** $p < 0.01$, *** $p < 0.001$, **** $p < 0.0001$

3.5 DISCUSSION

In this study, we utilized scRNA-seq to understand heterogenous EMT transcriptional regulation in populations of pancreas cancer cells in response to different drivers of the mesenchymal transition. We identified both common and unique modes of EMT regulation at play between growth factor and hypoxia conditions. FAT1 was enriched across epithelial cells regardless of the treatment condition, whereas AXL played a context-dependent role in hypoxia-mediated EMT only. Previous work found that *FAT1* deletion promoted a hybrid EMT through YAP nuclear localization and ZEB1 expression in squamous cell carcinoma (198), and that FAT1 prevents EMT via suppression of the MAPK/ERK pathway in esophageal squamous cell cancer (202). Additionally, to account for the hypoxia-specific enrichment of AXL, studies have found that HIF-1α and HIF-2α directly promote AXL expression, which promotes SRC activity (203). We have previously established a role for SRC-dependent MAPK/ERK-signaling in regulating hypoxia-mediated EMT (185), which unifies the present study and previous findings on FAT1 and AXL to provide a mechanism for hypoxia-driven EMT in PDAC.

Aside from its role in EMT, AXL is involved in cell survival, angiogenesis, and immune response in pancreas cancer (204). AXL-deficient mice bearing pancreas tumors have increased survival, more differentiated tumor histology, and decreased metastasis, making AXL an attractive therapeutic target (205). Our results suggest a potentially interesting role for nuclear AXL in correlation with EMT. Nuclear AXL has been observed in various carcinomas, including schwannoma, melanoma, and mesothelioma (206-209); however, there is still more to interrogate regarding the function of nuclear AXL, especially in relation to EMT. One study identified in mesothelioma that there was nuclear colocalization of AXL and p53, and that AXL can bind to the *TP53* promoter to suppress expression (209). Several AXL inhibitors are in clinical trials for advanced solid tumors, and other diseases (ClinicalTrials.gov). However, only one clinical trial has tested AXL inhibitors in pancreas cancer, in combination with chemotherapy, and that study

was terminated to pursue other research (NCT03649321; ClinicalTrials.gov). There has yet to be another study initiated for AXL inhibition in PDAC. Given the bias for AXL expression in hypoxic mesenchymal cells, more success could be achieved from AXL inhibition by targeting AXL-driven EMT in cooperation with other therapies. Supporting the notion of an important role for AXL in PDAC pathogenesis, soluble AXL is a useful biomarker for classifying patients as healthy, tumor-burdened, or having chronic pancreatitis (210). Further, a current clinical trial in PDAC detects AXL-positive circulating tumor cells (CTCs) through real-time liquid biopsy to eventually correlate survival with the presence of AXL-positive CTCs (NCT05346536; ClinicalTrials.gov). Therefore, although AXL inhibition is still being investigated, detection of AXL could provide critical diagnostic insight in PDAC.

While our study focuses on EMT transcriptional regulation, post-translational and epigenetic modifications may also play important roles in determining EMT heterogeneity. The activity of different EMT transcription factors can be dependent on the context and stage in transition (211). Further, the localization and turnover of EMT transcription factors, including Snail, Slug, Twist, and ZEB1, are regulated by acetylation, phosphorylation, and ubiquitination (212,213). Mutations and post-translational modifications can also influence the activity of EMT-regulating signaling pathways, such as mutant KRAS promoting EMT in a MEK-dependent manner (135) and EGF-stimulated SHP2 activity augmenting EMT (32). Further, the Hippo pathway constrains YAP through phosphorylation-dependent degradation via LATS1/2 (214,215). In specific settings, histone methylation and acetylation marks are required for EMT, including histone 3 lysine 4 acetylation (H3K4Ac), histone 3 lysine 4 di-methylation (H3K4me2), histone 3 lysine 27 tri-methylation (H3K27me3), and histone 3 lysine 36 di-methylation (H3K36me2) (34-36). At least one of these marks (i.e., H3K36me2) is induced by both EMT-driving growth factors and hypoxia (34-36). Here, our analysis nominates H3 Histone Family 3A (*H3F3A*) as enriched in cells cultured in 21% or 1% O_2, potentially pointing to a context-specific role for H3F3A. Mass

cytometry and high-content, multi-channel immunofluorescence imaging will be important tools moving forward for discovering the potential supporting role of post-translational modifications in explaining EMT heterogeneity.

Given that mesenchymal cells are more resistant to chemotherapy (14), heterogeneity of EMT poses a significant challenge to treatment. One of the ways to combat this across carcinomas could be molecular subtyping to identify patients that will likely be more responsive (216). In PDAC, there are ongoing studies to classify patient tumors as classical or basal-like, since classical tumors are more responsive to the chemotherapy FOLFIRINOX (217). However, as identified through single-cell measurements in this study and others, there is significant heterogeneity in EMT between cells within a cell line and within a tumor. Since mesenchymal cells are chemoresistant (218), the existence of heterogenous EMT states creates a subpopulation of cells that are less chemoresponsive and likely to remain after treatment (219). A means to combat this heterogeneity could be to use small molecule drugs as neoadjuvants to antagonize EMT prior to conventional chemotherapy (220). Due to the heterogeneity of EMT and the regulatory processes that control it, identifying the most appropriate molecularly targeted drugs must leverage measurement and analysis techniques that accommodate cell-to-cell variability.

3.6 ACKNOWLEDGEMENTS

We thank Dr. David Tuveson (Cold Springs Harbor Laboratory) for sharing annotated tumor scRNAseq data. We acknowledge Dr. Katia Sol-Church at UVA Genome Analysis and Technology Core for assisting in experimental design and performing the scRNA-sequencing on HPAF-II cells. We thank Drs. Ben Stanger and Jason Pitarresi (University of Pennsylvania) for helpful technical discussions.

3.7 SUPPLEMENTAL MATERIAL

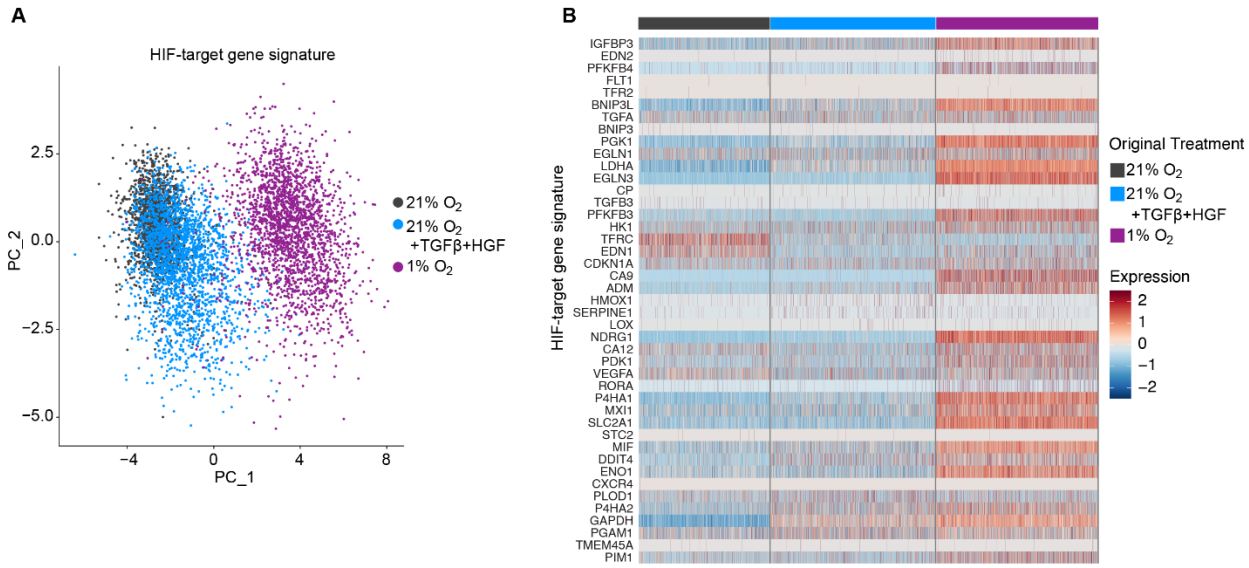

Supp Figure 3.S1 Hypoxic cell culture promoted expression of hypoxia-associated genes
(A) PCA on the HIF-target gene set was computed for the aggregated data as mapped to the experimental conditions. **(B)** The heatmap displays the expression of the HIF-target genes with annotation of the experimental conditions.

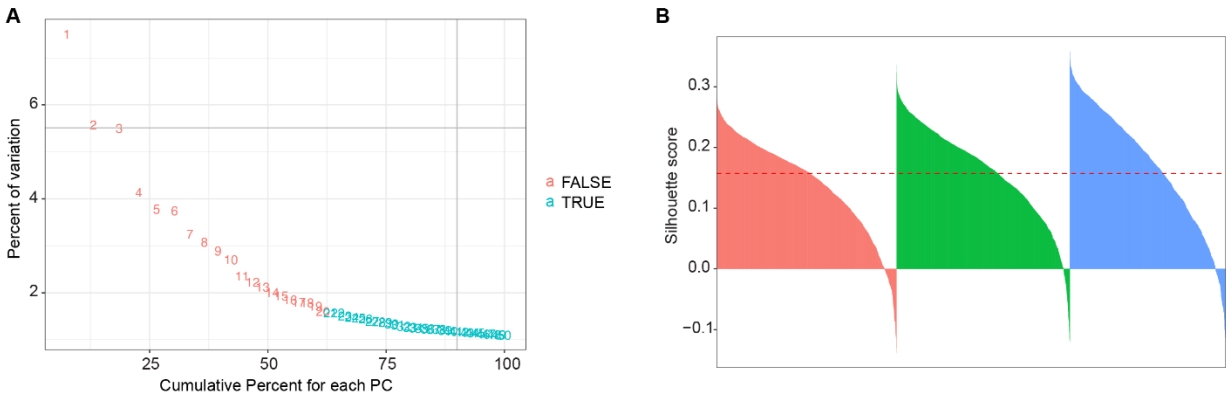

Supp Figure 3.S2 The optimal parameters were chosen for clustering on all genes within the data set

(A) An elbow plot showing the percent variation and cumulative percent for each principal component used for clustering in Figure 3.1B. Plotted numbers refer to the principal component (PC) number. Red and blue numbers indicate the change in percent variation to the next PC is greater than or less than 0.1%, respectively. **(B)** Silhouette scores are shown per cell by cluster for the optimal number of k-nearest neighbor clusters based on the aggregated data set.

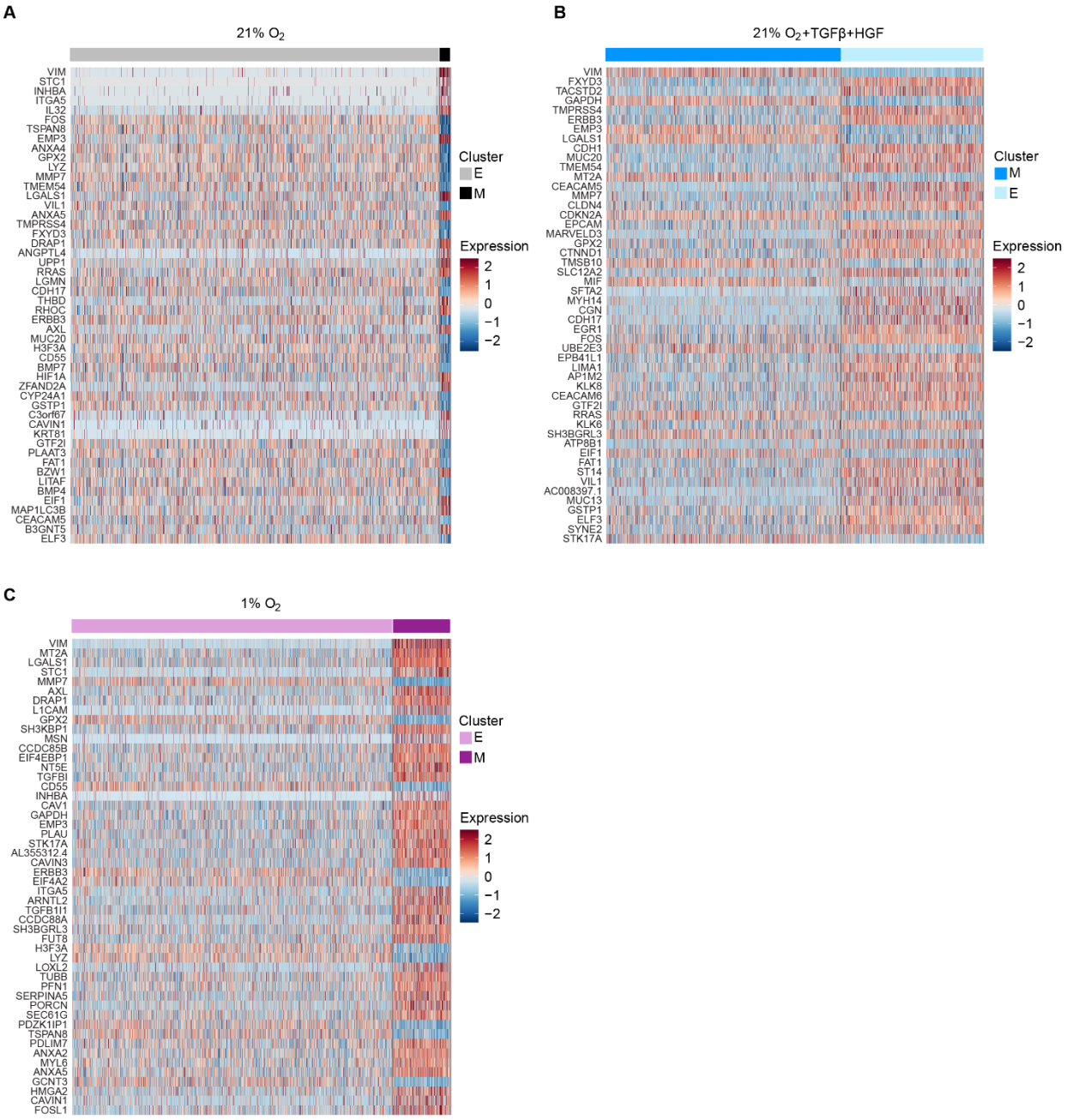

Supp Figure 3.S3 There was differential gene expression between epithelial and mesenchymal cells per treatment condition

(A-C) Heatmaps display the top 50 differentially expressed genes comparing the E and M clusters for each experimental conditions of **(A)** 21% O_2, **(B)** 21% O_2 with 10 ng/mL TGFβ and 50 ng/mL HGF, and **(C)** 1% O_2 in relation to the clusters from Figure 3.3A-C.

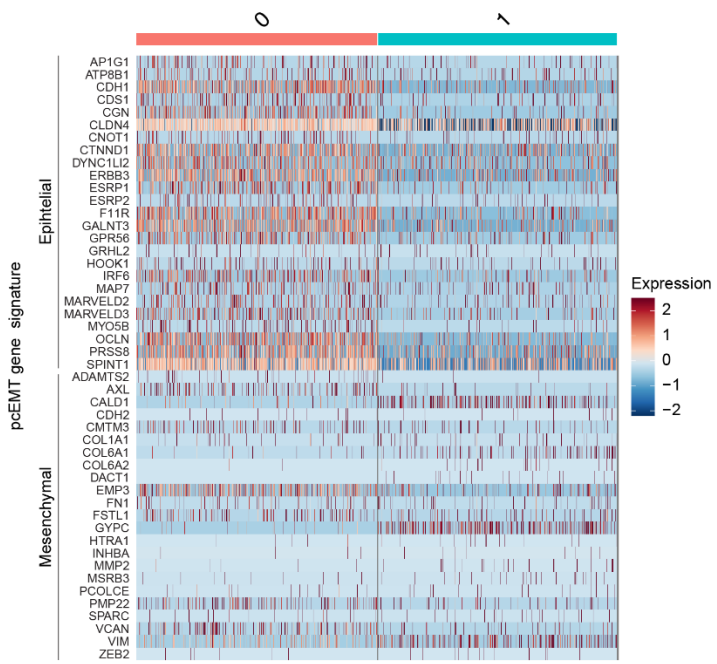

Supp Figure 3.S4 Patient ductal cells were clustered on EMT gene expression

The heatmap displays the gene expression of the pcEMT gene signature for the patient ductal cells as clustered in Figure 3.4C.

Supp Table 3.S1 Software and algorithms

RESOURCE	SOURCE
R v4.2.0	R Development Core Team
Bioconductor	(183)
cluster v2.1.4	(221)
clusterProfiler v4.4.4	(106,184)
dittoSeq v1.8.1	(222)
dplyr v1.0.9	(223)
escape v1.6.0	(224)
ggplot2 v3.3.6	(112)
ggstatsplot v0.9.4	(110)
limma v3.52.2	(225)
org.Hs.eg.db v3.15.0	(226)
patchwork v1.1.2	(227)
rlang v1.0.5	(228)
scRNABatchQC v0.10.4	(193)
Seurat v4.1.1	(229-232)
stringr v1.4.1	(233)
UCell v2.0.1	(195)

Supp Table 3.S2 qRT-PCR Primers

Target		Sequence (5' → 3')
CASC3	Forward	ACCTCGGAAAGGGCTCTTCTT
	Reverse	CGACCCTCATCCTTCCATAGC
CDH1	Forward	CATCAGGCCTCCGTTTCTG
	Reverse	GGAGTTGGGAAATGTGAGCA
VIM	Forward	TCTCTGAGGCTGCCAACCG
	Reverse	CGAAGGTGACGAGCCATTTCC
FAT1	Forward	TCTCTGAGGCTGCCAACCG
	Reverse	CGAAGGTGACGAGCCATTTCC

CHAPTER 4: CONCLUSIONS AND FUTURE WORK

4.1 SUMMARY

The work described in this thesis uncovers novel mechanisms by which hypoxia can promote a heterogeneous, but durable, EMT and highlights vulnerabilities in PDAC for therapeutic intervention. Throughout this work, we employed a variety of techniques and models to study hypoxia-mediated EMT through mouse models, single-cell and bulk omics, and cell-based assays to gain a comprehensive understanding of signal transduction at the epigenetic, protein, and transcriptional level. The extensive information gained through this thesis work not only provides valuable knowledge to the field of pancreas cancer research, but also postulates a direct therapeutic opportunity to inhibit signaling pathway targets to reverse a dangerous phenotype prevalent in pancreas cancer.

In Chapter 2, we gained an improved understanding of the complex regulation of EMT driven from the hypoxic tumor microenvironment. We identified a complex histone methylation-MAPK signaling axis responsible for driving a durable mesenchymal phenotype in PDAC. We determined that reduced activity of the oxygen-dependent histone demethylase KDM2A and the increased protein stabilization of the histone methyltransferase NSD2 allow for an increase in histone 3 lysine 36 dimethylation (H3K36me2). Through downregulation of protein phosphatases, SFK-mediated MAPK signaling is increased to drive an increase in nuclear cJun accumulation and ERK phosphorylation, as well as stabilization of HIF-1α. Our finding that MAPKs regulate HIF-1α expression, but that HIF-1α does not solely dictate hypoxia-mediated EMT was an interesting finding that motivated exploring additional means of cellular responses to low oxygen. Further, we utilized patient data to generate a hypothesis to test in cell lines and mouse models to develop a detailed mechanism of hypoxic regulation of EMT, which ultimately concluded in demonstrating that co-inhibition of MEK and JNK has a synergistic effect in preventing and

reversing durable hypoxia-driven EMT. The work from this chapter can be expanded to incorporate the effect of hypoxia-mediated EMT on chemoresponse and the influence of hypoxia on other cell types (e.g., CAFs). This would then allow for future studies of targeting MAPKs in combination with chemotherapy to improve efficacy.

In Chapter 3, we sought to understand the heterogeneity of EMT and directly compare the transcriptional regulation of hypoxia- and growth factor-mediated EMT. Through scRNA-seq of cells cultured with or without the addition of TGFβ + HGF, or in hypoxic culture, we were able to directly study the response of these drivers, as opposed to our work in Chapter 2 with patient tumor data sets where we had to utilize hypoxic gene sets as a means of correlating hypoxia with the cellular response. Although both drivers promoted EMT on net based on gene sets, the specific EMT-associated genes that they regulated were not identical. Further, we were able to determine that the Hippo pathway and *FAT1* were enriched in epithelial cells, whereas *AXL* was upregulated in mesenchymal cells, preferentially in response to hypoxic culture. We were able to validate these findings in patient tumor scRNA-seq data. Through cell-based assays, we confirmed the model findings by observing FAT1 to be lower in mesenchymal cells and that AXL inhibition only prevented EMT in hypoxic culture. We were intrigued by the nuclear localization of AXL, a phenomenon about which there is still limited published research. We acknowledge that there is still much to be uncovered from this unique data set, and we hope by making this data set publicly available that other researchers will generate and test new hypotheses.

4.2 CLINICAL IMPLICATIONS OF EMT

In pancreas cancer, there is a current clinical trial utilizing Purity Independent Subtyping of Tumors (PurIST) that stratifies patient tumors as classical (epithelial-like) or basal (mesenchymal-like) as a means of determining the therapeutic strategy (NCT04683315, ClinicalTrials.gov), based on the premise that basal-like tumors have been found to be less

responsive to the FOLIFIRNOX (9,217). Genomic data from patient tumors is analyzed for subtype-associated genes and scored based on the relative expression (217). For now, the trial consists of subjecting patients with a classical subtype to FOLFIRINOX and patients with a basal subtype to gemcitabine/nab-paclitaxel to understand if stratifying tumor subtypes by basal/classical will yield a better response rate to FOLFIRINOX. This study is still in early phase with no published results. However, the existence of the trial demonstrates that the field is pursuing PDAC classifications as a means of determining individual patient treatment plans and informing clinical trials to target the patient population that is most likely respond.

Given the reported role of EMT in metastasis and resistance to therapy, targeting EMT provides an attractive mechanism for improving therapeutic response. Previous studies have found that downregulation of the mesenchymal transcription factor ZEB1, through silencing of ZEB1 or interference via an HDAC inhibitor, sensitizes once gemcitabine-resistant mesenchymal PDAC cells to gemcitabine (234,235). Further, repurposing drugs can be successful in suppressing EMT by sensitizing pancreas cancer cells to gemcitabine. For example, metformin can promote the tumor suppressor miR-663 (236) and zidovudine can inhibit the Akt-GSK3β-Snail pathway (237) to reverse EMT. The work in this thesis identifies the drug targets of MEK and JNK for preventing hypoxia-mediated EMT. There already exist FDA-approved drugs for MEK [e.g., trametinib and selumetinib (238)] and investigational drugs targeting JNK in other cancer settings, which provides a path for further preclinical and eventual clinical testing of the effects of EMT antagonism as a means of improving chemoresponse.

4.3 EFFECTS OF HYPOXIA ON CELLULAR RESPONSE TO CHEMOTHERAPY

A premise of the work performed in this thesis is that hypoxia and growth factors, through their ability to drive EMT, may impact PDAC cancer cell response to chemotherapy. To lay the groundwork for the next steps in this long-term research plan, we have begun to investigate the

interplay between hypoxia and growth factors as drivers of EMT and chemotherapeutic response. In a set of new pilot experiments, we cultured HPAF-II pancreas cancer cells with or without TGFβ + HGF or in hypoxic culture prior to treating the cells with the chemotherapeutic gemcitabine and measuring cell death several days later. Cells grown in the hypoxic condition exhibited a greater degree of chemoresistance, reflected by a lower fraction of dead cells, than cells cultured in 21% O_2 with or without TGFβ + HGF **(Figure 4.1A)**. Surprisingly, growth factor treatment sensitized cells to gemcitabine, promoting a greater degree of cell death compared to 21% O_2 without growth factors. Hypoxic culture prevented some DNA damage, as measured by lower pH2A.X, which could explain the reduced induction of cell death **(Figure 4.1B)**. However, more work needs to be done to determine if this is a result of EMT or another hypoxia-regulated mechanism. Interestingly, gemcitabine caused EMT in pancreatic cancer cells. This is consistent with findings in the literature suggesting that PDAC cancer cells, and other carcinoma cells, may evade chemotherapy by undergoing an EMT. However, when cells were cultured in hypoxia, there was no supplementary EMT caused by the addition of gemcitabine **(Figure 4.1C)**. It is important to note that chemotherapies with mechanisms of action different than gemcitabine may drive different degrees of EMT and chemoresistance and potentially through different mechanisms. Future studies should confirm these trends in different cell lines and using different chemotherapies and growth factors and seek to clarify if the effects of hypoxia on chemoresistance are due primarily to EMT.

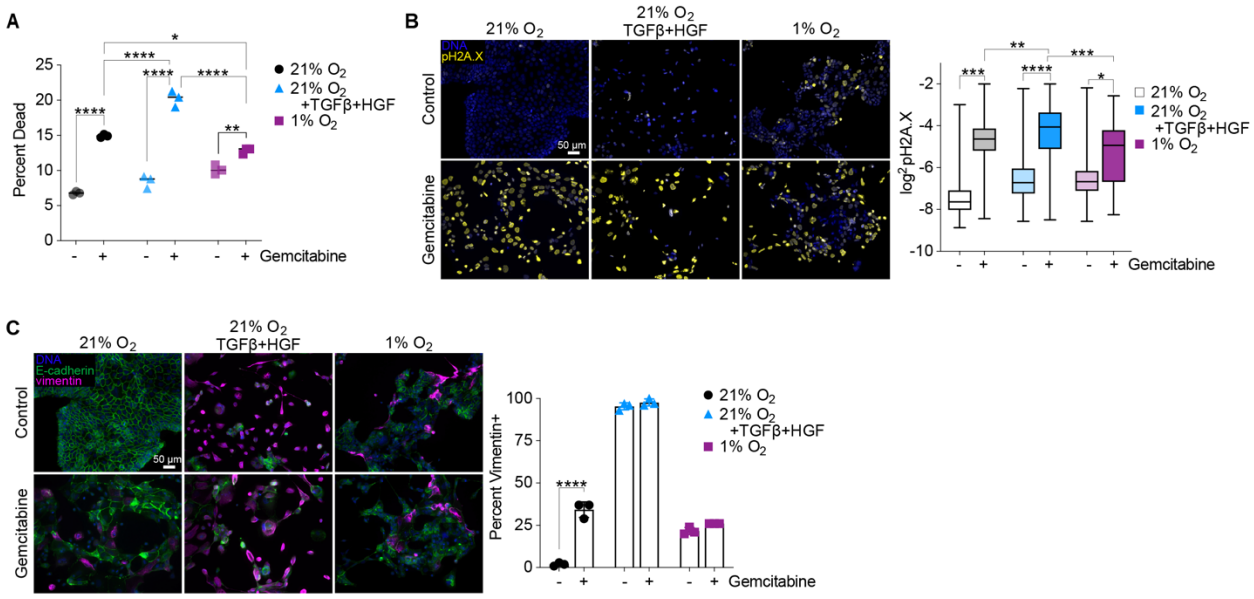

Figure 4.1 Hypoxia promotes gemcitabine resistance

(A-C) HPAF-II cells were cultured for 120 hr in 21% O_2 with or without 10 ng/mL TGFβ + 50 ng/mL HGF or in 1% O_2, then were exposed to 1 μg/mL gemcitabine for 72 hr. (A) Flow cytometry was performed for cell viability using ToPro3. *n* = 3, two-way ANOVA with Sidak's multiple comparison test. **(B)** Immunofluorescence was performed for the indicated proteins, with the intensity of pH2A.X measured for DNA damage. *n* = 3, mixed-effects analysis with Tukey's multiple comparison test. **(C)** Immunofluorescence was performed for the indicated proteins, with quantification of the percent positive vimentin cells. *n* = 3, two-way ANOVA with Sidak's multiple comparison test.

We are further testing the effects of hypoxia on gemcitabine resistance through *in vivo* studies. In ongoing studies, mice bearing orthotopic tumors created by injecting cells engineered with the hypoxia fate-mapping system (described in Chapter 2) are being treated with gemcitabine. We will assess the degree of DNA damage, via pH2A.X staining, in cells that experienced hypoxia versus those that did not. Further, to elucidate the involvement of EMT, we will stain for vimentin and ask if cellular resistance to gemcitabine occurs preferentially in the hypoxic mesenchymal cells. If there is no difference in DNA damage between hypoxic epithelial and mesenchymal cells, then hypoxic effects other than the induction of EMT, such as changes in metabolism, may be responsible for promoting the resistance to gemcitabine we observed in cell culture experiments. Additionally, we will evaluate the chemoresponse in epithelial and mesenchymal cells that did not experience hypoxia. Because hypoxia drives an especially durable

EMT, we hypothesize that once-hypoxic mesenchymal cells may be preferentially chemoresistant compared to never-hypoxic mesenchymal cells. The complete results of these studies may then motivate the investigation of combination therapy approaches based on the knowledge gained in Chapters 2 and 3 of this thesis. In Chapter 2, we found that MEK and JNK inhibition suppresses hypoxia-mediated EMT *in vivo*. Therefore, assuming hypoxia-induced chemoresistance is EMT-dependent, we can perform studies to dose kinase inhibitors to promote mesenchymal-epithelial transition (MET) prior to treating mice with gemcitabine, with the hypothesis that EMT antagonism would promote chemoresponse. This analysis can be expanded to other chemotherapies, such as FOLFIRINOX, to understand if the effects proposed here may depend on the chemotherapeutic. Additionally, the use of the hypoxia fate-mapping cells allows for tracing of once-hypoxic cells even in distal metastatic sites, which could provide additional insight into hypoxia as a regulator of response to chemotherapy in metastatic lesions. Although our current initial studies are being conducted to probe for effects on EMT, survival studies would ultimately need to be conducted to determine if targeting EMT prior to chemotherapy provides a benefit.

We were particularly intrigued by the finding in **Figure 4.1C** that gemcitabine in 21% O_2 caused EMT, but the addition of gemcitabine in 1% O_2 did not drive EMT more than hypoxic culture alone. This motivates further research into the signaling mechanisms governing gemcitabine-induced EMT. Given that both chemotherapy and hypoxia stimulate a stress response in cells, they could drive signaling through a common pathway such as JNK (239). Another hypothesis could be that the hypoxic response that is responsible for preventing chemotherapy-induced cell death is also preventing chemotherapy-induced EMT by not allowing for DNA damage to occur. To test these hypotheses, cells could be probed for their signaling response to chemotherapy in both 21% and 1% O_2. By employing multiplexed immunofluorescence microscopy, the gemcitabine-treated hypoxia fate-mapped tumors could be utilized to determine the gemcitabine-induced cell signaling response in hypoxic mesenchymal

cells. Collectively, these studies would help to determine the cellular response to gemcitabine under hypoxic stress.

4.4 IMPACT OF TUMOR HETEREOGENEITY ON TREATMENT

Tumor heterogeneity poses significant challenges for the design of effective therapies. The challenge of inter-tumoral heterogeneity across patients is being addressed through genetic subtyping for more informed treatment plans (217). However, there is significant intra-tumoral heterogeneity that needs to be overcome for complete tumor reduction. Tumors with greater diversity in genotypes are correlated with increased relapse and poorer outcomes (219) due to the existence of cell subpopulations that resist treatment and expand to drive tumor progression (219). In addition to intrinsic tumor cell heterogeneity, chemotherapy and radiation can also force mutations and modifications in cells leading to an even more diverse cell population (219).

In Chapter 3, we identified a subpopulation of hypoxic mesenchymal cells that are preferentially enriched in *AXL* in both cell line and patient tumor data. In cell culture studies, inhibition of AXL prevented hypoxia-mediated EMT but not growth factor-mediated EMT, identifying an important potential difference in the mode of regulation of EMT in the two different contexts. The potential value of targeting this cell subpopulation for clinical applications is unclear given that it is a small subset of cells. Preclinical testing in appropriate mouse models is needed to begin to understand this issue. There is an active clinical trial (NCT02183883, ClinicalTrials.gov) that is evaluating this concept through studying the response to an EGFR inhibitor in non-small cell lung cancer in tumors with varying degrees of mutations, including if the mutation is only in a subset of cells. The goal is to assess if the EGFR inhibitor is effective when the mutation is dominant (>50%), non-dominant (5-50%) or low frequency (<5%). Although the effect will ultimately depend on the target, trials such as this one will give insight into the effectiveness of targeting a subpopulation with an active mutation or overexpression.

Overcoming intra-tumoral heterogeneity will be a critical task for developing improved PDAC therapies. Improved clinical methods of assessing patient tumors will need to be adopted for single-cell resolution and temporal measurements to gain a more complete picture of patient tumors. To address spatial heterogeneity of the tumor microenvironment, including hypoxic domains and stromal interactions, it is recommended to biopsy the tumor from multiple locations if feasible (240). Genetic sequencing is helpful at the bulk level, but ultimately it may be more beneficial to not just assess “basal” or “classical” subtypes but to understand the spectrum of classification. Further, temporal measurements are critical to allow for an adaptive treatment regimen (241), and to understand how adaption occurs from heterogeneity.

4.5 COMBINATION THERAPY FOR TREATMENT OF PDAC

Our work in Chapter 2 demonstrates the utility of a combination of kinase inhibitors to suppress the mesenchymal phenotype in hypoxic PDAC cells. Tumor cell heterogeneity and the ability of cells to adaptively resist treatments also motivate the idea of using combinations of drugs to improve therapeutic efficacy. We found that inhibition of MEK and JNK can mitigate hypoxia-mediated EMT, which aligns with previous work suggesting MAPK signaling as a target for PDAC combination therapy. MEK/ERK inhibitors have been combined with anti-PD-L1 (155) and PI3K inhibitors (156), and low-dose “vertical inhibition” of RAF and ERK may promote a mesenchymal-epithelial transition in KRAS-mutant PDAC (157). JNK inhibition reduces FOLFOX (5-FU+LEU plus oxaliplatin) chemoresistance in PDAC (137). Our findings provide specific motivation for pursuing combinations of MAPK inhibitors for the complete antagonism of hypoxia-mediated EMT, which may potentiate PDAC response to chemotherapy. Given that there are approved MEK inhibitors and investigational JNK inhibitors, this combination is feasible to pursue. Our work also demonstrates a role for histone modifications and HIFs in hypoxia-mediated EMT. As selective histone methyltransferase and HIF inhibitors continue to be developed, it may become

possible to consider combining kinase inhibitors with entirely different classes of drugs to interrupt the feedback process we identified in Chapter 2, which we propose as a driver of PDAC chemoresistance.

As combination therapies are explored, questions of how to schedule multiple drugs naturally arise. Considering the often-significant side effects and toxicities of cancer therapies and the potential for undesirable drug interactions, there are practical barriers that limit how drugs can be deployed in combination. One recent study proposed a strategy of employing stochastic simulations of growth rates of sensitive and resistant cells to predict an optimal dosing regimen using continual and pulsed treatments of drugs to minimize the emergence of a resistant cell population in response to targeted therapies (242,243). Other work is investigating the application of optimal control mathematical models to design cancer therapy dosing schedules to optimize response (244). This would allow for a more systematic and informed decision making for dosing, especially when combining drugs. The objective is to utilize adaptive plans based on an evolutionary game theory model of cancer dynamics, instead of the standard administration of the maximum tolerated dose, to achieve the same impact on tumor growth while using less total drug (245). These models will be important in the practicality of combining therapies in order to minimize adverse events while maximizing the effects of pursuing different targets. Thinking in the context of EMT, it is conceivable to have a regimen of inhibitors that first reverses EMT to promote a cellular state that is more responsive to therapy and then follow those inhibitors with chemotherapy to promote an overall augmented chemoresponse.

REFERENCES

1. Yang J, Xu R, Wang C, Qiu J, Ren B, You L. Early screening and diagnosis strategies of pancreatic cancer: a comprehensive review. Cancer Commun (Lond) **2021**;41(12):1257-74 doi 10.1002/cac2.12204.
2. Haeno H, Gonen M, Davis MB, Herman JM, Iacobuzio-Donahue CA, Michor F. Computational modeling of pancreatic cancer reveals kinetics of metastasis suggesting optimum treatment strategies. Cell **2012**;148(1-2):362-75 doi 10.1016/j.cell.2011.11.060.
3. Yachida S, Jones S, Bozic I, Antal T, Leary R, Fu B*, et al.* Distant metastasis occurs late during the genetic evolution of pancreatic cancer. Nature **2010**;467(7319):1114-7 doi 10.1038/nature09515.
4. Mohammad AA. Advanced pancreatic cancer: The standard of care and new opportunities. Oncol Rev **2018**;12(2):370 doi 10.4081/oncol.2018.370.
5. McGuigan A, Kelly P, Turkington RC, Jones C, Coleman HG, McCain RS. Pancreatic cancer: A review of clinical diagnosis, epidemiology, treatment and outcomes. World J Gastroenterol **2018**;24(43):4846-61 doi 10.3748/wjg.v24.i43.4846.
6. Gbolahan OB, Tong Y, Sehdev A, O'Neil B, Shahda S. Overall survival of patients with recurrent pancreatic cancer treated with systemic therapy: a retrospective study. BMC Cancer **2019**;19(1):468 doi 10.1186/s12885-019-5630-4.
7. Heestand GM, Murphy JD, Lowy AM. Approach to patients with pancreatic cancer without detectable metastases. J Clin Oncol **2015**;33(16):1770-8 doi 10.1200/JCO.2014.59.7930.
8. Fan JQ, Wang MF, Chen HL, Shang D, Das JK, Song J. Current advances and outlooks in immunotherapy for pancreatic ductal adenocarcinoma. Mol Cancer **2020**;19(1):32 doi 10.1186/s12943-020-01151-3.
9. Moffitt RA, Marayati R, Flate EL, Volmar KE, Loeza SG, Hoadley KA*, et al.* Virtual microdissection identifies distinct tumor- and stroma-specific subtypes of pancreatic ductal adenocarcinoma. Nat Genet **2015**;47(10):1168-78 doi 10.1038/ng.3398.
10. Collisson EA, Sadanandam A, Olson P, Gibb WJ, Truitt M, Gu S*, et al.* Subtypes of pancreatic ductal adenocarcinoma and their differing responses to therapy. Nat Med **2011**;17(4):500-3 doi 10.1038/nm.2344.
11. Bailey P, Chang DK, Nones K, Johns AL, Patch AM, Gingras MC*, et al.* Genomic analyses identify molecular subtypes of pancreatic cancer. Nature **2016**;531(7592):47-52 doi 10.1038/nature16965.
12. Zheng X, Carstens JL, Kim J, Scheible M, Kaye J, Sugimoto H*, et al.* Epithelial-to-mesenchymal transition is dispensable for metastasis but induces chemoresistance in pancreatic cancer. Nature **2015**;527(7579):525-30 doi 10.1038/nature16064.
13. Rhim AD, Mirek ET, Aiello NM, Maitra A, Bailey JM, McAllister F*, et al.* EMT and dissemination precede pancreatic tumor formation. Cell **2012**;148(1-2):349-61 doi 10.1016/j.cell.2011.11.025.
14. Fischer KR, Durrans A, Lee S, Sheng J, Li F, Wong ST*, et al.* Epithelial-to-mesenchymal transition is not required for lung metastasis but contributes to chemoresistance. Nature **2015**;527(7579):472-6 doi 10.1038/nature15748.
15. Lu W, Kang Y. Epithelial-Mesenchymal Plasticity in Cancer Progression and Metastasis. Dev Cell **2019**;49(3):361-74 doi 10.1016/j.devcel.2019.04.010.
16. Leggett SE, Hruska AM, Guo M, Wong IY. The epithelial-mesenchymal transition and the cytoskeleton in bioengineered systems. Cell Commun Signal **2021**;19(1):32 doi 10.1186/s12964-021-00713-2.
17. Chaffer CL, San Juan BP, Lim E, Weinberg RA. EMT, cell plasticity and metastasis. Cancer Metastasis Rev **2016**;35(4):645-54 doi 10.1007/s10555-016-9648-7.

18. Stemmler MP, Eccles RL, Brabletz S, Brabletz T. Non-redundant functions of EMT transcription factors. Nat Cell Biol **2019**;21(1):102-12 doi 10.1038/s41556-018-0196-y.
19. Aiello NM, Maddipati R, Norgard RJ, Balli D, Li J, Yuan S*, et al.* EMT Subtype Influences Epithelial Plasticity and Mode of Cell Migration. Dev Cell **2018**;45(6):681-95 e4 doi 10.1016/j.devcel.2018.05.027.
20. Rochefort MM, Ankeny JS, Kadera BE, Donald GW, Isacoff W, Wainberg ZA*, et al.* Impact of tumor grade on pancreatic cancer prognosis: validation of a novel TNMG staging system. Ann Surg Oncol **2013**;20(13):4322-9 doi 10.1245/s10434-013-3159-3.
21. Dong X, Ma Y, Zhao X, Tian X, Sun Y, Yang Y*, et al.* Spatial heterogeneity in epithelial to mesenchymal transition properties of circulating tumor cells associated with distant recurrence in pancreatic cancer patients. Ann Transl Med **2020**;8(11):676 doi 10.21037/atm-20-782.
22. Zhao XH, Wang ZR, Chen CL, Di L, Bi ZF, Li ZH*, et al.* Molecular detection of epithelial-mesenchymal transition markers in circulating tumor cells from pancreatic cancer patients: Potential role in clinical practice. World J Gastroenterol **2019**;25(1):138-50 doi 10.3748/wjg.v25.i1.138.
23. Arumugam T, Ramachandran V, Fournier KF, Wang H, Marquis L, Abbruzzese JL*, et al.* Epithelial to mesenchymal transition contributes to drug resistance in pancreatic cancer. Cancer Res **2009**;69(14):5820-8 doi 10.1158/0008-5472.CAN-08-2819.
24. Suarez-Carmona M, Lesage J, Cataldo D, Gilles C. EMT and inflammation: inseparable actors of cancer progression. Mol Oncol **2017**;11(7):805-23 doi 10.1002/1878-0261.12095.
25. Gonzalez DM, Medici D. Signaling mechanisms of the epithelial-mesenchymal transition. Sci Signal **2014**;7(344):re8 doi 10.1126/scisignal.2005189.
26. Katsuno Y, Lamouille S, Derynck R. TGF-beta signaling and epithelial-mesenchymal transition in cancer progression. Curr Opin Oncol **2013**;25(1):76-84 doi 10.1097/CCO.0b013e32835b6371.
27. Heldin CH, Vanlandewijck M, Moustakas A. Regulation of EMT by TGFbeta in cancer. FEBS Lett **2012**;586(14):1959-70 doi 10.1016/j.febslet.2012.02.037.
28. Hao Y, Baker D, Ten Dijke P. TGF-beta-Mediated Epithelial-Mesenchymal Transition and Cancer Metastasis. Int J Mol Sci **2019**;20(11) doi 10.3390/ijms20112767.
29. Cook DP, Vanderhyden BC. Context specificity of the EMT transcriptional response. Nat Commun **2020**;11(1):2142 doi 10.1038/s41467-020-16066-2.
30. Deshmukh AP, Vasaikar SV, Tomczak K, Tripathi S, den Hollander P, Arslan E*, et al.* Identification of EMT signaling cross-talk and gene regulatory networks by single-cell RNA sequencing. Proc Natl Acad Sci U S A **2021**;118(19) doi 10.1073/pnas.2102050118.
31. Wade JD, Lun XK, Zivanovic N, Voit EO, Bodenmiller B. Mechanistic Model of Signaling Dynamics Across an Epithelial Mesenchymal Transition. Front Physiol **2020**;11:579117 doi 10.3389/fphys.2020.579117.
32. Buonato JM, Lan IS, Lazzara MJ. EGF augments TGFbeta-induced epithelial-mesenchymal transition by promoting SHP2 binding to GAB1. J Cell Sci **2015**;128(21):3898-909 doi 10.1242/jcs.169599.
33. Kim M, Costello J. DNA methylation: an epigenetic mark of cellular memory. Exp Mol Med **2017**;49(4):e322 doi 10.1038/emm.2017.10.
34. Yuan S, Natesan R, Sanchez-Rivera FJ, Li J, Bhanu NV, Yamazoe T*, et al.* Global Regulation of the Histone Mark H3K36me2 Underlies Epithelial Plasticity and Metastatic Progression. Cancer Discov **2020**;10(6):854-71 doi 10.1158/2159-8290.CD-19-1299.
35. Lin YT, Wu KJ. Epigenetic regulation of epithelial-mesenchymal transition: focusing on hypoxia and TGF-beta signaling. J Biomed Sci **2020**;27(1):39 doi 10.1186/s12929-020-00632-3.

36. Wu MZ, Tsai YP, Yang MH, Huang CH, Chang SY, Chang CC*, et al.* Interplay between HDAC3 and WDR5 is essential for hypoxia-induced epithelial-mesenchymal transition. Mol Cell **2011**;43(5):811-22 doi 10.1016/j.molcel.2011.07.012.
37. Neesse A, Michl P, Frese KK, Feig C, Cook N, Jacobetz MA*, et al.* Stromal biology and therapy in pancreatic cancer. Gut **2011**;60(6):861-8 doi 10.1136/gut.2010.226092.
38. Truong LH, Pauklin S. Pancreatic Cancer Microenvironment and Cellular Composition: Current Understandings and Therapeutic Approaches. Cancers (Basel) **2021**;13(19) doi 10.3390/cancers13195028.
39. Koong AC, Mehta VK, Le QT, Fisher GA, Terris DJ, Brown JM*, et al.* Pancreatic tumors show high levels of hypoxia. Int J Radiat Oncol Biol Phys **2000**;48(4):919-22 doi 10.1016/s0360-3016(00)00803-8.
40. Katsuta E, Qi Q, Peng X, Hochwald SN, Yan L, Takabe K. Pancreatic adenocarcinomas with mature blood vessels have better overall survival. Sci Rep **2019**;9(1):1310 doi 10.1038/s41598-018-37909-5.
41. Grunwald BT, Devisme A, Andrieux G, Vyas F, Aliar K, McCloskey CW*, et al.* Spatially confined sub-tumor microenvironments in pancreatic cancer. Cell **2021**;184(22):5577-92 e18 doi 10.1016/j.cell.2021.09.022.
42. Dhani NC, Serra S, Pintilie M, Schwock J, Xu J, Gallinger S*, et al.* Analysis of the intra- and intertumoral heterogeneity of hypoxia in pancreatic cancer patients receiving the nitroimidazole tracer pimonidazole. Br J Cancer **2015**;113(6):864-71 doi 10.1038/bjc.2015.284.
43. Yang S, Liu Q, Liao Q. Tumor-Associated Macrophages in Pancreatic Ductal Adenocarcinoma: Origin, Polarization, Function, and Reprogramming. Front Cell Dev Biol **2020**;8:607209 doi 10.3389/fcell.2020.607209.
44. Vaish U, Jain T, Are AC, Dudeja V. Cancer-Associated Fibroblasts in Pancreatic Ductal Adenocarcinoma: An Update on Heterogeneity and Therapeutic Targeting. Int J Mol Sci **2021**;22(24) doi 10.3390/ijms222413408.
45. Ohlund D, Handly-Santana A, Biffi G, Elyada E, Almeida AS, Ponz-Sarvise M*, et al.* Distinct populations of inflammatory fibroblasts and myofibroblasts in pancreatic cancer. J Exp Med **2017**;214(3):579-96 doi 10.1084/jem.20162024.
46. Pereira BA, Vennin C, Papanicolaou M, Chambers CR, Herrmann D, Morton JP*, et al.* CAF Subpopulations: A New Reservoir of Stromal Targets in Pancreatic Cancer. Trends Cancer **2019**;5(11):724-41 doi 10.1016/j.trecan.2019.09.010.
47. Hosein AN, Brekken RA, Maitra A. Pancreatic cancer stroma: an update on therapeutic targeting strategies. Nat Rev Gastroenterol Hepatol **2020**;17(8):487-505 doi 10.1038/s41575-020-0300-1.
48. Bulle A, Lim KH. Beyond just a tight fortress: contribution of stroma to epithelial-mesenchymal transition in pancreatic cancer. Signal Transduct Target Ther **2020**;5(1):249 doi 10.1038/s41392-020-00341-1.
49. Galbraith CG, Yamada KM, Sheetz MP. The relationship between force and focal complex development. J Cell Biol **2002**;159(4):695-705 doi 10.1083/jcb.200204153.
50. Brown JM, Giaccia AJ. The unique physiology of solid tumors: opportunities (and problems) for cancer therapy. Cancer Res **1998**;58(7):1408-16.
51. Helmlinger G, Yuan F, Dellian M, Jain RK. Interstitial pH and pO2 gradients in solid tumors in vivo: high-resolution measurements reveal a lack of correlation. Nat Med **1997**;3(2):177-82 doi 10.1038/nm0297-177.
52. Vaupel P, Thews O, Hoeckel M. Treatment resistance of solid tumors: role of hypoxia and anemia. Med Oncol **2001**;18(4):243-59 doi 10.1385/MO:18:4:243.
53. Vaupel P, Hockel M, Mayer A. Detection and characterization of tumor hypoxia using pO2 histography. Antioxid Redox Signal **2007**;9(8):1221-35 doi 10.1089/ars.2007.1628.

54. Kelleher DK, Mattheinsen U, Thews O, Vaupel P. Blood flow, oxygenation, and bioenergetic status of tumors after erythropoietin treatment in normal and anemic rats. Cancer Res **1996**;56(20):4728-34.
55. Ludwig H, Van Belle S, Barrett-Lee P, Birgegard G, Bokemeyer C, Gascon P*, et al.* The European Cancer Anaemia Survey (ECAS): a large, multinational, prospective survey defining the prevalence, incidence, and treatment of anaemia in cancer patients. Eur J Cancer **2004**;40(15):2293-306 doi 10.1016/j.ejca.2004.06.019.
56. Oberhoff C, Neri B, Amadori D, Petry KU, Gamucci T, Rebmann U*, et al.* Recombinant human erythropoietin in the treatment of chemotherapy-induced anemia and prevention of transfusion requirement associated with solid tumors: a randomized, controlled study. Ann Oncol **1998**;9(3):255-60 doi 10.1023/a:1008296622469.
57. McKeown SR. Defining normoxia, physoxia and hypoxia in tumours-implications for treatment response. Br J Radiol **2014**;87(1035):20130676 doi 10.1259/bjr.20130676.
58. Bertout JA, Patel SA, Simon MC. The impact of O2 availability on human cancer. Nat Rev Cancer **2008**;8(12):967-75 doi 10.1038/nrc2540.
59. Lee KE, Spata M, Bayne LJ, Buza EL, Durham AC, Allman D*, et al.* Hif1a Deletion Reveals Pro-Neoplastic Function of B Cells in Pancreatic Neoplasia. Cancer Discov **2016**;6(3):256-69 doi 10.1158/2159-8290.CD-15-0822.
60. Luo W, Wang Y. Epigenetic regulators: multifunctional proteins modulating hypoxia-inducible factor-alpha protein stability and activity. Cell Mol Life Sci **2018**;75(6):1043-56 doi 10.1007/s00018-017-2684-9.
61. Bae YS, Kang SW, Seo MS, Baines IC, Tekle E, Chock PB*, et al.* Epidermal growth factor (EGF)-induced generation of hydrogen peroxide. Role in EGF receptor-mediated tyrosine phosphorylation. J Biol Chem **1997**;272(1):217-21.
62. Shimojo Y, Akimoto M, Hisanaga T, Tanaka T, Tajima Y, Honma Y*, et al.* Attenuation of reactive oxygen species by antioxidants suppresses hypoxia-induced epithelial-mesenchymal transition and metastasis of pancreatic cancer cells. Clin Exp Metastasis **2013**;30(2):143-54 doi 10.1007/s10585-012-9519-8.
63. Chakraborty AA, Laukka T, Myllykoski M, Ringel AE, Booker MA, Tolstorukov MY*, et al.* Histone demethylase KDM6A directly senses oxygen to control chromatin and cell fate. Science **2019**;363(6432):1217-22 doi 10.1126/science.aaw1026.
64. Batie M, Frost J, Frost M, Wilson JW, Schofield P, Rocha S. Hypoxia induces rapid changes to histone methylation and reprograms chromatin. Science **2019**;363(6432):1222-6 doi 10.1126/science.aau5870.
65. Chang Q, Jurisica I, Do T, Hedley DW. Hypoxia predicts aggressive growth and spontaneous metastasis formation from orthotopically grown primary xenografts of human pancreatic cancer. Cancer Res **2011**;71(8):3110-20 doi 10.1158/0008-5472.CAN-10-4049.
66. Yokoi K, Fidler IJ. Hypoxia increases resistance of human pancreatic cancer cells to apoptosis induced by gemcitabine. Clin Cancer Res **2004**;10(7):2299-306 doi 10.1158/1078-0432.ccr-03-0488.
67. Yang MH, Wu MZ, Chiou SH, Chen PM, Chang SY, Liu CJ*, et al.* Direct regulation of TWIST by HIF-1alpha promotes metastasis. Nat Cell Biol **2008**;10(3):295-305 doi 10.1038/ncb1691.
68. Salnikov AV, Liu L, Platen M, Gladkich J, Salnikova O, Ryschich E*, et al.* Hypoxia induces EMT in low and highly aggressive pancreatic tumor cells but only cells with cancer stem cell characteristics acquire pronounced migratory potential. PLoS One **2012**;7(9):e46391 doi 10.1371/journal.pone.0046391.

69. Moen I, Oyan AM, Kalland KH, Tronstad KJ, Akslen LA, Chekenya M*, et al.* Hyperoxic treatment induces mesenchymal-to-epithelial transition in a rat adenocarcinoma model. PLoS One **2009**;4(7):e6381 doi 10.1371/journal.pone.0006381.
70. Sahlgren C, Gustafsson MV, Jin S, Poellinger L, Lendahl U. Notch signaling mediates hypoxia-induced tumor cell migration and invasion. Proc Natl Acad Sci U S A **2008**;105(17):6392-7 doi 10.1073/pnas.0802047105.
71. Wenger RH, Kurtcuoglu V, Scholz CC, Marti HH, Hoogewijs D. Frequently asked questions in hypoxia research. Hypoxia (Auckl) **2015**;3:35-43 doi 10.2147/HP.S92198.
72. Pavlacky J, Polak J. Technical Feasibility and Physiological Relevance of Hypoxic Cell Culture Models. Front Endocrinol (Lausanne) **2020**;11:57 doi 10.3389/fendo.2020.00057.
73. Sinha D, Saha P, Samanta A, Bishayee A. Emerging Concepts of Hybrid Epithelial-to-Mesenchymal Transition in Cancer Progression. Biomolecules **2020**;10(11) doi 10.3390/biom10111561.
74. Luond F, Sugiyama N, Bill R, Bornes L, Hager C, Tang F*, et al.* Distinct contributions of partial and full EMT to breast cancer malignancy. Dev Cell **2021**;56(23):3203-21 e11 doi 10.1016/j.devcel.2021.11.006.
75. Kim E, Kim JY, Smith MA, Haura EB, Anderson ARA. Cell signaling heterogeneity is modulated by both cell-intrinsic and -extrinsic mechanisms: An integrated approach to understanding targeted therapy. PLoS Biol **2018**;16(3):e2002930 doi 10.1371/journal.pbio.2002930.
76. Singh DK, Ku CJ, Wichaidit C, Steininger RJ, 3rd, Wu LF, Altschuler SJ. Patterns of basal signaling heterogeneity can distinguish cellular populations with different drug sensitivities. Mol Syst Biol **2010**;6:369 doi 10.1038/msb.2010.22.
77. Yi H, Li G, Long Y, Liang W, Cui H, Zhang B*, et al.* Integrative multi-omics analysis of a colon cancer cell line with heterogeneous Wnt activity revealed RUNX2 as an epigenetic regulator of EMT. Oncogene **2020**;39(28):5152-64 doi 10.1038/s41388-020-1351-z.
78. Cao L, Huang C, Cui Zhou D, Hu Y, Lih TM, Savage SR*, et al.* Proteogenomic characterization of pancreatic ductal adenocarcinoma. Cell **2021**;184(19):5031-52 e26 doi 10.1016/j.cell.2021.08.023.
79. Ben Q, An W, Sun Y, Qian A, Liu J, Zou D*, et al.* A nicotine-induced positive feedback loop between HIF1A and YAP1 contributes to epithelial-to-mesenchymal transition in pancreatic ductal adenocarcinoma. J Exp Clin Cancer Res **2020**;39(1):181 doi 10.1186/s13046-020-01689-6.
80. Chen S, Chen JZ, Zhang JQ, Chen HX, Yan ML, Huang L*, et al.* Hypoxia induces TWIST-activated epithelial-mesenchymal transition and proliferation of pancreatic cancer cells in vitro and in nude mice. Cancer Lett **2016**;383(1):73-84 doi 10.1016/j.canlet.2016.09.027.
81. Li H, Peng C, Zhu C, Nie S, Qian X, Shi Z*, et al.* Hypoxia promotes the metastasis of pancreatic cancer through regulating NOX4/KDM5A-mediated histone methylation modification changes in a HIF1A-independent manner. Clin Epigenetics **2021**;13(1):18 doi 10.1186/s13148-021-01016-6.
82. Tam SY, Wu VWC, Law HKW. Hypoxia-Induced Epithelial-Mesenchymal Transition in Cancers: HIF-1alpha and Beyond. Front Oncol **2020**;10:486 doi 10.3389/fonc.2020.00486.
83. Wei H, Xu Z, Liu F, Wang F, Wang X, Sun X*, et al.* Hypoxia induces oncogene yes-associated protein 1 nuclear translocation to promote pancreatic ductal adenocarcinoma invasion via epithelial-mesenchymal transition. Tumour Biol **2017**;39(5):1010428317691684 doi 10.1177/1010428317691684.
84. Zhang Q, Lou Y, Zhang J, Fu Q, Wei T, Sun X*, et al.* Hypoxia-inducible factor-2alpha promotes tumor progression and has crosstalk with Wnt/beta-catenin signaling in pancreatic cancer. Mol Cancer **2017**;16(1):119 doi 10.1186/s12943-017-0689-5.

85. Chen B, Li L, Li M, Wang X. HIF1A expression correlates with increased tumor immune and stromal signatures and aggressive phenotypes in human cancers. Cell Oncol (Dordr) **2020**;43(5):877-88 doi 10.1007/s13402-020-00534-4.
86. Losman JA, Koivunen P, Kaelin WG, Jr. 2-Oxoglutarate-dependent dioxygenases in cancer. Nat Rev Cancer **2020**;20(12):710-26 doi 10.1038/s41568-020-00303-3.
87. Ma W, Kim S, Chowdhury S, Li Z, Yang M, Yoo S*, et al.* DreamAI: algorithm for the imputation of proteomics data. bioRxiv **2021**.
88. Elyada E, Bolisetty M, Laise P, Flynn WF, Courtois ET, Burkhart RA*, et al.* Cross-Species Single-Cell Analysis of Pancreatic Ductal Adenocarcinoma Reveals Antigen-Presenting Cancer-Associated Fibroblasts. Cancer Discov **2019**;9(8):1102-23 doi 10.1158/2159-8290.CD-19-0094.
89. Mak MP, Tong P, Diao L, Cardnell RJ, Gibbons DL, William WN*, et al.* A Patient-Derived, Pan-Cancer EMT Signature Identifies Global Molecular Alterations and Immune Target Enrichment Following Epithelial-to-Mesenchymal Transition. Clin Cancer Res **2016**;22(3):609-20 doi 10.1158/1078-0432.CCR-15-0876.
90. Li B, Qiu B, Lee DS, Walton ZE, Ochocki JD, Mathew LK*, et al.* Fructose-1,6-bisphosphatase opposes renal carcinoma progression. Nature **2014**;513(7517):251-5 doi 10.1038/nature13557.
91. Liberzon A, Birger C, Thorvaldsdottir H, Ghandi M, Mesirov JP, Tamayo P. The Molecular Signatures Database (MSigDB) hallmark gene set collection. Cell Syst **2015**;1(6):417-25 doi 10.1016/j.cels.2015.12.004.
92. Kanehisa M, Furumichi M, Tanabe M, Sato Y, Morishima K. KEGG: new perspectives on genomes, pathways, diseases and drugs. Nucleic Acids Res **2017**;45(D1):D353-D61 doi 10.1093/nar/gkw1092.
93. Kanehisa M, Goto S. KEGG: kyoto encyclopedia of genes and genomes. Nucleic Acids Res **2000**;28(1):27-30 doi 10.1093/nar/28.1.27.
94. Sturm G, Finotello F, Petitprez F, Zhang JD, Baumbach J, Fridman WH*, et al.* Comprehensive evaluation of transcriptome-based cell-type quantification methods for immuno-oncology. Bioinformatics **2019**;35(14):i436-i45 doi 10.1093/bioinformatics/btz363.
95. Racle J, de Jonge K, Baumgaertner P, Speiser DE, Gfeller D. Simultaneous enumeration of cancer and immune cell types from bulk tumor gene expression data. Elife **2017**;6 doi 10.7554/eLife.26476.
96. Gaujoux R, Seoighe C. A flexible R package for nonnegative matrix factorization. BMC Bioinformatics **2010**;11:367 doi 10.1186/1471-2105-11-367.
97. Brunet JP, Tamayo P, Golub TR, Mesirov JP. Metagenes and molecular pattern discovery using matrix factorization. Proc Natl Acad Sci U S A **2004**;101(12):4164-9 doi 10.1073/pnas.0308531101.
98. Kim H, Park H. Sparse non-negative matrix factorizations via alternating non-negativity-constrained least squares for microarray data analysis. Bioinformatics **2007**;23(12):1495-502 doi 10.1093/bioinformatics/btm134.
99. Rousseeuw P. Silhouettes: A graphical aid to the interpretation and validation of cluster analysis. Journal of Computational and Applied Mathematics **1987**;20:53-65.
100. Monti S, Tamayo P, Mesirov J, Golub T. Consensus Clustering: A Resampling-Based Method for Class Discovery and Visualization of Gene Expression Microarray Data. Machine Learning **2003**;52:91-118.
101. Wilkerson MD, Hayes DN. ConsensusClusterPlus: a class discovery tool with confidence assessments and item tracking. Bioinformatics **2010**;26(12):1572-3 doi 10.1093/bioinformatics/btq170.

102. Hanzelmann S, Castelo R, Guinney J. GSVA: gene set variation analysis for microarray and RNA-seq data. BMC Bioinformatics **2013**;14:7 doi 10.1186/1471-2105-14-7.
103. Zhang Y, Ma Y, Huang Y, Zhang Y, Jiang Q, Zhou M*, et al.* Benchmarking algorithms for pathway activity transformation of single-cell RNA-seq data. Comput Struct Biotechnol J **2020**;18:2953-61 doi 10.1016/j.csbj.2020.10.007.
104. Lake BB, Chen S, Sos BC, Fan J, Kaeser GE, Yung YC*, et al.* Integrative single-cell analysis of transcriptional and epigenetic states in the human adult brain. Nat Biotechnol **2018**;36(1):70-80 doi 10.1038/nbt.4038.
105. Fan J, Salathia N, Liu R, Kaeser GE, Yung YC, Herman JL*, et al.* Characterizing transcriptional heterogeneity through pathway and gene set overdispersion analysis. Nat Methods **2016**;13(3):241-4 doi 10.1038/nmeth.3734.
106. Wu T, Hu E, Xu S, Chen M, Guo P, Dai Z*, et al.* clusterProfiler 4.0: A universal enrichment tool for interpreting omics data. Innovation (N Y) **2021**;2(3):100141 doi 10.1016/j.xinn.2021.100141.
107. Benjamini Y, Hochberg Y. Controlling the False Discovery Rate: A Practical and Powerful Approach to Multiple Testing. Journal of the Royal Statistical Society **1995**;57(1):289-300.
108. Friedman J, Hastie T, Tibshirani R. Regularization Paths for Generalized Linear Models via Coordinate Descent. J Stat Softw **2010**;33(1):1-22.
109. Akaike H. A new look at the statistical model identification. IEEE Transaction on Automatic Control **1974**;19(6):716-23.
110. Patil I. Visualizations with statistical details: The 'ggstatsplot' approach. Journal of Open Source Software **2021**;6(61):3167.
111. Therneau T. 2022 A Package for Survival Analysis in R. <https://CRAN.R-project.org/package=survival.>.
112. Wickham H. 2016 ggplot2: Elegant Graphics for Data Analysis. Springer-Verlag New York.
113. Mangiola S, Papenfuss A. tidyHeatmap: an R package for modular heatmap production based on tidy principles. Journal of Open Source Software **2020**;5:2472.
114. Gu Z, Eils R, Schlesner M. Complex heatmaps reveal patterns and correlations in multidimensional genomic data. Bioinformatics **2016**;32(18):2847-9 doi 10.1093/bioinformatics/btw313.
115. Lex A, Gehlenborg N, Strobelt H, Vuillemot R, Pfister H. UpSet: Visualization of Intersecting Sets. IEEE Trans Vis Comput Graph **2014**;20(12):1983-92 doi 10.1109/TVCG.2014.2346248.
116. Walters DM, Stokes JB, Adair SJ, Stelow EB, Borgman CA, Lowrey BT*, et al.* Clinical, molecular and genetic validation of a murine orthotopic xenograft model of pancreatic adenocarcinoma using fresh human specimens. PLoS One **2013**;8(10):e77065 doi 10.1371/journal.pone.0077065.
117. Michaels AD, Newhook TE, Adair SJ, Morioka S, Goudreau BJ, Nagdas S*, et al.* CD47 Blockade as an Adjuvant Immunotherapy for Resectable Pancreatic Cancer. Clin Cancer Res **2018**;24(6):1415-25 doi 10.1158/1078-0432.CCR-17-2283.
118. Li J, Byrne KT, Yan F, Yamazoe T, Chen Z, Baslan T*, et al.* Tumor Cell-Intrinsic Factors Underlie Heterogeneity of Immune Cell Infiltration and Response to Immunotherapy. Immunity **2018**;49(1):178-93 e7 doi 10.1016/j.immuni.2018.06.006.
119. Norgard RJ, Pitarresi JR, Maddipati R, Aiello-Couzo NM, Balli D, Li J*, et al.* Calcium signaling induces a partial EMT. EMBO Rep **2021**:e51872 doi 10.15252/embr.202051872.
120. Adam M, Potter AS, Potter SS. Psychrophilic proteases dramatically reduce single-cell RNA-seq artifacts: a molecular atlas of kidney development. Development **2017**;144(19):3625-32 doi 10.1242/dev.151142.

121. Carpenter AE, Jones TR, Lamprecht MR, Clarke C, Kang IH, Friman O*, et al.* CellProfiler: image analysis software for identifying and quantifying cell phenotypes. Genome Biol **2006**;7(10):R100 doi 10.1186/gb-2006-7-10-r100.
122. Kamentsky L, Jones TR, Fraser A, Bray MA, Logan DJ, Madden KL*, et al.* Improved structure, function and compatibility for CellProfiler: modular high-throughput image analysis software. Bioinformatics **2011**;27(8):1179-80 doi 10.1093/bioinformatics/btr095.
123. McQuin C, Goodman A, Chernyshev V, Kamentsky L, Cimini BA, Karhohs KW*, et al.* CellProfiler 3.0: Next-generation image processing for biology. PLoS Biol **2018**;16(7):e2005970 doi 10.1371/journal.pbio.2005970.
124. Schmittgen TD, Livak KJ. Analyzing real-time PCR data by the comparative C(T) method. Nat Protoc **2008**;3(6):1101-8 doi 10.1038/nprot.2008.73.
125. Godet I, Shin YJ, Ju JA, Ye IC, Wang G, Gilkes DM. Fate-mapping post-hypoxic tumor cells reveals a ROS-resistant phenotype that promotes metastasis. Nat Commun **2019**;10(1):4862 doi 10.1038/s41467-019-12412-1.
126. Laukka T, Myllykoski M, Looper RE, Koivunen P. Cancer-associated 2-oxoglutarate analogues modify histone methylation by inhibiting histone lysine demethylases. J Mol Biol **2018**;430(18 Pt B):3081-92 doi 10.1016/j.jmb.2018.06.048.
127. McInnes L, Healy J, Melville J. 2018 UMAP: Uniform Manifold Approximation and Projection for Dimension Reduction. arXiv <https://arxiv.org/abs/1802.03426>.
128. Dengler VL, Galbraith M, Espinosa JM. Transcriptional regulation by hypoxia inducible factors. Crit Rev Biochem Mol Biol **2014**;49(1):1-15 doi 10.3109/10409238.2013.838205.
129. Lin Q, Cong X, Yun Z. Differential hypoxic regulation of hypoxia-inducible factors 1alpha and 2alpha. Mol Cancer Res **2011**;9(6):757-65 doi 10.1158/1541-7786.MCR-11-0053.
130. Stokes JB, Adair SJ, Slack-Davis JK, Walters DM, Tilghman RW, Hershey ED*, et al.* Inhibition of focal adhesion kinase by PF-562,271 inhibits the growth and metastasis of pancreatic cancer concomitant with altering the tumor microenvironment. Mol Cancer Ther **2011**;10(11):2135-45 doi 10.1158/1535-7163.MCT-11-0261.
131. Deer EL, Gonzalez-Hernandez J, Coursen JD, Shea JE, Ngatia J, Scaife CL*, et al.* Phenotype and genotype of pancreatic cancer cell lines. Pancreas **2010**;39(4):425-35 doi 10.1097/MPA.0b013e3181c15963.
132. Ling G, Ji Q, Ye W, Ma D, Wang Y. Epithelial-mesenchymal transition regulated by p38/MAPK signaling pathways participates in vasculogenic mimicry formation in SHG44 cells transfected with TGF-beta cDNA loaded lentivirus in vitro and in vivo. Int J Oncol **2016**;49(6):2387-98 doi 10.3892/ijo.2016.3724.
133. Strippoli R, Benedicto I, Foronda M, Perez-Lozano ML, Sanchez-Perales S, Lopez-Cabrera M*, et al.* p38 maintains E-cadherin expression by modulating TAK1-NF-kappa B during epithelial-to-mesenchymal transition. J Cell Sci **2010**;123(Pt 24):4321-31 doi 10.1242/jcs.071647.
134. Gui T, Sun Y, Shimokado A, Muragaki Y. The Roles of Mitogen-Activated Protein Kinase Pathways in TGF-beta-Induced Epithelial-Mesenchymal Transition. J Signal Transduct **2012**;2012:289243 doi 10.1155/2012/289243.
135. Buonato JM, Lazzara MJ. ERK1/2 blockade prevents epithelial-mesenchymal transition in lung cancer cells and promotes their sensitivity to EGFR inhibition. Cancer Res **2014**;74(1):309-19 doi 10.1158/0008-5472.CAN-12-4721.
136. Srivastava S, Weitzmann MN, Cenci S, Ross FP, Adler S, Pacifici R. Estrogen decreases TNF gene expression by blocking JNK activity and the resulting production of c-Jun and JunD. J Clin Invest **1999**;104(4):503-13 doi 10.1172/JCI7094.
137. Lipner MB, Peng XL, Jin C, Xu Y, Gao Y, East MP*, et al.* Irreversible JNK1-JUN inhibition by JNK-IN-8 sensitizes pancreatic cancer to 5-FU/FOLFOX chemotherapy. JCI Insight **2020**;5(8) doi 10.1172/jci.insight.129905.

138. Kayahara M, Wang X, Tournier C. Selective regulation of c-jun gene expression by mitogen-activated protein kinases via the 12-o-tetradecanoylphorbol-13-acetate-responsive element and myocyte enhancer factor 2 binding sites. Mol Cell Biol **2005**;25(9):3784-92 doi 10.1128/MCB.25.9.3784-3792.2005.
139. Wlodarchak N, Xing Y. PP2A as a master regulator of the cell cycle. Crit Rev Biochem Mol Biol **2016**;51(3):162-84 doi 10.3109/10409238.2016.1143913.
140. Hu X, Wu X, Xu J, Zhou J, Han X, Guo J. Src kinase up-regulates the ERK cascade through inactivation of protein phosphatase 2A following cerebral ischemia. BMC Neurosci **2009**;10:74 doi 10.1186/1471-2202-10-74.
141. Eichhorn PJ, Creyghton MP, Wilhelmsen K, van Dam H, Bernards R. A RNA interference screen identifies the protein phosphatase 2A subunit PR55gamma as a stress-sensitive inhibitor of c-SRC. PLoS Genet **2007**;3(12):e218 doi 10.1371/journal.pgen.0030218.
142. Snider NT, Omary MB. Post-translational modifications of intermediate filament proteins: mechanisms and functions. Nat Rev Mol Cell Biol **2014**;15(3):163-77 doi 10.1038/nrm3753.
143. Tiwari A, Tashiro K, Dixit A, Soni A, Vogel K, Hall B*, et al.* Loss of HIF1A From Pancreatic Cancer Cells Increases Expression of PPP1R1B and Degradation of p53 to Promote Invasion and Metastasis. Gastroenterology **2020**;159(5):1882-97 e5 doi 10.1053/j.gastro.2020.07.046.
144. Furcht CM, Buonato JM, Skuli N, Mathew LK, Munoz Rojas AR, Simon MC*, et al.* Multivariate signaling regulation by SHP2 differentially controls proliferation and therapeutic response in glioma cells. J Cell Sci **2014**;127(Pt 16):3555-67 doi 10.1242/jcs.150862.
145. Mylonis I, Chachami G, Samiotaki M, Panayotou G, Paraskeva E, Kalousi A*, et al.* Identification of MAPK phosphorylation sites and their role in the localization and activity of hypoxia-inducible factor-1alpha. J Biol Chem **2006**;281(44):33095-106 doi 10.1074/jbc.M605058200.
146. Ast T, Mootha VK. Oxygen and mammalian cell culture: are we repeating the experiment of Dr. Ox? Nat Metab **2019**;1(9):858-60 doi 10.1038/s42255-019-0105-0.
147. Batie M, Druker J, D'Ignazio L, Rocha S. KDM2 Family Members are Regulated by HIF-1 in Hypoxia. Cells **2017**;6(1) doi 10.3390/cells6010008.
148. Lv N, Jin S, Liang Z, Wu X, Kang Y, Su L*, et al.* PP2Cdelta Controls the Differentiation and Function of Dendritic Cells Through Regulating the NSD2/mTORC2/ACLY Pathway. Front Immunol **2021**;12:751409 doi 10.3389/fimmu.2021.751409.
149. Jia D, Jolly MK, Tripathi SC, Den Hollander P, Huang B, Lu M*, et al.* Distinguishing mechanisms underlying EMT tristability. Cancer Converg **2017**;1(1):2 doi 10.1186/s41236-017-0005-8.
150. Celia-Terrassa T, Bastian C, Liu DD, Ell B, Aiello NM, Wei Y*, et al.* Hysteresis control of epithelial-mesenchymal transition dynamics conveys a distinct program with enhanced metastatic ability. Nat Commun **2018**;9(1):5005 doi 10.1038/s41467-018-07538-7.
151. Bagowski CP, Ferrell JE, Jr. Bistability in the JNK cascade. Curr Biol **2001**;11(15):1176-82 doi 10.1016/s0960-9822(01)00330-x.
152. Legewie S, Schoeberl B, Bluthgen N, Herzel H. Competing docking interactions can bring about bistability in the MAPK cascade. Biophys J **2007**;93(7):2279-88 doi 10.1529/biophysj.107.109132.
153. Fabian Z, Taylor CT, Nguyen LK. Understanding complexity in the HIF signaling pathway using systems biology and mathematical modeling. J Mol Med (Berl) **2016**;94(4):377-90 doi 10.1007/s00109-016-1383-6.
154. Berenguer J, Celia-Terrassa T. Cell memory of epithelial-mesenchymal plasticity in cancer. Curr Opin Cell Biol **2021**;69:103-10 doi 10.1016/j.ceb.2021.01.001.

155. Henry KE, Mack KN, Nagle VL, Cornejo M, Michel AO, Fox IL*, et al.* ERK Inhibition Improves Anti-PD-L1 Immune Checkpoint Blockade in Preclinical Pancreatic Ductal Adenocarcinoma. Mol Cancer Ther **2021**;20(10):2026-34 doi 10.1158/1535-7163.MCT-20-1112.
156. Alagesan B, Contino G, Guimaraes AR, Corcoran RB, Deshpande V, Wojtkiewicz GR*, et al.* Combined MEK and PI3K inhibition in a mouse model of pancreatic cancer. Clin Cancer Res **2015**;21(2):396-404 doi 10.1158/1078-0432.CCR-14-1591.
157. Ozkan-Dagliyan I, Diehl JN, George SD, Schaefer A, Papke B, Klotz-Noack K*, et al.* Low-Dose Vertical Inhibition of the RAF-MEK-ERK Cascade Causes Apoptotic Death of KRAS Mutant Cancers. Cell Rep **2020**;31(11):107764 doi 10.1016/j.celrep.2020.107764.
158. Bryant KL, Stalnecker CA, Zeitouni D, Klomp JE, Peng S, Tikunov AP*, et al.* Combination of ERK and autophagy inhibition as a treatment approach for pancreatic cancer. Nat Med **2019**;25(4):628-40 doi 10.1038/s41591-019-0368-8.
159. Fallah J, Rini BI. HIF Inhibitors: Status of Current Clinical Development. Curr Oncol Rep **2019**;21(1):6 doi 10.1007/s11912-019-0752-z.
160. Chen Y, Ren B, Yang J, Wang H, Yang G, Xu R*, et al.* The role of histone methylation in the development of digestive cancers: a potential direction for cancer management. Signal Transduct Target Ther **2020**;5(1):143 doi 10.1038/s41392-020-00252-1.
161. Dong B, Qiu Z, Wu Y. Tackle Epithelial-Mesenchymal Transition With Epigenetic Drugs in Cancer. Front Pharmacol **2020**;11:596239 doi 10.3389/fphar.2020.596239.
162. Dovzhanskiy DI, Arnold SM, Hackert T, Oehme I, Witt O, Felix K*, et al.* Experimental in vivo and in vitro treatment with a new histone deacetylase inhibitor belinostat inhibits the growth of pancreatic cancer. BMC Cancer **2012**;12:226 doi 10.1186/1471-2407-12-226.
163. Nguyen AH, Elliott IA, Wu N, Matsumura C, Vogelauer M, Attar N*, et al.* Histone deacetylase inhibitors provoke a tumor supportive phenotype in pancreatic cancer associated fibroblasts. Oncotarget **2017**;8(12):19074-88 doi 10.18632/oncotarget.13572.
164. Chao MW, Chang LH, Tu HJ, Chang CD, Lai MJ, Chen YY*, et al.* Combination treatment strategy for pancreatic cancer involving the novel HDAC inhibitor MPT0E028 with a MEK inhibitor beyond K-Ras status. Clin Epigenetics **2019**;11(1):85 doi 10.1186/s13148-019-0681-6.
165. Laschanzky RS, Humphrey LE, Ma J, Smith LM, Enke TJ, Shukla SK*, et al.* Selective Inhibition of Histone Deacetylases 1/2/6 in Combination with Gemcitabine: A Promising Combination for Pancreatic Cancer Therapy. Cancers (Basel) **2019**;11(9) doi 10.3390/cancers11091327.
166. Chen R, Chen Y, Zhao W, Fang C, Zhou W, Yang X*, et al.* The Role of Methyltransferase NSD2 as a Potential Oncogene in Human Solid Tumors. Onco Targets Ther **2020**;13:6837-46 doi 10.2147/OTT.S259873.
167. Shen Y, Morishita M, Lee D, Kim S, Lee T, Mevius D*, et al.* Identification of LEM-14 inhibitor of the oncoprotein NSD2. Biochem Biophys Res Commun **2019**;508(1):102-8 doi 10.1016/j.bbrc.2018.11.037.
168. Wang S, Yang H, Su M, Lian F, Cong Z, Wei R*, et al.* 5-Aminonaphthalene derivatives as selective nonnucleoside nuclear receptor binding SET domain-protein 2 (NSD2) inhibitors for the treatment of multiple myeloma. Eur J Med Chem **2021**;222:113592 doi 10.1016/j.ejmech.2021.113592.
169. Xu Y, Guo J, Liu J, Xie Y, Li X, Jiang H*, et al.* Hypoxia-induced CREB cooperates MMSET to modify chromatin and promote DKK1 expression in multiple myeloma. Oncogene **2021**;40(7):1231-41 doi 10.1038/s41388-020-01590-8.
170. Schodel J, Oikonomopoulos S, Ragoussis J, Pugh CW, Ratcliffe PJ, Mole DR. High-resolution genome-wide mapping of HIF-binding sites by ChIP-seq. Blood **2011**;117(23):e207-17 doi 10.1182/blood-2010-10-314427.

171. Wenger RH, Stiehl DP, Camenisch G. Integration of oxygen signaling at the consensus HRE. Sci STKE **2005**;2005(306):re12 doi 10.1126/stke.3062005re12.
172. Day EK, Campbell A, Pandolf A, Rogerson T, Zhong Q, Xiao A*, et al.* ERK-dependent suicide gene therapy for selective targeting of RTK/RAS-driven cancers. Mol Ther **2021**;29(4):1585-601 doi 10.1016/j.ymthe.2020.12.019.
173. Rogers S, Wells R, Rechsteiner M. Amino acid sequences common to rapidly degraded proteins: the PEST hypothesis. Science **1986**;234(4774):364-8 doi 10.1126/science.2876518.
174. Song C, Ye M, Liu Z, Cheng H, Jiang X, Han G*, et al.* Systematic analysis of protein phosphorylation networks from phosphoproteomic data. Mol Cell Proteomics **2012**;11(10):1070-83 doi 10.1074/mcp.M111.012625.
175. Vasseur S, Tomasini R, Tournaire R, Iovanna JL. Hypoxia induced tumor metabolic switch contributes to pancreatic cancer aggressiveness. Cancers (Basel) **2010**;2(4):2138-52 doi 10.3390/cancers2042138.
176. Jia D, Park JH, Kaur H, Jung KH, Yang S, Tripathi S*, et al.* Towards decoding the coupled decision-making of metabolism and epithelial-to-mesenchymal transition in cancer. Br J Cancer **2021**;124(12):1902-11 doi 10.1038/s41416-021-01385-y.
177. Guillaumond F, Leca J, Olivares O, Lavaut MN, Vidal N, Berthezene P*, et al.* Strengthened glycolysis under hypoxia supports tumor symbiosis and hexosamine biosynthesis in pancreatic adenocarcinoma. Proc Natl Acad Sci U S A **2013**;110(10):3919-24 doi 10.1073/pnas.1219555110.
178. Papa S, Choy PM, Bubici C. The ERK and JNK pathways in the regulation of metabolic reprogramming. Oncogene **2019**;38(13):2223-40 doi 10.1038/s41388-018-0582-8.
179. Teperino R, Schoonjans K, Auwerx J. Histone methyl transferases and demethylases; can they link metabolism and transcription? Cell Metab **2010**;12(4):321-7 doi 10.1016/j.cmet.2010.09.004.
180. Li W, Sun L, Lei J, Wu Z, Ma Q, Wang Z. Curcumin inhibits pancreatic cancer cell invasion and EMT by interfering with tumorstromal crosstalk under hypoxic conditions via the IL6/ERK/NFkappaB axis. Oncol Rep **2020**;44(1):382-92 doi 10.3892/or.2020.7600.
181. Zhang J, Cao J, Ma S, Dong R, Meng W, Ying M*, et al.* Tumor hypoxia enhances Non-Small Cell Lung Cancer metastasis by selectively promoting macrophage M2 polarization through the activation of ERK signaling. Oncotarget **2014**;5(20):9664-77 doi 10.18632/oncotarget.1856.
182. Xiong C, Zhu Y, Xue M, Jiang Y, Zhong Y, Jiang L*, et al.* Tumor-associated macrophages promote pancreatic ductal adenocarcinoma progression by inducing epithelial-to-mesenchymal transition. Aging (Albany NY) **2021**;13(3):3386-404 doi 10.18632/aging.202264.
183. Huber W, Carey VJ, Gentleman R, Anders S, Carlson M, Carvalho BS*, et al.* Orchestrating high-throughput genomic analysis with Bioconductor. Nat Methods **2015**;12(2):115-21 doi 10.1038/nmeth.3252.
184. Yu G, Wang LG, Han Y, He QY. clusterProfiler: an R package for comparing biological themes among gene clusters. OMICS **2012**;16(5):284-7 doi 10.1089/omi.2011.0118.
185. Brown BA, Myers PJ, Adair SJ, Pitarresi JR, Sah-Teli SK, Hart WS*, et al.* A histone methylation-MAPK signaling axis drives durable epithelial-mesenchymal transition in hypoxic pancreas cancer. bioRxiv **2022**.
186. Porter RL, Magnus NKC, Thapar V, Morris R, Szabolcs A, Neyaz A*, et al.* Epithelial to mesenchymal plasticity and differential response to therapies in pancreatic ductal adenocarcinoma. Proc Natl Acad Sci U S A **2019**;116(52):26835-45 doi 10.1073/pnas.1914915116.

187. Day EK, Sosale NG, Lazzara MJ. Cell signaling regulation by protein phosphorylation: a multivariate, heterogeneous, and context-dependent process. Curr Opin Biotechnol **2016**;40:185-92 doi 10.1016/j.copbio.2016.06.005.
188. Martin D, Degese MS, Vitale-Cross L, Iglesias-Bartolome R, Valera JLC, Wang Z*, et al.* Assembly and activation of the Hippo signalome by FAT1 tumor suppressor. Nat Commun **2018**;9(1):2372 doi 10.1038/s41467-018-04590-1.
189. Ansari D, Ohlsson H, Althini C, Bauden M, Zhou Q, Hu D*, et al.* The Hippo Signaling Pathway in Pancreatic Cancer. Anticancer Res **2019**;39(7):3317-21 doi 10.21873/anticanres.13474.
190. Ghiso E, Migliore C, Ciciriello V, Morando E, Petrelli A, Corso S*, et al.* YAP-Dependent AXL Overexpression Mediates Resistance to EGFR Inhibitors in NSCLC. Neoplasia **2017**;19(12):1012-21 doi 10.1016/j.neo.2017.10.003.
191. Vuoriluoto K, Haugen H, Kiviluoto S, Mpindi JP, Nevo J, Gjerdrum C*, et al.* Vimentin regulates EMT induction by Slug and oncogenic H-Ras and migration by governing Axl expression in breast cancer. Oncogene **2011**;30(12):1436-48 doi 10.1038/onc.2010.509.
192. Zhang G, Kong X, Wang M, Zhao H, Han S, Hu R*, et al.* AXL is a marker for epithelial-mesenchymal transition in esophageal squamous cell carcinoma. Oncol Lett **2018**;15(2):1900-6 doi 10.3892/ol.2017.7443.
193. Liu Q, Sheng Q, Ping J, Ramirez MA, Lau KS, Coffey RJ*, et al.* scRNABatchQC: multi-samples quality control for single cell RNA-seq data. Bioinformatics **2019**;35(24):5306-8 doi 10.1093/bioinformatics/btz601.
194. Barbie DA, Tamayo P, Boehm JS, Kim SY, Moody SE, Dunn IF*, et al.* Systematic RNA interference reveals that oncogenic KRAS-driven cancers require TBK1. Nature **2009**;462(7269):108-12 doi 10.1038/nature08460.
195. Andreatta M, Carmona SJ. UCell: Robust and scalable single-cell gene signature scoring. Comput Struct Biotechnol J **2021**;19:3796-8 doi 10.1016/j.csbj.2021.06.043.
196. Rajasekaran SA, Gopal J, Espineda C, Ryazantsev S, Schneeberger EE, Rajasekaran AK. HPAF-II, a cell culture model to study pancreatic epithelial cell structure and function. Pancreas **2004**;29(3):e77-83 doi 10.1097/00006676-200410000-00016.
197. Akrida I, Bravou V, Papadaki H. The deadly cross-talk between Hippo pathway and epithelial-mesenchymal transition (EMT) in cancer. Mol Biol Rep **2022** doi 10.1007/s11033-022-07590-z.
198. Pastushenko I, Mauri F, Song Y, de Cock F, Meeusen B, Swedlund B*, et al.* Fat1 deletion promotes hybrid EMT state, tumour stemness and metastasis. Nature **2021**;589(7842):448-55 doi 10.1038/s41586-020-03046-1.
199. Asiedu MK, Beauchamp-Perez FD, Ingle JN, Behrens MD, Radisky DC, Knutson KL. AXL induces epithelial-to-mesenchymal transition and regulates the function of breast cancer stem cells. Oncogene **2014**;33(10):1316-24 doi 10.1038/onc.2013.57.
200. Ludwig KF, Du W, Sorrelle NB, Wnuk-Lipinska K, Topalovski M, Toombs JE*, et al.* Small-Molecule Inhibition of Axl Targets Tumor Immune Suppression and Enhances Chemotherapy in Pancreatic Cancer. Cancer Res **2018**;78(1):246-55 doi 10.1158/0008-5472.CAN-17-1973.
201. Lu Y, Wan J, Yang Z, Lei X, Niu Q, Jiang L*, et al.* Regulated intramembrane proteolysis of the AXL receptor kinase generates an intracellular domain that localizes in the nucleus of cancer cells. FASEB J **2017**;31(4):1382-97 doi 10.1096/fj.201600702R.
202. Hu X, Zhai Y, Kong P, Cui H, Yan T, Yang J*, et al.* FAT1 prevents epithelial mesenchymal transition (EMT) via MAPK/ERK signaling pathway in esophageal squamous cell cancer. Cancer Lett **2017**;397:83-93 doi 10.1016/j.canlet.2017.03.033.

203. Rankin EB, Fuh KC, Castellini L, Viswanathan K, Finger EC, Diep AN*, et al.* Direct regulation of GAS6/AXL signaling by HIF promotes renal metastasis through SRC and MET. Proc Natl Acad Sci U S A **2014**;111(37):13373-8 doi 10.1073/pnas.1404848111.
204. Du W, Brekken RA. Does Axl have potential as a therapeutic target in pancreatic cancer? Expert Opin Ther Targets **2018**;22(11):955-66 doi 10.1080/14728222.2018.1527315.
205. Du W, Phinney NZ, Huang H, Wang Z, Westcott J, Toombs JE*, et al.* AXL Is a Key Factor for Cell Plasticity and Promotes Metastasis in Pancreatic Cancer. Mol Cancer Res **2021**;19(8):1412-21 doi 10.1158/1541-7786.MCR-20-0860.
206. Ammoun S, Provenzano L, Zhou L, Barczyk M, Evans K, Hilton DA*, et al.* Axl/Gas6/NFkappaB signalling in schwannoma pathological proliferation, adhesion and survival. Oncogene **2014**;33(3):336-46 doi 10.1038/onc.2012.587.
207. Auyez A, Sayan AE, Kriajevska M, Tulchinsky E. AXL Receptor in Cancer Metastasis and Drug Resistance: When Normal Functions Go Askew. Cancers (Basel) **2021**;13(19) doi 10.3390/cancers13194864.
208. Flem-Karlsen K, Nyakas M, Farstad IN, McFadden E, Wernhoff P, Jacobsen KD*, et al.* Soluble AXL as a marker of disease progression and survival in melanoma. PLoS One **2020**;15(1):e0227187 doi 10.1371/journal.pone.0227187.
209. Song W, Wang H, Lu M, Ni X, Bahri N, Zhu S*, et al.* AXL Inactivation Inhibits Mesothelioma Growth and Migration via Regulation of p53 Expression. Cancers (Basel) **2020**;12(10) doi 10.3390/cancers12102757.
210. Martinez-Bosch N, Cristobal H, Iglesias M, Gironella M, Barranco L, Visa L*, et al.* Soluble AXL is a novel blood marker for early detection of pancreatic ductal adenocarcinoma and differential diagnosis from chronic pancreatitis. EBioMedicine **2022**;75:103797 doi 10.1016/j.ebiom.2021.103797.
211. Brown MS, Abdollahi B, Wilkins OM, Lu H, Chakraborty P, Ognjenovic NB*, et al.* Phenotypic heterogeneity driven by plasticity of the intermediate EMT state governs disease progression and metastasis in breast cancer. Sci Adv **2022**;8(31):eabj8002 doi 10.1126/sciadv.abj8002.
212. Kang E, Seo J, Yoon H, Cho S. The Post-Translational Regulation of Epithelial-Mesenchymal Transition-Inducing Transcription Factors in Cancer Metastasis. Int J Mol Sci **2021**;22(7) doi 10.3390/ijms22073591.
213. Dong B, Wu Y. Epigenetic Regulation and Post-Translational Modifications of SNAI1 in Cancer Metastasis. Int J Mol Sci **2021**;22(20) doi 10.3390/ijms222011062.
214. Boopathy GTK, Hong W. Role of Hippo Pathway-YAP/TAZ Signaling in Angiogenesis. Front Cell Dev Biol **2019**;7:49 doi 10.3389/fcell.2019.00049.
215. Plouffe SW, Hong AW, Guan KL. Disease implications of the Hippo/YAP pathway. Trends Mol Med **2015**;21(4):212-22 doi 10.1016/j.molmed.2015.01.003.
216. Punt CJ, Koopman M, Vermeulen L. From tumour heterogeneity to advances in precision treatment of colorectal cancer. Nat Rev Clin Oncol **2017**;14(4):235-46 doi 10.1038/nrclinonc.2016.171.
217. Rashid NU, Peng XL, Jin C, Moffitt RA, Volmar KE, Belt BA*, et al.* Purity Independent Subtyping of Tumors (PurIST), A Clinically Robust, Single-sample Classifier for Tumor Subtyping in Pancreatic Cancer. Clin Cancer Res **2020**;26(1):82-92 doi 10.1158/1078-0432.CCR-19-1467.
218. Palamaris K, Felekouras E, Sakellariou S. Epithelial to Mesenchymal Transition: Key Regulator of Pancreatic Ductal Adenocarcinoma Progression and Chemoresistance. Cancers (Basel) **2021**;13(21) doi 10.3390/cancers13215532.
219. Sun XX, Yu Q. Intra-tumor heterogeneity of cancer cells and its implications for cancer treatment. Acta Pharmacol Sin **2015**;36(10):1219-27 doi 10.1038/aps.2015.92.

220. Du B, Shim JS. Targeting Epithelial-Mesenchymal Transition (EMT) to Overcome Drug Resistance in Cancer. Molecules **2016**;21(7) doi 10.3390/molecules21070965.
221. Maechler M. RP, Struyf A,. Hubert M., Hornik K. 2022 cluster: Cluster Analysis Basics and Extensions. <https://CRAN.R-project.org/package=cluster>.
222. Bunis DG, Andrews J, Fragiadakis GK, Burt TD, Sirota M. dittoSeq: Universal User-Friendly Single-Cell and Bulk RNA Sequencing Visualization Toolkit. Bioinformatics **2020** doi 10.1093/bioinformatics/btaa1011.
223. Wickham H, François R., Henry L., Müller K. 2022 dplyr: A Grammar of Data Manipulation. <https://dplyr.tidyverse.org, https://github.com/tidyverse/dplyr>.
224. Borcherding N, Vishwakarma A, Voigt AP, Bellizzi A, Kaplan J, Nepple K*, et al.* Mapping the immune environment in clear cell renal carcinoma by single-cell genomics. Commun Biol **2021**;4(1):122 doi 10.1038/s42003-020-01625-6.
225. Ritchie ME, Phipson B, Wu D, Hu Y, Law CW, Shi W*, et al.* limma powers differential expression analyses for RNA-sequencing and microarray studies. Nucleic Acids Res **2015**;43(7):e47 doi 10.1093/nar/gkv007.
226. Carlson M. org.Hs.eg.db: Genome wide annotation for Human. **2019**.
227. Pedersen T. 2022 patchwork: The Composer of Plots. <https://patchwork.data-imaginist.com>.
228. Henry L. WH. 2022 rlang: Functions for Base Types and Core R and 'Tidyverse' Features. <https://rlang.r-lib.org, https://github.com/r-lib/rlang>.
229. Stuart T, Butler A, Hoffman P, Hafemeister C, Papalexi E, Mauck WM, 3rd*, et al.* Comprehensive Integration of Single-Cell Data. Cell **2019**;177(7):1888-902 e21 doi 10.1016/j.cell.2019.05.031.
230. Satija R, Farrell JA, Gennert D, Schier AF, Regev A. Spatial reconstruction of single-cell gene expression data. Nat Biotechnol **2015**;33(5):495-502 doi 10.1038/nbt.3192.
231. Hao Y, Hao S, Andersen-Nissen E, Mauck WM, 3rd, Zheng S, Butler A*, et al.* Integrated analysis of multimodal single-cell data. Cell **2021**;184(13):3573-87 e29 doi 10.1016/j.cell.2021.04.048.
232. Butler A, Hoffman P, Smibert P, Papalexi E, Satija R. Integrating single-cell transcriptomic data across different conditions, technologies, and species. Nat Biotechnol **2018**;36(5):411-20 doi 10.1038/nbt.4096.
233. H. W. 2022 stringr: Simple, Consistent Wrappers for Common String Operations. <http://stringr.tidyverse.org, https://github.com/tidyverse/stringr>.
234. Meidhof S, Brabletz S, Lehmann W, Preca BT, Mock K, Ruh M*, et al.* ZEB1-associated drug resistance in cancer cells is reversed by the class I HDAC inhibitor mocetinostat. EMBO Mol Med **2015**;7(6):831-47 doi 10.15252/emmm.201404396.
235. El Amrani M, Corfiotti F, Corvaisier M, Vasseur R, Fulbert M, Skrzypczyk C*, et al.* Gemcitabine-induced epithelial-mesenchymal transition-like changes sustain chemoresistance of pancreatic cancer cells of mesenchymal-like phenotype. Mol Carcinog **2019**;58(11):1985-97 doi 10.1002/mc.23090.
236. Gu Y, Zhang B, Gu G, Yang X, Qian Z. Metformin Increases the Chemosensitivity of Pancreatic Cancer Cells to Gemcitabine by Reversing EMT Through Regulation DNA Methylation of miR-663. Onco Targets Ther **2020**;13:10417-29 doi 10.2147/OTT.S261570.
237. Namba T, Kodama R, Moritomo S, Hoshino T, Mizushima T. Zidovudine, an anti-viral drug, resensitizes gemcitabine-resistant pancreatic cancer cells to gemcitabine by inhibition of the Akt-GSK3beta-Snail pathway. Cell Death Dis **2015**;6:e1795 doi 10.1038/cddis.2015.172.
238. Han J, Liu Y, Yang S, Wu X, Li H, Wang Q. MEK inhibitors for the treatment of non-small cell lung cancer. J Hematol Oncol **2021**;14(1):1 doi 10.1186/s13045-020-01025-7.

239. Wagner EF, Nebreda AR. Signal integration by JNK and p38 MAPK pathways in cancer development. Nat Rev Cancer **2009**;9(8):537-49 doi 10.1038/nrc2694.
240. Stanta G, Bonin S. Overview on Clinical Relevance of Intra-Tumor Heterogeneity. Front Med (Lausanne) **2018**;5:85 doi 10.3389/fmed.2018.00085.
241. Lou X, Qin Y, Xu X, Yu X, Ji S. Spatiotemporal heterogeneity and clinical challenge of pancreatic neuroendocrine tumors. Biochim Biophys Acta Rev Cancer **2022**;1877(5):188782 doi 10.1016/j.bbcan.2022.188782.
242. Foo J, Michor F. Evolution of resistance to targeted anti-cancer therapies during continuous and pulsed administration strategies. PLoS Comput Biol **2009**;5(11):e1000557 doi 10.1371/journal.pcbi.1000557.
243. Foo J, Michor F. Evolution of resistance to anti-cancer therapy during general dosing schedules. J Theor Biol **2010**;263(2):179-88 doi 10.1016/j.jtbi.2009.11.022.
244. Schattler HL, U. Optimal Control for Mathematical Models of Cancer Therapies: An Application of Geometric Methods. New York, NY: Springer Science+Business Media LLC; 2015.
245. Gluzman M, Scott JG, Vladimirsky A. Optimizing adaptive cancer therapy: dynamic programming and evolutionary game theory. Proc Biol Sci **2020**;287(1925):20192454 doi 10.1098/rspb.2019.2454.